JAN 19 1986

C 13.46: 1217

180

NBS TECHNICAL NOTE 1217

U.S. DEPARTMENT OF COMMERCE/National Bureau of Standards

NBS Reactor:

Summary of Activities July 1984 Through June 1985

ORIGINAL

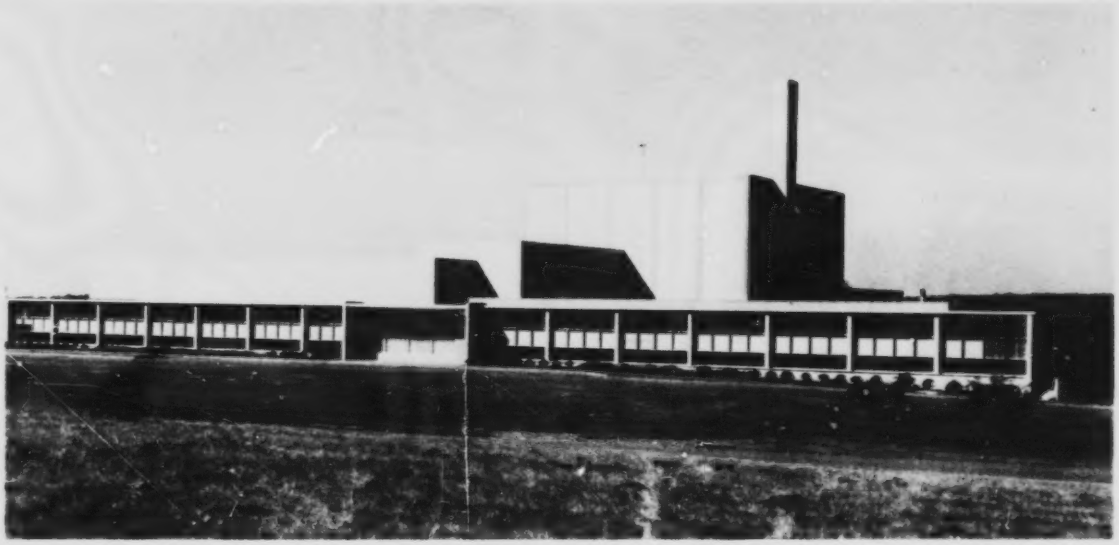

BEST COPY AVAILABLE

The National Bureau of Standards[1] was established by an act of Congress on March 3, 1901. The Bureau's overall goal is to strengthen and advance the nation's science and technology and facilitate their effective application for public benefit. To this end, the Bureau conducts research and provides: (1) a basis for the nation's physical measurement system, (2) scientific and technological services for industry and government, (3) a technical basis for equity in trade, and (4) technical services to promote public safety. The Bureau's technical work is performed by the National Measurement Laboratory, the National Engineering Laboratory, the Institute for Computer Sciences and Technology, and the Institute for Materials Science and Engineering.

The National Measurement Laboratory

Provides the national system of physical and chemical measurement; coordinates the system with measurement systems of other nations and furnishes essential services leading to accurate and uniform physical and chemical measurement throughout the Nation's scientific community, industry, and commerce; provides advisory and research services to other Government agencies; conducts physical and chemical research; develops, produces, and distributes Standard Reference Materials; and provides calibration services. The Laboratory consists of the following centers:

- Basic Standards[2]
- Radiation Research
- Chemical Physics
- Analytical Chemistry

The National Engineering Laboratory

Provides technology and technical services to the public and private sectors to address national needs and to solve national problems; conducts research in engineering and applied science in support of these efforts; builds and maintains competence in the necessary disciplines required to carry out this research and technical service; develops engineering data and measurement capabilities; provides engineering measurement traceability services; develops test methods and proposes engineering standards and code changes; develops and proposes new engineering practices; and develops and improves mechanisms to transfer results of its research to the ultimate user. The Laboratory consists of the following centers:

- Applied Mathematics
- Electronics and Electrical Engineering[2]
- Manufacturing Engineering
- Building Technology
- Fire Research
- Chemical Engineering[2]

The Institute for Computer Sciences and Technology

Conducts research and provides scientific and technical services to aid Federal agencies in the selection, acquisition, application, and use of computer technology to improve effectiveness and economy in Government operations in accordance with Public Law 89-306 (40 U.S.C. 759), relevant Executive Orders, and other directives; carries out this mission by managing the Federal Information Processing Standards Program, developing Federal ADP standards guidelines, and managing Federal participation in ADP voluntary standardization activities; provides scientific and technological advisory services and assistance to Federal agencies; and provides the technical foundation for computer-related policies of the Federal Government. The Institute consists of the following centers:

- Programming Science and Technology
- Computer Systems Engineering

The Institute for Materials Science and Engineering

Conducts research and provides measurements, data, standards, reference materials, quantitative understanding and other technical information fundamental to the processing, structure, properties and performance of materials; addresses the scientific basis for new advanced materials technologies; plans research around cross-country scientific themes such as nondestructive evaluation and phase diagram development; oversees Bureau-wide technical programs in nuclear reactor radiation research and nondestructive evaluation; and broadly disseminates generic technical information resulting from its programs. The Institute consists of the following Divisions:

- Ceramics
- Fracture and Deformation [3]
- Polymers
- Metallurgy
- Reactor Radiation

[1] Headquarters and Laboratories at Gaithersburg, MD, unless otherwise noted; mailing address Gaithersburg, MD 20899.
[2] Some divisions within the center are located at Boulder, CO 80303.
[3] Located at Boulder, CO, with some elements at Gaithersburg, MD.

BEST COPY AVAILABLE

NBS Reactor: Summary of Activities July 1984 Through June 1985

Frederick J. Shorten, Editor

Reactor Radiation Division
Institute for Materials Science and Engineering
National Bureau of Standards
Gaithersburg, MD 20899

December 1985

U.S. DEPARTMENT OF COMMERCE, Malcolm Baldrige, Secretary
NATIONAL BUREAU OF STANDARDS, Ernest Ambler, Director

BEST COPY AVAILABLE

National Bureau of Standards Technical Note 1217
Natl. Bur. Stand. (U.S.), Tech. Note 1217, 175 pages (Dec. 1985)
CODEN: NBTNAE

U.S. GOVERNMENT PRINTING OFFICE
WASHINGTON: 1985

BEST COPY AVAILABLE

II

FOREWORD

The National Bureau of Standards Reactor was built not only to serve the needs of the NBS but also those of other government agencies as a National Center for the application of neutron methods to problems of national interest. The Reactor Radiation Division was established to operate the reactor and to foster its scientific and technological use. Toward this end, the Division has a small nucleus of scientists experienced in the use of reactors for a wide range of scientific and technical problems. In addition to pursuing their own research and developing sophisticated experimental facilities, they actively seek out and encourage collaboration with other scientists engaged in challenging programs whose work can benefit from use of the reactor, but who as yet do not have the reactor experience necessary to take full advantage of the facilities available. The Division also provides irradiation services to a wide variety of users as well as engineering and other technical services.

The reactor power was increased from 10 to 20 MW during the past year and provided 25 experimental facilities ranging from intense neutron beams to extensive irradiation facilities, making it one of the most versatile high performance research reactors in the country. Thus, it is able to serve a large number of scientists and engineers in a broad range of activities both within and outside the NBS.

This report attempts to summarize all the work done which is dependent on the reactor including a large number of programs outside the Division. The first section summarizes the programs carried out by scientists in the Reactor Radiation Division and their collaborators. The second section summarizes NBS work originating outside NBS for which the Division provides irradiation services. The remaining sections are self-explanatory.

Appreciation is extended F. J. Shorten of the Reactor Radiation Division for his extensive contributions to the editing, organization, and preparation of this report, and T. L. Lindstrom, K. E. Ferrel, M. H. Clark, and S. Tassey for efforts in typing manuscripts.

R. S. Carter

R. S. Carter
Chief, Reactor Radiation Division
National Bureau of Standards

BEST COPY AVAILABLE

ABSTRACT

This report summarizes all those programs which depend on the NBS reactor. It covers the period from July 1984 through June 1985. The programs range from the use of neutron beams to study the structure and dynamics of materials through nuclear physics and neutron standards to sample irradiations for activation analysis, isotope production, radiation effects studies, neutron radiography, and nondestructive evaluation.

Key words: Activation analysis; crystal structure; diffraction; isotopes; molecular dynamics; neutron; neutron radiography; nondestructive evaluation; nuclear reactor; radiation.

DISCLAIMER

Certain trade names and company products are identified in order to adequately specify the experiment procedure. In no case does such identification imply recommendation or endorsement by the National Bureau of Standards, nor does it imply that the products are necessarily the best available for the purpose.

BEST COPY AVAILABLE

TABLE OF CONTENTS

FOREWORD iii

ABSTRACT. iv

A. REACTOR RADIATION DIVISION AND COLLABORATIVE PROGRAMS 1

Control of Pore Size In Zeolite RhO. 1

Structural Characterization of the Lithium Insertion Compound, $LiFe(II)ClMoO_4$. 1

The Structure of $2BaBr_2 \cdot BaCl_2$. 2

Structural Changes in Nasicon Solid Solutions, $Na_{1+x}Zr_2Si_xP_{3-x}O_{12}$, at Elevated Temperatures 4

Structure of Barium Titanium Niobium Oxides. 10

Neutron Powder Diffraction Study of the Structure of the Compound $Li_{0.31}La_{0.56}MoO_4$. 11

Geometrical Ambiguities in the Indexing of Powder Patterns 11

Texture of Extruded Uranium Alloys by Neutron Diffraction. 12

The Nondestructive Determination of Near-Surface Residual Stresses in Depleted Uranium Alloys 15

Crystal Data 21

Local Modes in Dilute Metal-Hydrogen Alloys. 22

Neutron Scattering Studies of Hydrogen in Yttrium. 25

Stochastic States Theory of Neutron Scattering from Self-Trapped Defects in Solids. 29

Theory of Processes Contributing to Quasielastic Neutron Scattering from Hydrogen in Metals. 33

Translation-Rotation Coupling - Alkali Cyanide/Alkali Halides. 35

Interaction of Vibrating H Atoms on the Surface of Platinum Particles by Isotope Dilution Neutron Spectroscopy 36

Incoherent Inelastic Neutron Scattering Study of the Interaction of Adsorbed Hydrogen with Oxygen on Platinum Black. 39

Neutron Scattering Studies of Zeolite RhO. 42

Study of Dynamical and Static Scaling of the λ Transition in ^4He 44

Simulation of a Slightly More Complex Chemical Reaction. 45

Neutron Scattering Studies of Diluted Magnetic Semiconductor Systems $Cd_{1-x}Mn_xTe$ and $Zn_{1-x}Mn_xSe$ 46

Long-Range Incommensurate Spin State in Dilute YGd Alloys. 49

BEST COPY AVAILABLE

TABLE OF CONTENTS

Field Dependence of the Two-Spin Correlation Function in a Reentrant Spin Glass 52
Neutron Scattering Study of the Spin Dynamics of Amorphous $Fe_{70}Ni_{20}Zr_{10}$ . . .55
Magnetic Order in the Superconductor $Tm_2Fe_3Si_5$ 58
Magnetic and Superconducting Properties of Holmium-Rich $(Er_{1-x}Ho_x)Rh_4B_4$ . .60
Advanced Neutron Methods 61
Cold Neutron Research Facility 63
NBSR Cold Neutron Source 64
The NBS Neutron Time-Of-Flight Spectrometer. 66
The Phase Shift and Multiple Scattering in Small Angle Neutron Scattering: Application to Beam Broadening from Ceramics. 68
Study of Plasma Spray Coatings by Small Angle Neutron Scattering 72
Critical Fluctuation and Phase Behavior of a Binary Polymer System 73
Small Network Structure Studied with Small Angle Neutron Scattering. 78
SANS Study of a Concentrated Protein Solution. 79
Joint Neutron and X-ray Structural Refinement of Porcine Insulin 81
Neutron Activation Autoradiography Study of Paintings. 83
B. NON-RRD PROGRAMS. 86
Nuclear Methods Group: Overview 86
High Resolution Neutron Depth Profiling (NDP) and Secondary Ion Mass Spectrometer (SIMS) of Boron Through Oxide-Silicon Interfaces. 88
High-Sensitivity Determination of Idoine Isotopic Ratios by Thermal and Fast Neutron Activation. 93
Neutron-Capture Prompt-γ Activation Analysis and Related Studies 95
IAEA Coordinated Research Program on Human Daily Dietary Intakes of Nutritionally Important Trace Elements. 99
Determination of Gold and Platinum in Human Urine, SRM 2670. 100
Multielement Analysis of Biological Macromolecules 103
Development of Biomonitoring Specimen Bank in the United States. 107
Facilities and Equipment for Activation Analysis. 111
Atmospheric and Environmental Studies by Instrumental Neutron Activation Analysis. 112
Characterization of the NBSR at 20MW 120
Summary of Reactor Related Activities Carried Out by the Neutron Field Standards Group 130
Neutron Driven Gamma Ray Field 138

BEST COPY AVAILABLE

TABLE OF CONTENTS

Experimental Microdosimetry. 140
C. REACTOR OPERATIONS AND SERVICES 147
D. SERVICE PROGRAMS 150
The Food and Drug Administration's Neutron Activation Facility 150
Preparation of F-18 Labeled Radiotracers Using NBS Reactor-Produced F-18 . .151
Production of F-18 on Low Flux Reactors. 151
E. PERSONNEL ROSTER. 153
F. PUBLICATIONS. 160

BEST COPY AVAILABLE

A. Reactor Radiation Division and Collaborative Programs

CONTROL OF PORE SIZE IN ZEOLITE RHO

G. D. Stucky
(E. I. duPont de Nemours and Co., Wilmington, DE)
and
E. Prince

Selectivity in organic reactions is generallly determined by a few kilocalories/mole, which in zeolite catalysis translates into differences of a few tenths of an angstrom in zeolite pore dimensions. Framework flexibility can be used to control reaction selectivity by using the response of the three dimensional surface to temperature, sorbate and cation coordination. For zeolite, Rho, a simple distortion involving the "breathing" of a double 8-ring can be modeled as a function of the cubic unit cell dimension. The degree to which the ring opening will distort is given by a parameter D, which measures the degree of ellipticity of the double 8-ring opening. Neutron diffraction studies of LiRho have shown a mechanism for inducing this distortion by design. This has been confirmed by the temperature dependent contraction of the unit cell of CaRho which results in the smallest unit cell reported for a Rho zeolite. Dehydration of BeRho lowers the crystal system symmetry from cubic to monoclinic, indicative of the stronger metal atom framework interaction expected for the smaller divalent cation.

STRUCTURAL CHARACTERIZATION OF THE LITHIUM INSERTION COMPOUND, $LiFe(II)ClMoO_4$

C. C. Torardi
(E. I. duPont de Nemours and Co., Wilmington, DE)
and
E. Prince

The structure and magnetism of the new layered tetragonal antiferromagnet $Fe(III)ClMoO_4$ has been recently described (1,2). Reaction of this compound with LiI in acetonitrile under inert atmosphere yields the lithium-inserted monoclinic material $LiFe(II)ClMoO_4$. This topochemical redox reaction is completely reversible. Neutron powder diffraction data were collected on the lithium phase, and the structure has been determined using the NBS Rietveld profile refinement computer programs.

BEST COPY AVAILABLE

The title compound is monoclinic,m space group $P2_1/m$, with a = 6.9944(6), b = 6.8714(6), c = 5.0144(5) A, and β = 91.272(5)°. Although two crystallographic sites exist between the $FeClMoO_4$ layers for lithium occupation, only one site is occupied. This results in a fully ordered structural arrangement. Lithium is octahedrally coordinated to four oxygen and two chlorine atoms. FeO_4Cl_2 octahedra in LiFe $ClMoO_4$ are so much less distorted than in the parent compound which contains FeO_4Cl square pyramids with an additional Cl atom 3.02A from iron.

---

1. C. C. Torardi, J. C. Calabrese, K. Lázár, and W. M. Reiff J. Solid State Chem. 51, 376 (1984).

2. NBS Technical Note 1207, ed. F. J. Shorten (1984)

THE STRUCTURE OF $2BaBr_2 \cdot BaCl_2$

H. A. Eick

(Michigan State University, East Lansing, MI)

and

E. Prince

Both $BaCl_2$ and $BaBr_2$ exhibit orthorhombic $PbCl_2$-type symmetry.[1] An x-ray diffraction study of the $BaBr_2$-$BaCl_2$ system indicated a non linear variation of the a and c parameters (space group Pnma) with composition, but a linear variation of b parameter and the volume.[1] Data collected in an x-ray powder diffraction study of the phase, BaBrCl, when fit by Rietveld line profile procedures, indicated the phase to be anion-ordered with the chloride ions occupying only the tetrahedral holes and the bromide ions occupying only the square pyramidal holes. In an effort to determine if at other compositions, i.e., a Cl/Br ratio of about 0.5, anion ordering would force the symmetry of the system to change or cause a doubling of the unit cell parameters, a neutron diffraction study of an intermediate composition, $2BaBr_2 \cdot BaCl_2$, was undertaken.

The sample submitted for analysis was prepared by fusing in Al_2O_3 crucibles confined in high vacuum an intimately ground mixture of $BaCl_2$ and $BaBr_2$ mixed in the molar stoichiometric ratio of 2:1. The $BaCl_2$, purchased from CERAC, Inc., Milwaukee, Wisconsin, was placed in an Al_2O_3 crucible and fused in high vacuum prior to use. The $BaBr_2$ was prepared from BaO (Fisher Scientific) by a conventional NH_4Cl/HCl chlorination procedure, and was then fused as was the $BaCl_2$. X-ray powder diffraction analysis of both reactants and the products indicated the presence of only reflections assignable to the Pnma-$PbCl_2$ type structure.

BEST COPY AVAILABLE

Neutron diffraction data collected over the range $17° < 2\theta < 122°$ on the NBS neutron diffractometer at ambient temperature (λ = 1.5500A), were refined by Rietveld line profile least-square analysis procedures at Michigan State University with the programs REFINE provided by E. Prince.

The structure refined to an R value of 7.73 (statistically expected value: 4.97) with 36 variables. Cell, positional, and anisotropic thermal parameters are presented in table 1. The half width parameters u,v, and w are 4178(151), 230(47), and 716(11), respectively.

During the refinement process with both anion thermal parameters isotropic, the bromine anion occupancy of both anion positions was allowed to vary, the overall occupancy only being constrained to the mixed composition. Under these conditins, the occupancy of anion position 1 refined to 1.009(16). It was thus assumed that the

Table 1. Positional, Anisotropic Thermal, and Cell Parameters for $2BaBr_2 \cdot BaCl_2$. The digit(s) in parenthesis indicate the estimated standard deviation of the last digit(s).

	X	Y	Z
Ba	0.2603(4)	0.25	0.1203(3)
Br1	0.0293(3)	0.25	0.8292(3)
(Br,Cl)2	0.1446(2)	0.25	0.4329(2)

	B(1,1)	B(2,2)	B(3,3)	B(1,2)	B(1,3)	B(2,3)
Ba	0.67(15)	1.40(16)	2.23(15)	0	0.29(12)	0
Br1	1.62(14)	1.62(13)	1.55(13)	0	0.00(10)	0
(Br,Cl)2	1.38(10)	1.56(10)	1.19(9)	0	0.29(9)	0

Lattice Parameters

a = 8.2031(3)
b = 4.8606(2)
c = 9.6359(4)

BEST COPY AVAILABLE

square pyramidal hole was occupied exclusively by bromine atoms, and occupancy was removed as a variable. Thus, even at this intermediate composition, anions do not randomly substitute in the structure. However, no evidence for a doubling of one of the lattice parameters to accommodate an ordering of the chloride and bromide anions within the tetrahedral holes was found. An examination of the plot output indicated a generally good fit of the data throughout the entire spectrum, but a couple of spurious reflections were present in the region $109<2\theta<114°$. A Hamilton's test of the R values obtained with and without all thermal parameters aniostropic indicated the anisotropic parameters to be significant.

The lattice parameters agree well with the values expected from Hodorowitz, et al., and the positional parameters are in excellent agreement with those derived for BaBrCl,[1] and in fair agreement with those reported for $BaBr_2$.[2]

1. S. A. Hodorowitz, E. K. Hodorowitz, H. A. Eick, J. Solid State Chemistry 48, 351-6(1982).

2. E. B. Brackett, T. E. Brackett, R. L. Sass, J. Phys. Chem. 67, 2132-5(1963).

STRUCTURAL CHANGES IN NASICON SOLID SOLUTIONS, $Na_{1+x}Zr_2Si_xP_{3-x}O_{12}$, AT ELEVATED TEMPERATURES

J. J. Didisheim and B. J. Wuensch
(Massachusetts Institute of Technology, Cambridge, MA)

and

E. Prince

The ionic electrical conductivity of solid solutions between sodium zirconium phosphate and sodium zirconium silicate, $Na_{1+x}Zr_2Si_xP_{3-x}O_{12}$, rises four orders of magnitude from the modest conductivity of the endmember compositions to a maximum near $x = 2$. This change in conductivity seems closely correlated to change in crystal structure. The a axis of these hexagonal or monoclinic pseudo-hexagonal phases (for $1.6 < x < 2.2$) increases monotonically with x. The length of the c axis (and the cell volume, as a result), however, rises to a maximum value and then decreases upon further substitution of the larger Si ion for P. The composition with maximum cell volume falls close to that of maximum conductivity. To understand the structure changes which give rise to these anomalies and, presumably, the enhanced conductivity, Rietveld analyses of the crystal structure of solid solutions as a function of composition had been earlier performed at room temperature[1-3] with neutron powder diffraction data obtained from phases with $x = 1.0$, 2.5 and 3.0

BEST COPY AVAILABLE

(hexagonal, space group $R\bar{3}c$) and x = 1.6 and 2.0 (monoclinic space group C2/c). The results revealed that the principal change in the framework with composition is a rotation of the orientation of the tetrahedral (P, Si) groups up to x = 2, followed by a progressive return to the original orientation for larger values of x. The rotation acts to stretch the height of an octahedral cavity fully occupied by Na(1), and this change in length accounts almost entirely for the variation in c. The rotation also acts to open the saddle-point arrangement of oxygen ions that separates neighboring Na ions. The radius of this "window" was found to attain a maximum value, close to the ionic radius of Na^+, near the composition of maximum conductivity. One would expect this to lower the barrier to a diffusive jump between alkali ion sites. Evidence that this is indeed the case is provided by the fact that the temperature factors for the Na ions increase sharply to a maximum near x = 2, suggesting a softening of the potential well in which they reside. The Na ions that occupy one of two types of interstices available in the framework assume temperature factors that are too large to be physically reasonable. Moreover, the observed Na-O bond distance is much too large, and the maximum in scattering density in this site, as revealed by Fourier and difference syntheses, does not fall at the center of the site. This suggests that a static atomic displacement occurs as a result of the "stretching" of the cavity described above, and that the thermal motion is only apparent.

The studies of the phases are currently being extended to elevated temperatures. The objectives are to (a) examine possible order-disorder transformations among the alkali-ion sites, one of which was found to be fully occupied in all compositions at room temperature, (b) distinguish positional disorder from time-averaged thermal vibration of the sodium ions through the temperature dependence of the temperature factor coefficients, and (c) establish the extent to which anisotropic thermal expansion shifts the composition at which optimum size occurs for the "window" between neighboring Na sites, thereby providing further insight into the role of charge carrier concentration, as opposed to mobility, in determination of the enhanced conductivity.

Measurements have begun with examination of the high conductivity compositions near x = 2. Neutron powder diffraction data have been obtained at 275° and 320°C for a sample with x = 2.0 and at 320°C for x = 1.6. Refinement of the structure with these three data sets is still in progress, but is sufficiently close to convergence that values for the atomic coordinates are likely close to their final values. These parameters are presented in table 1. Comparison of the results with the room-temperature structures at these compositions is not straightforward, as phases with $1.6 < x < 2.2$ are monoclinic under ambient conditions but transform to the

BEST COPY AVAILABLE

rhombohedral structure at the temperatures at which the present measurements were performed. The monoclinic structures are strongly pseudo-hexagonal, however. The atomic positions found for the monoclinic room-temperature were thus converted to coordinates expressed relative to hexagonal axes for purposes of comparison in table 1.

The atomic positions in the high-temperature rhombohedral phases may be seen to remain remarkably close to those in the corresponding monoclinic phase. The shift in the framework cations is very slight, amounting to 0.001 c (0.02Å) or less for Zr and on the order of 0.001 a (0.009 Å) for Si. The coordinates for the oxygen ions also remain fairly invariant, but a shift of 0.12Å in the z coordinate of O(2) indicates some rotation of the orientation of the tetrahedral groups. The other significant shift in position is the location of Na(2), which moves 0.15Å along a. As the alkali ions are located in shallow potential wells, it is expected that relatively small rearrangements of the framework ions might result in significant displacement of the mobile alkali ions. The lattice constants indicate an anisotropic expansion

BEST COPY AVAILABLE

Table 1. . Comparison of Atomic Coordinates in NASICON Solid Solutions $Na_{1+x}Zr_2Si_xP_{3-x}O_{12}$ at Room Temperature and at Elevated Temperature (Estimated Standard Deviations in Parentheses).

		x = 1.6		x = 2.0		
		23°C†	320°C	23°C†	275°C	320°C
Na(1)	occupancy	1.0	1.01(7)	1.0	1*	1.01(7)
Na(2)	occupancy	**	0.53(2) [0.533 ideal]	**	2*	0.667(2) [0.677 ideal]
	x	0.6429	0.626(3)	0.6231	0.636(2)	0.633(5)
Zr	z	0.1476	0.1483(3)	0.1464(5)	0.1464(5)	0.1474(4)
(Si,P)	x	0.2898	0.2897(8)	0.2840	0.283(10	0.288(1)
O(1)	x	0.1780	0.1735(6)	0.1805	0.1772(9)	0.177(1)
	y	-0.0432	-0.0349(7)	-0.0459	-0.035(1)	-0.0368(9)
	z	0.1890	0.1944(2)	0.1869	0.1950(3)	0.1940(3)
O(2)	x	0.1942	0.1949(6)	0.1974	0.192(1)	0.1928(8)
	y	0.1780	0.1708(6)	0.1754	0.1713(8)	0.1714(8)
	z	0.0926	0.0915(2)	0.0941	0.0922(2)	0.0924(3)
a(A)		8.9954	9.0039(5)	9.0351	9.0581(8)	9.0538(7)
c(A)		22.9716	23.080(2)	22.9810	23.070(3)	23.070(3)

† The monoclinic room-temperature structures have been referred to pseudo-hexagonal axes to permit comparison.

* Not yet refined.

** Na(2) is split into two symmetry-independent sites in the monoclinic structures. These are not equally occupied.

BEST COPY AVAILABLE

Table 2. Comparison of "Window" Sizes Along Diffusion Paths in NASICON Solid Solutions $Na_{1+x}Zr_2Si_xP_{3-x}O_{12}$ at Room Temperature and at Elevated Temperature

(a) Path 1 [Na(1) - Na(2)]

	23°C*				275°C	320°C
x = 1.6	0.970,	1.025,	1.125 A	(1.040 A, av.)	-	1.035 A
x = 2.0	0.933,	1.057,	1.139 A	(1.043 A, av.)	1.041 A	1.030 A

(b) Path 2 [Na(2) - Na(2)]

	23°C*				275°C	320°C
x = 1.6	0.963,	1.021,	1.004 A	(0.996 A, av.)	-	1.013 A
x - 2.0	0.923,	1.002,	1.022 A	(0.982 A, av.)	1.021 A	1.009 A

* Three symmetry-independent paths exist between a given pair of species in the monoclinic room temperature structures.

BEST COPY AVAILABLE

coefficients are 1.6 10^{-5} and 3.2 10^{-6} $°C^{-1}$ parallel to and normal to the c axis, respectively. All of the above structural changes, however, include both the discontinuous displacement that accompany the monoclinic to rhombohedral phase transformation and changes caused by thermal expansion. Separation of these two influences must await comparison of phases that are entirely within the field of stability of the rhombohedral structure type.

The refinements provide no evidence for change in the occupancy of the Na sites to the temperatures examined to date. The Na(1) site remains fully occupied. Table 2 compares the computed critical radius of the sphere that could just pass through the oxygen ion configuration that separates neighboring Na(1) and Na(2) sites (path 1) and also two neighboring Na(2) positions (path 2). Detailed comparison with the values in the room-temperature structures is again complicated by the fact that three distinct symmetry independent paths exist in the monoclinic structures. Table 2 accordingly includes an average value for the room temperature windows. The window size found at elevated temperatures is close to the average found for both types of diffusive paths at room temperature as a result of the small magnitudes of the atomic displacement. The radius at elevated temperature, however, varies less from composition to composition than do the radi of the individual paths at room temperature. This suggests that the saddle point configuration at elevated temperatures may be less critically dependent upon composition than is the case at room temperature. Confirmation of these trends must await extension of these analyses to a wider range of compositions and temperature, but the observations seem to have bearing on the reason why the composition of maximum conductivity for the NASICON solid solution system appears to shift with increased temperature.

---

1. L. J. Schioler, B. J. Wuensch and E. Prince, NBS Tech. Note 1178, F. J. Shorten, ed., 42 (1983).

2. B. J. Wuensch, L. J. Schioler and E. Prince, Proceedings of the Conference on High Temperature Solid Oxide Electrolytes Vol. 11 -- Cation Conductors. Brookhaven National Laboratory BNL-51728, 55, October 1983.

3. L. J. Schioler, B. J. Wuensch and E. Prince, NBS Tech. Note 1190, F. J. Shorten, ed., 9 (1984).

BEST COPY AVAILABLE

STRUCTURE OF BARIUM TITANIUM NIOBIUM OXIDES

J. L. Soubeyroux
(CNRS - Laboratoire de Chimie de Solide, Bordeaux, France)
and
(National Bureau of Standards, Gaithersburg, MD)
and
R. S. Roth
(Center for Material Science)
and
A. Santoro

High resolution diffraction measurements have been made on compounds of the ternary system $BaO-TiO_2-Nb_2O_5$. These compounds can be studied particularly well by neutron diffraction techniques because of the high contrast between the scattering lengths of the titanium atoms ($-0.344\ 10^{-12}$cm.) and of the niobium atoms ($0.702\ 10^{-12}$cm.).

The compound $BaTi_{0.89}Nb_{0.085}O_{2.99}$ has the cubic perovskite structure with a = 4.015 A. The titanium and niobium atoms are randomly distributed in the octahedral sites with a mean metal-oxygen distance of 2.07 A.

The compound $Ba_6TiNb_4O_{18}$, also written $Ba(Ti_{1/6}Nb_{4/6})O_3$, is a six-layer arrangement of the perovskite structure. The refinement of the structure has been performed in the R 3m space group with the hexagonal parameters a = 5.7756(1)A and c = 42.409(1)A. The resulting structure leads to a statistical distribution of the titanium and niobium atoms in the octahedral sites. The octahedra share corners to form a five-sequence. The metal-oxygen distances range between 1.83 and 2.19 A, in good agreement with Ti^{4+} and Nb^{5+} ionic radii. A sample of the compound was annealed in order to introduce ordering in the structure. The refinement of this new sample shows no ordering of the metal atoms.

The compound $Ba_8Ti_3Nb_4O_{24}$, also written $Ba(Ti_{3/8}Nb_{4/8})O_3$, is the eight layer repeat sequence. The hexagonal parameters determined are a = 5.7908(3)A and c = 18.853(1)A. The refinement of the structure is in progress.

BEST COPY AVAILABLE

NEUTRON POWDER DIFFRACTION STUDY OF THE STRUCTURE OF THE COMPOUND $Li_{0.31}La_{0.56}MoO_4$

E. Lukacevic, A. Santoro

and

R. S. Roth

(National Bureau of Standards, Gaithersburg, MD)

The structure of the title compound has been analyzed by neutron powder diffraction techniques and by the Rietveld method. The material crystallizes with the symmetry of space group $I4_1/a$. The lattice parameters ae a = 5.335, c = 11.479 A. The framework structure is of sheelite type. The La^{3+} ions are statistically distributed on the sites 4b. The Mo^{6+} ions fully occupy sites 4a and the O^{2-} ions sites 16f with x = .1413, y = .0116, z = .2074 The R-factors at this stage of refinement are R_N = 6.52, R_p = 6.27, R_W = 8.01 and the expected value is R_E = 4.46. There are several possible locations for the Li^+ ions. A likely position would be site 8e with z $\sim$ 3/8. In this configuration the Li^+ ions would be placed halfway, along the c-axis, between the Mo^{6+} and the La^{3+} cations. So far, however, attempts to locate the Li^+ ions have been unsuccesful and refinements of the structure seem to be peculiarly insensitive to the Li^+ positions.

GEOMETRICAL AMBIGUITIES IN THE INDEXING OF POWDER PATTERNS

A. Santoro

It is well known that powder patterns can often be indexed on more than one lattice. In most cases the ambiguities in the indexing are accidental in origin (errors in the measurements of angular positions, extinctions related or unrelated to the symmetry operations of the structure, however, in reflections produced by impurities, etc.). There are cases, however, in which the ambiguities are not accidental but geometrical in nature. These cases arise when two or more different lattices give calculated patterns having the identical number of distinct lines in identical 2θ angular positions. The number of planes contributing to each reflection and the indices hkℓ of the planes are in general different. The lattices which are consistent with the same powder pattern Ae related to one another in a rather simple manner, i.e. by a transformation matrix having simple rational elements. Lattices so related are called "derivative lattices". The problem of geometrical ambiguities has already been studied (1). The previous analysis, however, was based mainly on concepts of number theory and the critical role played by symmetry was not emphasized. Consequently, no general method was given for finding the conditions that

BEST COPY AVAILABLE

lattices must obey in order to generate geometrical ambiguities. A new procedure has now been devised, simpler than the previous one, which allows one to determine also ambiguities that Ae possible only when some types of space group extinctions are present in one of the two structures. This procedure is based on general properties of transformations and on the theory of derivative lattices (2).

---

(1) A. D. Mighell and A. Santoro (1975). J. Apl. Cryst. 8, 372-374.

(2) A. Santoro and A. D. Mighell (1972). Acta Cryst. A28, 284-287.

TEXTURE OF EXTRUDED URANIUM ALLOYS BY NEUTRON DIFFRACTION

C. S. Choi and H. J. Prask
(U.S. Army Armament R&D Center, Dover, NJ)
and
(National Bureau of Standards, Gaithersburg, MD)

It has been reported that extruded uranium/tungsten composites show improved mechanical strength at high extrusion ratios. Since the room-temperature stable phases of uranium alloys (α or α' phase) possess a highly anisotropic crystal structure, the extruded uranium samples are expected to be highly textured, and hence to exhibit anisotropic mechanical properties depending on the orientation texture. We have studied two hydrostatically extruded samples, a U-0.75wt% Ti alloy and a (U-Ti)/W composite alloy. Both samples were extruded in two steps, 6 to 1 area reduction at 600° C followed by 4 to 1 area reduction at 500° C, and have approximate dimensions of 7.6mm in diameter and 40mm in length. Since the pole figure diffractometer had poor instrumental resolution, only three reflections, (111), (112)and (131), were resolved adequately with sufficient intensity for study. All three reflections were used for the texture study of the extruded U-Ti alloy, but only (112) and (131) were used for the composite sample because of the overlapping of the α-U (111) reflection with the W(111) reflection. All of the pole figures showed almost perfect concentric circular contour-lines about the direction of the cylinder axis, which is an indication of fibre texture. The two dimensional pole density distributions were reduced to one-dimensional distributions by averaging the intensity over the φ-angle at each tilt angle, yielding accurate peak positions as shown in figure 1. The observed peak positions should correspond with the angles between the (hkl) plane normals and the fibre axis in an ideal fibre texture. The plane normals for the fibre axes were determined by comparing the observed peaks with the calculated interplanar angles. It was found that the uranium phase of the samples possesses a duplex figure texture with either [010] or [340] as

BEST COPY AVAILABLE

fibre axis. Assuming the orientational distribution of the fibre axes is a Gaussian form, the pole density $P(\rho)$ of an (hkl) reflection with tilt angle ρ_i is given by

$$F(\rho) = I \left[\sum_{i=1}^{n} \frac{N_i}{H_{340} \sin\rho_i} \exp - \frac{A(\rho - \rho_i)^2}{H_{340}^2} + R\{ \sum_{j=1}^{n} \frac{N_j}{H_{010} \sin\rho_j} \exp - \frac{A(\rho - \rho_j)^2}{H_{010}^2} \} \right]$$

where I is a constant related to the total crystal reflectivity, $A = 4\ell n2$, H is the full width at half maxmum, N_i ia the number of equivalent (hkl) planes which have

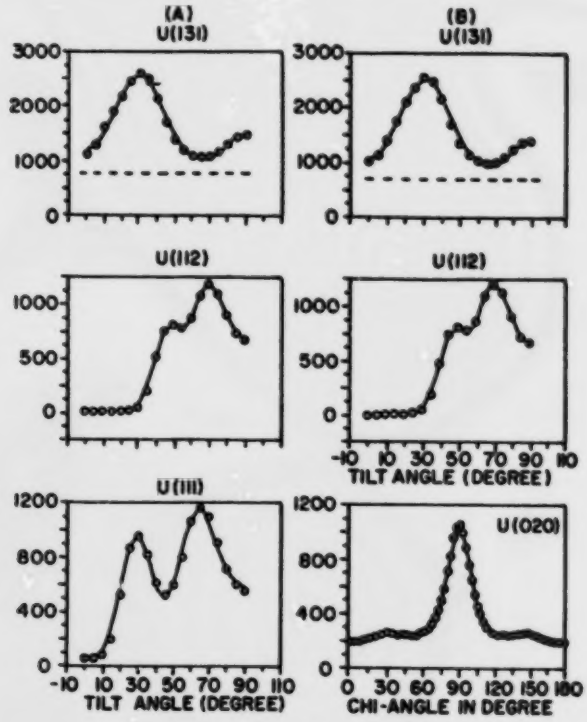

Figure 1. Pole density distributions of the three reflections, U(131), U(112) and U(111), for the two extruded alloys. The small circles refer to the observed values and the solid curves to the calculated distributions based on the [010]/[340] duplex fibre texture. The figures in (A) correspond to (U-Ti) alloy and those in (B) to the composite alloy. The U(020) distribution in (B) is the [010] fibre axis distribution measured directly by the chi-angle rocking of the composite alloy. The dotted lines in the (131) distributions indicate background level added for the refinement.

BEST COPY AVAILABLE

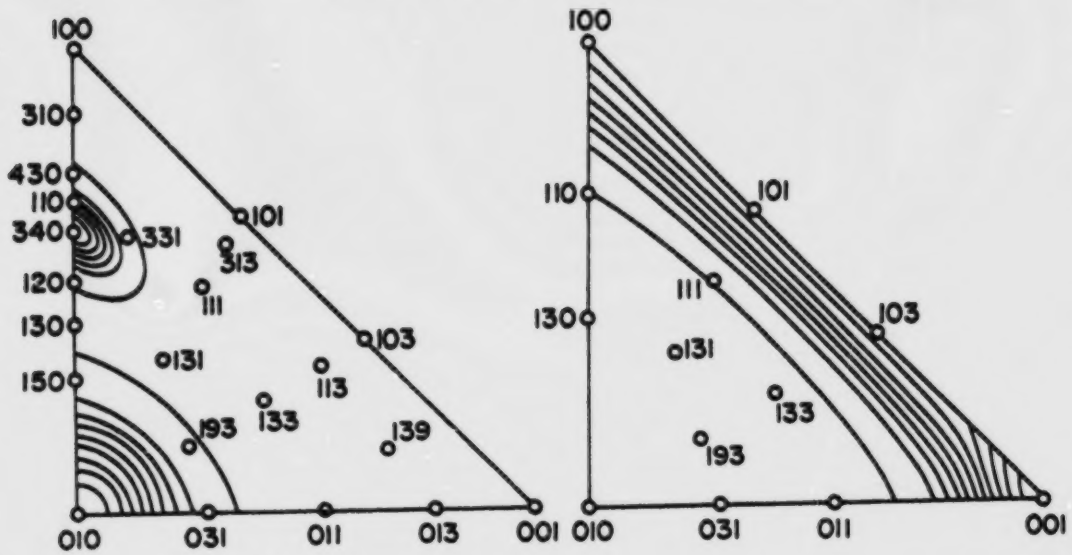

Figure 2. The inverse pole of the uranium phase of the composite alloy, with contour-heights in arbitrary units. The figure at left is the view from the fibre axis direction and that at right is the perpendicular view.

the identical tilt angle ρ_1, and R is a relative frequency of [010] for the fibre axis. The ideal duplex fibre texture model was fitted to the experimental intensity distribution patterns by a non-linear least-squares refinement, with I, H_{010}, H_{340}, and R as adjustable parameters. The calculated profiles agreed very well with the observed as shown in figure 1. This analysis revealed a quantative picture of the orientation distribution; (a) the width of the fibre axis distributions for the two extruded samples were approximately 18° for the [340] fibre axis and approximately 35° for the [010] axis, and (b) the frequency of the [010] axis was about 2.8 times that of the [340] fibre axis.

The pole density distribution as function of tilt angle can be rewritten in generalized form if we use the Miller indices for the expression of the interplanar angles ρ_1 and eliminate the summation operation over the total number of peaks, as follows:

$$F(\rho,hk\ell) = K[(H_{340})^{-1}\exp-A\{(\rho-B_{340})/H_{340}\}^2 + R(H_{010})^{-1}\exp-A\{(\rho-B_{010})/H_{010}\}^2]$$

where, $B_{340} = \text{acos}(3ha^{*2}+4kb^{*2})/\{(9a^{*2}+16b^{*2})^{1/2}q\}$, $B_{010} = \text{acos}(kb^{*}/q)$,

and $q = \{(ha^{*})^2+(kb^{*})^2+(\ell c^{*})^2\}^{1/2}$.

BEST COPY AVAILABLE

The term $\sin\rho_i$ in the pole density distribution function is eliminated in this generalized form because $F(\rho,hk\ell)$ refers to all [hkℓ] poles within the diffraction cone with tilt angle ρ_i. When the tilt angles of the sample are fixed to $\rho=0°$ or 90°, the function gives the number of the [hkℓ] poles oriented with their axes parallel or perpendicular to the fibre axis, respectively. The inverse pole figure viewed from the equatorial direction may be obtained by replacing the arccosine in the B_{340} and B_{010} by an arcsine. Figure 2 shows their inverse pole figures of the α-U phase using the parameters R = 2.8, and the FWHM's in radians (converted from H_{340} = 11°, H_{010} = 21°, the values corrected for the instrumental resolution). The pole densities were projected on the plane defined by the equation: $ha^*+kb^*+\ell c^* = s$, where s is an arbitrary constant . The contour lines are the probability densities on an arbitrary scale, starting from 1 with a step interval of 20.

THE NONDESTRUCTIVE DETERMINATION OF NEAR-SURFACE RESIDUAL STRESSES IN DEPLETED URANIUM ALLOYS

H. J. Prask and C. S. Choi
(U.S. Army Armament R & D Center, Dover, NJ)

and

(National Bureau of Standards, Gaithersburg, MD)

Depleted uranium -0.75 wt% Ti alloy ("DU") has become a principal material for armor-piercing projectiles because of its high density, hardness, ductility, and high ultimate tensile and yield strengths. These properties are achieved by a fabrication process which involves a fast quench to ambient temperature from the γ-phase (~800°C), followed by aging at ~400°C. This yields the desired mechanical properties with the Ti "dissolved" in the single-phase α'-U host lattice. However, optimization of performance has probably not been achieved because of an inability to characterize certain properties in the course of the fabrication process. One of the most important of these is residual stress.

Last year we described a new technique, energy-dispersive neutron diffraction (EDND), by which the first nondestructive characterization of sub-surface residual stress in DU was achieved. (1) Because of the expected susceptibility to stress-corrosion cracking, and because of the difficulties encountered with stress measurements in this material by means of x-ray diffraction, we have sought to extend the EDND stress measurements to the surface region of DU. In the following, results are described for a stress-free, powder test sample and two production-type DU specimens.

BEST COPY AVAILABLE

The details of the application of EDND to sub-surface residual stress measurements have been given in ref. 1. (For convenience, we define "sub-surface" as the sample region in which the differential volume, ΔV, of figure 1 is entirely within the sample.)

What is measured is strain, ε, which is reflected in the change in d-spacing which residual stresses produce:

$$\varepsilon = (d_{hkl} - d^{\circ}_{hkl})/d^{\circ}_{hkl} \qquad (1)$$

where d°_{hkl} represents the stress-free d-spacing of the (hkl) reflection. With reference to the spherical-coordinate geometry of figure 2, measured strain, $\varepsilon'_{\phi\psi}$, is related to residual stress by

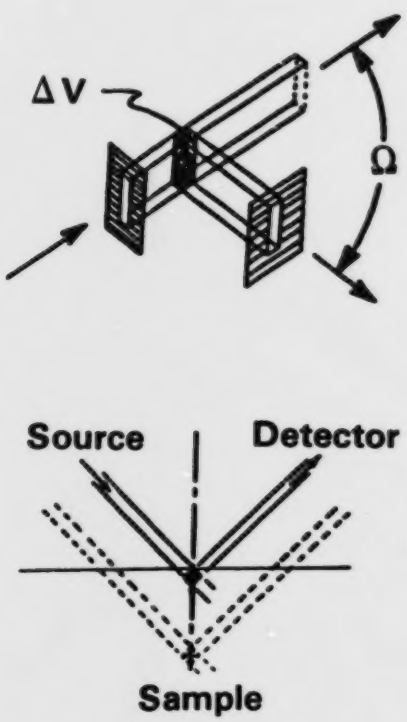

Figure 1. Upper: Perspective schematic showing how absorbing masks (e.g. Cd) can be used with Bragg's Law to define the examined volume, ΔV; lower: plan view of movement of ΔV through the (translated) sample.

BEST COPY AVAILABLE

$$\varepsilon'_{\phi\psi} = 1/2\ S_2(hkl)[\sigma_{11}\cos^2\phi\sin^2\psi + \sigma_{22}\sin\phi^2\sin^2\psi$$

$$+ \sigma_{33}\cos^2\psi + \sigma_{12}\sin2\phi\sin^2\psi + \sigma_{13}\cos\phi\sin2\psi \qquad (2)$$

$$\sigma_{23}\sin\phi\sin2\psi] + S_1(hkl)[\sigma_{11} + \sigma_{22} + \sigma_{33}].$$

The $S_1(hkl)$ are "diffraction elastic constants" which, in general, depend on the reflection studied.

For this initial study, several assumptions are made to extract stresses from the measured strains. We assume that the principal axes of stress in the sample coincide with the cylindrical geometry so that $\sigma_{12} = \sigma_{13} = \sigma_{23} = 0$. We also assume elastic isotropy in the sample such that

$$1/2\ S_2(hkl) = (1 + \mu)/E \text{ and } S_1(hkl) = -\mu/E \qquad (3)$$

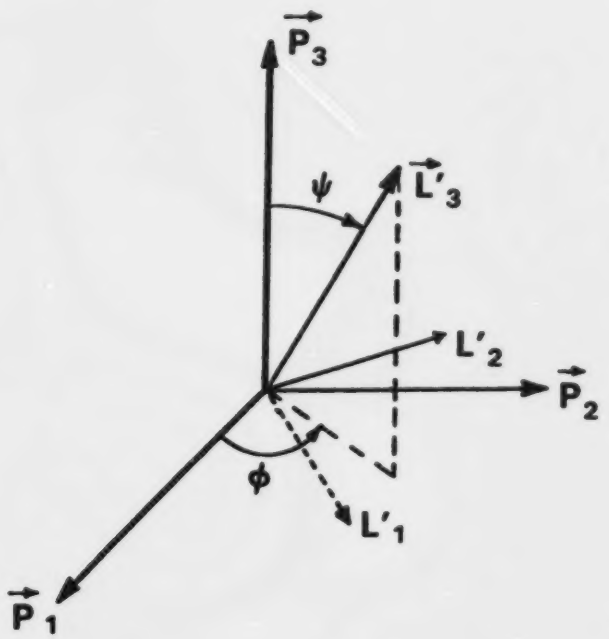

Figure 2. Specimen (P_i) and laboratory (L_i) corrdinates at a point in the specimen. The L'_3 or probe, direction coincides with the momentum transfer direction $\vec{k}$ or $\vec{Q}$; P_3 Corresponds to the cylinder axis.

BEST COPY AVAILABLE

where μ and E are Poisson's ration and Young's modulus, respectively.

At the surface, overall equilibrium requires that the stress normal to the surface be zero. With this and the assumptions described we have at the surface

$$\varepsilon'_{\phi\psi} = [(1 + \mu)/E](\sigma_{\theta\theta}\sin^2\phi\sin^2\psi + \sigma_{zz}\cos^2\psi) - [\mu/E](\sigma_{\theta\theta} + \sigma_{zz}). \quad (4)$$

To test for anomalous shifts in peak positions arising from geometric effects, we examined a copper powder in the same cylindrical geometry as the DU samples: 10 cm long by 2.38 cm in diameter. The ΔV for both copper and DU was nominally 1.5 cm 0.17 cm x 0.17 cm with the long dimension aligned parallel to the cylinder axis. Although microstresses might be present in the individual grains of copper powder, measured d-spacings should be identical at any point in the powder unless instrumental effects distort the measurements.

For copper, we examined the (111) reflection at a scattering angle of 90° at several positions in the sample. In figure 3 we show in a partial plan view the examined differential-volume cross-sections and the beam-in/beam-out bisector or $\vec{\kappa}$

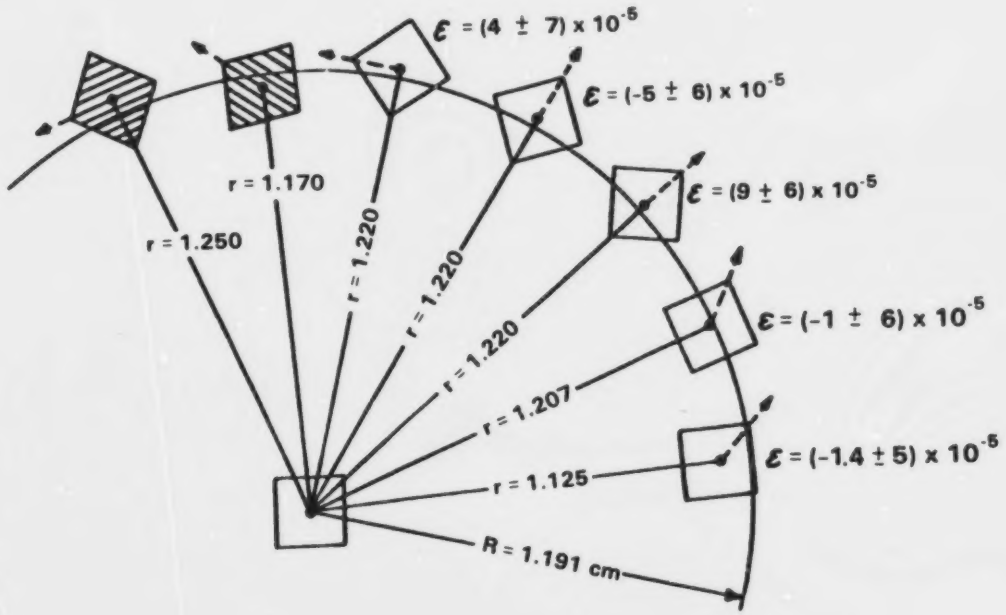

Figure 3. Cross-sections of ΔV, drawn to scale relative to the sample cross-section, for copper powder (open squares) and production-type DU (cross-hatched parallelograms) near-surface measurements. The arrows indicate the $\vec{k}$-direction for each measurement. Measured strains, ε, are shown for the copper powder.

BEST COPY AVAILABLE

direction. Measured strains which are also shown in the figure were determined in the following way. Several measurements of the d-spacing were made at the sample center. The weighted mean of these yielded "d°" = 2.08714 ± 0.00010 A. Strains at the near-surface positions shown in figure 3 were then calculated according to eq (1) from the d-spacings measured at these points. Measured strain values are obtained without any assumptions or approximations.

In this test case, if instrumental effects do not distort the measurements the measured strains should all be zero. It is most interesting that for the five points examined, only at one does the strain differ from zero by more than a standard deviation. It is also most important that even for differential volumes more than half of which are outside the sample the strains --with the one exception-- are zero within one standard deviation. Although these measurements do not represent a complete test of the EDND technique for near-surface studies, the results were sufficiently encouraging to begin preliminary studies of production type DU samples.

One area of considerable current interest relating to DU-0.75 wt% Ti penetrator fabrication is the effect of different processing techniques on surface residual stresses and stress-corrosion susceptibility. Two process variations which are currently being studied are rolled bars solutionized in an AVS furnace (DU-AVS) and rolled bars solutionized in an induction furnace (DU-I). Subsequent processing steps include quick-quenching, aging, and rotary straightening for both samples.

At the surface, four sets (90° apart) of two measurements were made with $\vec{\kappa}$ in the r-θ plane. Because of an instrumental shift not recognized until data collection was completed, the two measurements made at each 90° position did not coincide exactly. They differed in their position relative to the surface as shown in figure 3. However, since exactly the same problem occurred with both samples, the measurements were analyzed as if no shift had occurred. In this case the (111) reflection of DU was examined at a scattering angle of 82°. For this reason the ΔV cross-section is a parallelogram rather than a square as for copper at 90°.

To obtain the near-surface residual stresses eq (4) is used, d° is known for each sample from powder diffraction measurements so that both $\sigma_{\theta\theta}$ than σ_{zz} could be obtained from measurements with $\vec{\kappa}$ in the r-θ plane; however, since the angle is near 90° the measurements are much more sensitive to $\sigma_{\theta\theta}$ and σ_{zz}. For the present we evaluate only $\sigma_{\theta\theta}$. The results for the two samples are shown in figure 4.

As expected for a quenched cylinder, measured hoop stress on the surface is compressive. However, the AVS and induction furnace samples exhibit quite different stress distributions around the circumference. It is interesting that for both

BEST COPY AVAILABLE

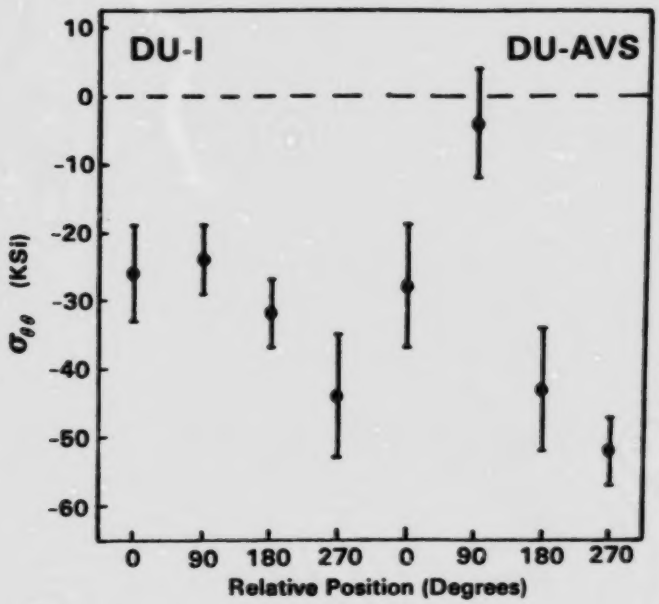

Figure 4. Preliminary results for near-surface hoop stresses for induction and AVS furnace solutionized Du. Measurements were obtained at 90° intervals around the circumference of the cylindrical samples with arbitrary zero position.

samples the average hoop stress is approximately 32 KSI; however, the variation about the average is considerably greater for the AVS-furnace sample. To minimize susceptibility to stress-corrosion cracking, it is imperative that the surface stresses be (highly) compressive. In this regard it is of concern that one of the AVS-furnace measurements approaches the tensile stress region. Follow-up measurements are planned to characterize these samples more definitively.

---

1. H. J. Prask and C. S. Choi, NBS Tech Note 1190, 31-34 (1984); NBSIR 84-2815, 53-56 (1984); J. Nucl. Matls., 126, 124-131 (1984).

BEST COPY AVAILABLE

REACTOR RADIATION DIVISION AND COLLABORATIVE PROGRAMS

CRYSTAL DATA

V. Himes, J. Stalick and A. Mighell

and

J. Rodgers
(National Research Council of Canada, Ottawa, Canada)

The NBS Crystal Data Center maintains a data base that contains evaluated crystallographic and chemical data on approximately 80,000 materials. The data fall into the following categories: organics, organometallics, metals, intermetallics, inorganics and minerals. During the year the data base has been significantly upgraded and expanded. Approximately 16,000 existing inorganic entries have been upgraded, processed by NBS*AIDS83, evaluated and added to the data base. In addition, ~5,000 organic entries corresponding to recently published data have been added.

There are two fundamental ways that large crystallographic data bases can be used. As a source of critically evaluated data, the data base can be used as a basis for scientific research or as an aid to research. To permit scientists to utilize the data base, we have developed software tools that can be distributed with the data base or used to search the data base on-line at a central site.

NBS search software, which became an integral part of the Crystal Data Distribution Package in June, 1985, is designed to be used on a variety of computers. With the lattice-matching algorithm, unknown compounds can be identified by comparison with entries in the data base. The method can be used once a cell has been determined from a single-crystal or from a powder sample using diffraction techniques. In addition, various types of lattice relationships between materials can be readily established. The lattice-matching method offers a comprehensive technique to characterize solid-state materials and is now in routine use at the National Bureau of Standards, in industrial analytical laboratories, and by crystallographic data centers.

The on-line search system is based on scientific software written both at NRC and NBS, coupled with IBM systems software (the IBM host computer is located at the National Research Council of Canada). Using Telenet or the equivalent, the NBS Crystal Data File can be accessed on-line by scientists anywhere in North America or Europe. This system permits search and retrieval of any given data item or combination of items using Boolean operations. The type of data that can be searched include chemical name and formula, cell parameters, cell volume, crystal system, space group symbol and number, density, bibliographic data, chemical class, plus

BEST COPY AVAILABLE

additional data. During the year, this system has been used by the NBS Crystal Data Center and by individual scientists to solve a variety of scientific problems in diverse areas of chemistry and solid-state physics.

LOCAL MODES IN DILUTE METAL-HYDROGEN ALLOYS

J. J. Rush and J. M. Rowe

and

A. Magerl

(Institute Laue-Langerin, Grenoble, FRANCE)

Data analysis has been completed on the measurements of local vibrational modes of hydrogen bound in vanadium, niobium and tantalum in the dilute α-phases. These experiments were performed on the BT-4 spectrometer, using the high-intensity, low-background beryllium detector analyzer and a Cu-220 monochromator. They provide the first direct information about the microscopic mechanism leading to large linewidths for the local modes in these dilute metal-hydrogen alloys.

Figures 1 and 2 show neutron spectra measured at room temperature for $VH_{0.012}$, $NbH_{0.03}$ and TaH_x with x = 0.180 and x = 0.037 (fast neutron background has been subtracted). These spectra reveal several highly unusual features: (1) The widths of the vibration peaks are in every case considerably wider (≥ 10 meV) than the instrumental recalcitron, in contrast to the very narrow linewidths anticipated for the vibrations of dilute interstitial defects. The spectral peaks (two modes are expected for H in a bcc tetrahedral site, one at low-energy and a doubly degenerate mode at higher energy) are most broadened for $VH_{0.012}$, with somewhat smaller but still substantial widths observed for H in Nb and Ta. The "peak" energies in meV observed at 295 K for the three α-phase samples are: 106 and ~170 ($VH_{0.012}$), 107 and 163 ($NbH_{0.03}$) and 114 and 154 meV ($TaH_{.037}$). A second unusual feature of these results is that the high energy mode peak for TaH_x (fig. 1) increases in energy from: 154 to 163 meV as x is changed from 0.03 to 0.18, while the lower energy mode remains unchanged. A third striking aspect shown in figure 2, is the anomalous shift of the lower excitation peak in $NbH_{0.005}$ to higher energy as the temperature is lowered toward the α-δ phase boundary.

After careful anlysis of the results in figures 1 and 2 and comparison with earlier experimental work on high hydrogen concentration α' phase samples and H trapped by impurities in Nb[2-4] and with theoretical predictions[5], we conclude that the broad vibratonal linewidths are associated with a delocalization of the excited vibrational states of the interstitial defects. In fact an estimate of the ground

BEST COPY AVAILABLE

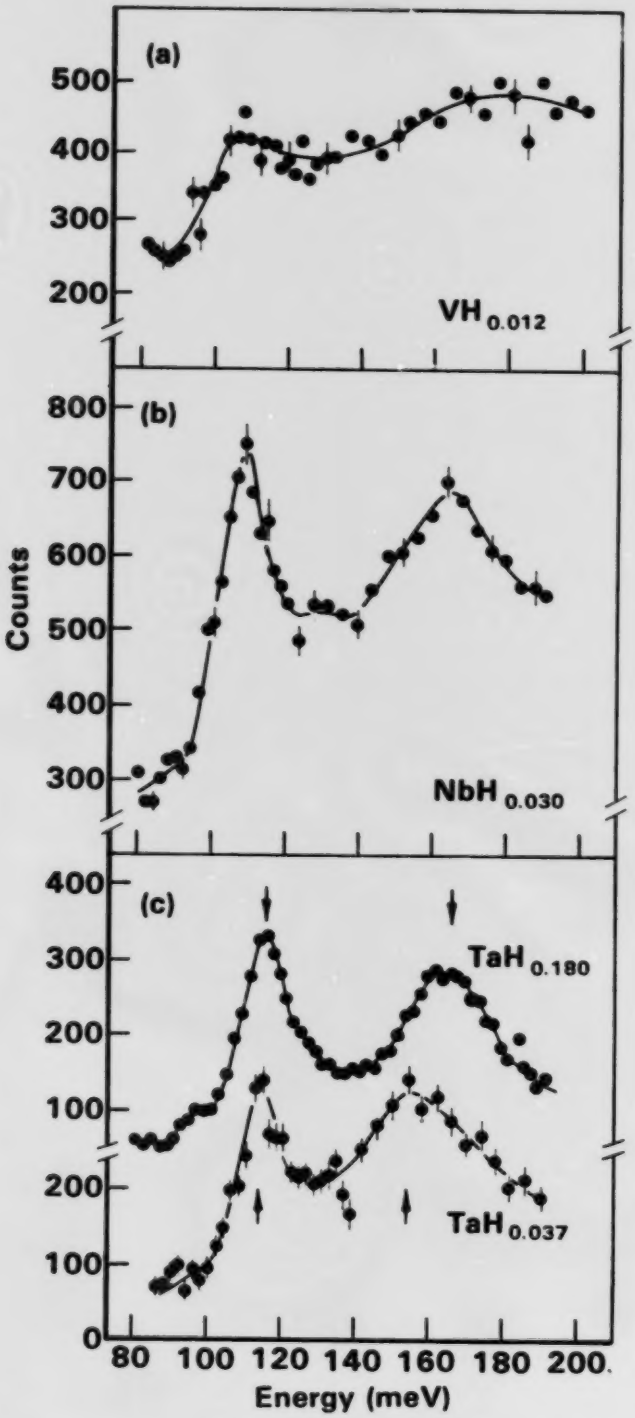

Figure 1. Spectra of local H modes measured at room temperature.

BEST COPY AVAILABLE

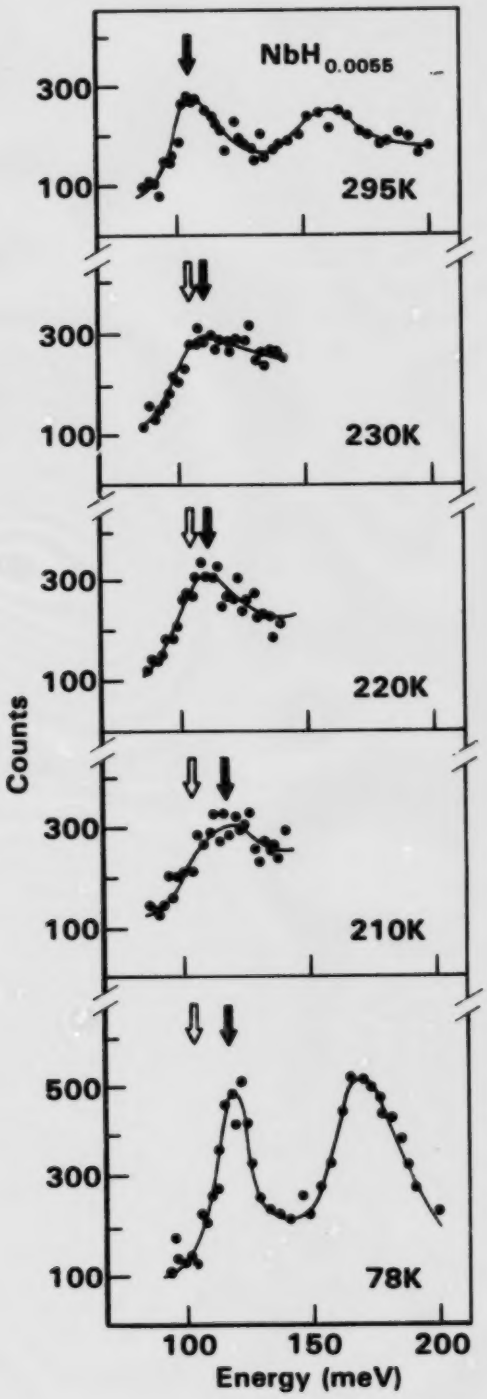

Figure 2. Temperature dependence of local H modes in $NbH_{0.0055}$. The $(\alpha|\alpha + \delta)$ phase boundary is at ~ 200 K. The solid arrow shows the actual "peak" position vs. T and the open arrow indicates the position at 295 K.

BEST COPY AVAILABLE

state tunnel spittling for self trapped protons in refractory metals suggests excited state "splittings" ~10 meV, which is in qualitative agreement with our observations. The anomalous shift of the low-energy density-of-states band for $NbH_{.005}$ toward the position of the ordered (δ) phase peak strongly suggests the existence of fluctuating hydrogen short range order resembling the ordering in the low temperature phase. Such "ordering" has never been directly observed over such a wide temperature range (~40° K) above the ordering phase transition. All these results are being combined in a paper to be submitted to Phys. Rev. B.

---

1. D. Richter and S. M. Shapiro, Phys. Rev. B, 22, 599 (1980), and R. Hempleman, D. Richter and A. Kollmar, Z. Phys. B, 44, 159 (1981).

2. A. Magerl, J. J. Rush, J. M. Rowe, D. Richter and H. Wipf, Phys. Rev. B, 27, 927 (1983).

3. D. Richter, J. J. Rush and J. M. Rowe, Phys. Rev. B, 27, 6227 (1983).

4. H. Wipf, et.al, Phys. Rev. Lett., 46, 947 (1981).

5. R.C. Casella, Phys. Rev. B, 27, 5943 (1983).

NEUTRON SCATTERING STUDIES OF HYDROGEN IN YTTRIUM

I. S. Anderson
(University of Maryland)
and
(National Bureau of Standards, Gaithersburg, MD)
and
T. J. Udovic, J. M. Rowe, and J. J. Rush

The dynamics of the yttrium-hydrogen system in the hcp solid solution phase has been studied in order to determine the hydrogen site occupation. There are two pairs of sites with tetrahedral symmetry and one pair of sites with octahedral symmetry in the yttrium unit cell aligned along the c direction, and although neutron diffraction studies[1] have shown that the tetrahedral sites are predominantly occupied, recent neutron energy loss measurements have shown evidence of multiple site occupancy (though the oxygen impurity levels in the yttrium samples were not known). In an attempt to clarify the possible occupancies, we have made neutron energy loss measurements to study the local vibrations of hydrogen in well-characterized yttrium samples with varying amounts of oxygen and hydrogen. A typical spectrum taken on the BT4 spectrometer at the NBS reactor operating with a cooled Be filter analyzer is shown in figure 1. For all the samples studied, two peaks were observed centered at

BEST COPY AVAILABLE

101 and 135 meV with no clear evidence of a second harmonic of the 100 meV peak. The peak at 135 meV can be associated with hydrogen in a regular tetrahedral site and the energy width of his peak was in all cases limited by the resolution of the instrument. The origin of the peak at 100 meV is however unclear, the energy being somewhat higher than would be expected for hydrogen in an octahedral site. The relative intensities of the two peaks do not depend directly on oxygen concentration indicating that oxygen trapping of the hydrogen does not give rise to the vibration at 100 meV. Moreover from the known concentrations, one would have to explain the trapping of 50 or more protons by each oxygen. However, on removing some hydrogen from the sample under vacuum at 750°C the intensity of the peak at 135 meV was reduced whereas the intensity of the peak at 100 meV remained unchanged. This suggests that the origin of the latter peak is due to hydrogen which is more tightly bound in the system. There is evidence that the relative intensity of the peak at 100 meV increases with time when the sample is left at room temperature.

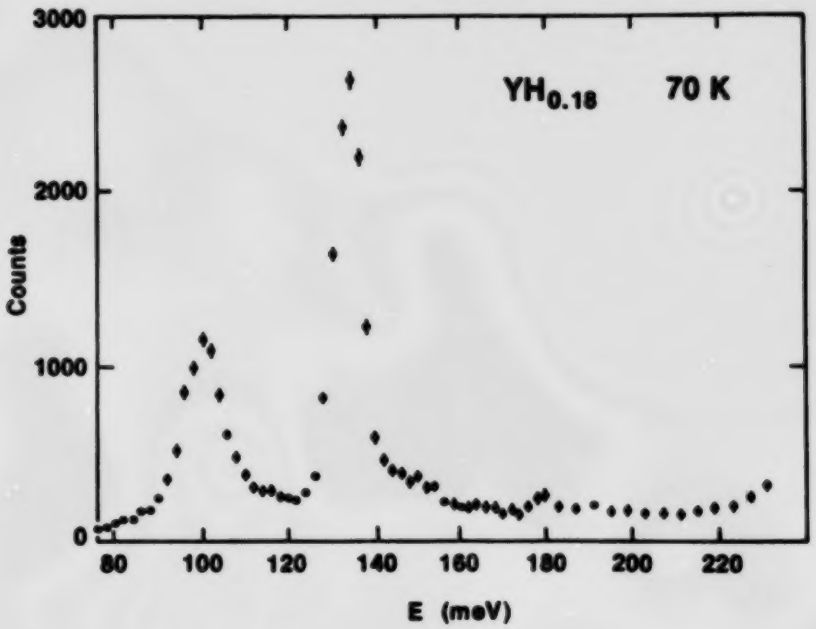

Figure 1. Typical neutron energy loss spectrum showing two local mode frequencies in $YH_{0.18}$.

BEST COPY AVAILABLE

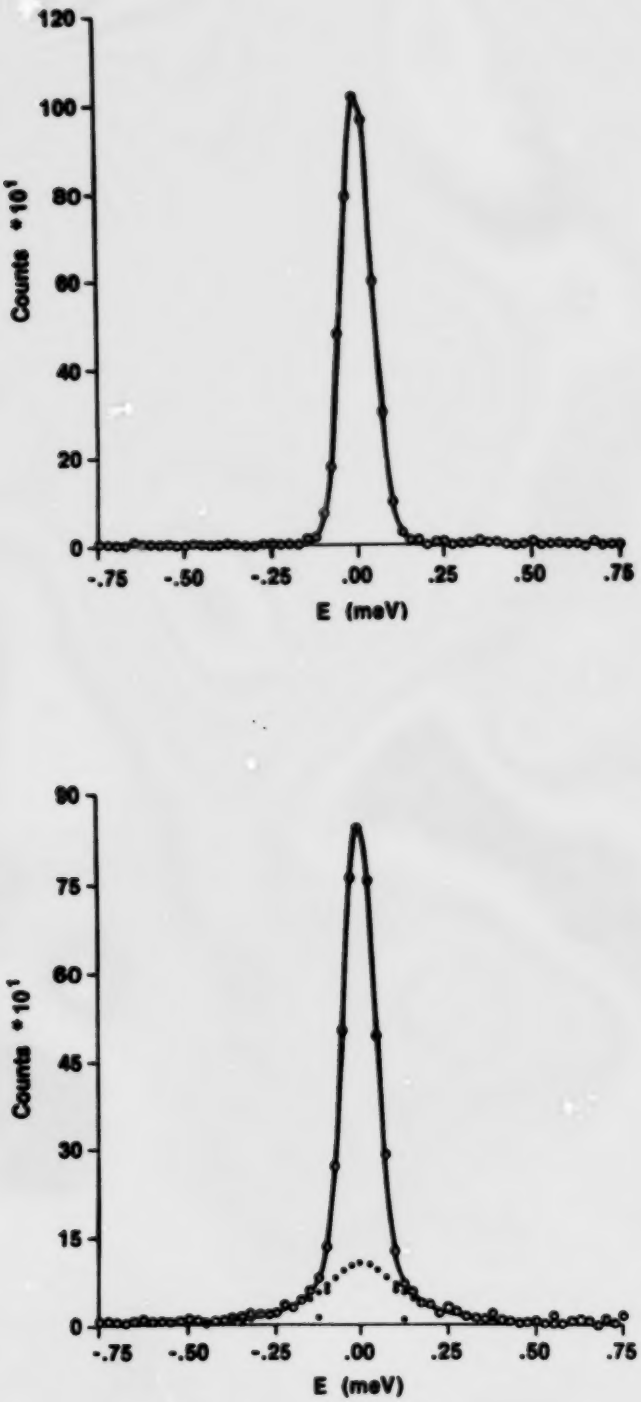

Figure 2. Quasielastic spectra from a single crystal of $YH_{0.2}$ a) Q //<1$\bar{2}$10>, b) Q //<0001>.

BEST COPY AVAILABLE

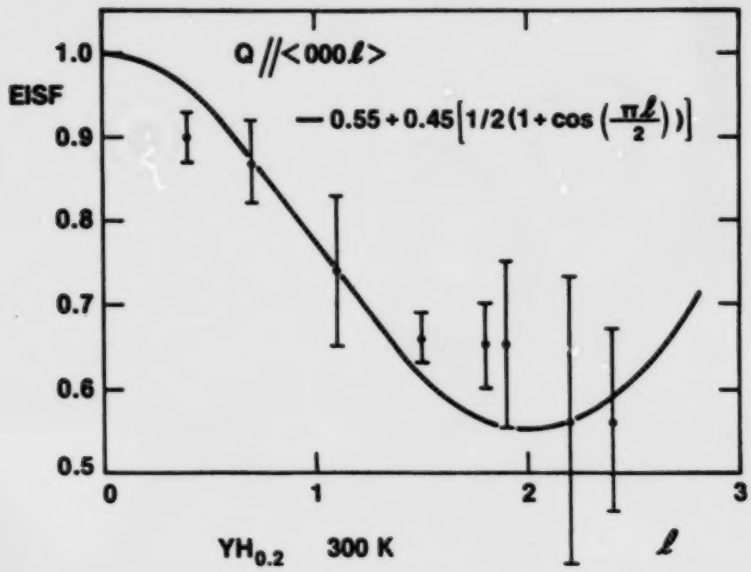

Figure 3. Elastic incoherent structure factor for $YH_{0.2}$ at 300 K. The solid line is a model calculation for jumps between two equivalent sites allowing only 45% of the hydrogen to occupy these sites.

Earlier measurements[2] of the diffusion of hydrogen in yttrium indicated the existence of a local hopping motion of hydrogen probably between pairs of tetrahedral sites. The BT4 spectrometer was used in its triple-axis mode to study the quasielastic scattering due to this local hydrogen motion in single crystals of yttrium at room temperature. Figures 2a and 2b show typical spectra taken with the momentum transfer vector Q perpendicular and parallel to the c axis respectively. Although there is no quasielastic intensity when Q is perpendicular to the c axis, there is clear quaiselastic intensity measured parallel to this axis showing that the motion involves jumps along the c direction. Moreover, the Elastic Incoherent Structure Factor (EISF) shown in figure 3 is well described by a model for jumps between pairs of tetrahedral sites if only a fraction 0.45 of the hydrogen atoms are involved. A neutron energy loss measurement on the same crystals showed that the relative intensity of the peak at 135 meV was also of the order of 0.45 indicating that the hydrogen giving rise to the peak at 100 meV was not involved in the local motion.

---

1. D. Khatamian, C. Stassis and B. J. Beaudy, Phys. Rev. B23, 624 (1981)

2. I. S. Anderson, A. Heidemann, J. E. Bonnet, D. K. Ross, S. K. P. Wilson, and M. W. McKergow, J. Less. Comm. Metals, 101, 405 (1984).

BEST COPY AVAILABLE

STOCHASTIC STATES THEORY OF NEUTRON SCATTERING FROM SELF-TRAPPED DEFECTS IN SOLIDS.

N. F. Berk

We are investigating a stochastic states theory for the energy and wavevector resolved spectrum of neutron scattering from self-trapped defects, such as hydrogen, in solids. The basic idea of the model is illustrated by the two reflection equivalent, aysmmetric double-well potentials in figure 1, which represent the vibrational potentials of a defect self-trapped in the deeper of the two wells or pockets: either in the right hand well, as shown in 1, or in the left hand well, as in 2. Self-trapping on either side of the double well is described by the asymmetry of the potential, where the asymmetry parameter ε is taken to be the measure of the local self-induced strain--or self-trapping--energy. Were the defect to remain indefinitely in one of these neighboring configurations, say 1, its vibrational spectrum would be determined by the rigid asymmetric potential, and neutron scattering would reveal a sharp inelastic peak at energy E of the tunnel-split ground-to-first-excited-state transition. Since the two potentials have identical spectra, a static distribution of self-trapping configurations, 1 and 2, would provide the same neutron spectrum as either one acting alone. The axiom of the present model, however, is that unless either configuration is stabilized by external forces, the system (solid + defect) undergoes diffusive--i.e., nonadiabatic, incoherent--transitions between the two stochastic states 1 and 2 at a rate given by the model parameter λ, which measures the effective hopping rate of the defect. The vibrational Hamiltonian of the system is now time-dependent: $H(t) = H_{\xi(t)}$, where $\xi(t)$ is a Markov process on $\{1,2\}$, and H_1 and H_2 are the Hamiltonian operators for the respective stochastic states. Because of the spatial displacement of the asymmetry distinguishing 1 from 2, H_1 and H_2 are noncommuting, $[H_1,H_2] \neq 0$, and so are not simultaneously diagonalizable. The defect, therefore, cannot stay in an eigenstate of one or the other potential, 1 or 2, and the spectrum of neutron scattering will be modified by the random potential well flipping that we take as a model for the hopping between the neighboring self-trapped configurations.

The consequences of the model for neutron scattering are worked out most naturally in the stochastic states superoperator formalism developed by Blume[1], and by Dattagupta and Blume[2], and further elucidated recently by Berk, et al.[3] In compact superoperator notation, the neutron scattering intensity is proportional to

BEST COPY AVAILABLE

$$I(Q,\omega) = \underline{\mathrm{Re}}(e^{iQr}|\bar{U}[i\omega]|e^{iQr}) \qquad (1)$$

where $\bar{U}[i\omega]$ is the Laplace transform of the average of the time-development superoperator

$$U(t) = \exp[i\int_0^t H^X(\tau)d\tau] \qquad (2)$$

where H^X is the Hamiltonian superoperator (Lioville operator), $H^XA = [H,A]$, and where $(A|B) = trA^\dagger$ for arbitrary operators A and B. As a first trial of these notions we have limited ourselves to the simplest case where both stochastic states are described by a two-level tunneling system. Thus, in the pocket-state (left-right) representation

$$H_{1,2} = -\delta S_x \pm \varepsilon S_z \qquad (3)$$

where S_i, i = x,y,z, are the Pauli spin-1/2 operators and where δ is the tunnel splitting for the limit of a symmetric potential; $E = \sqrt{(\delta^2 + \varepsilon^2)}$. The position operator in this representation is $r = 2aS_z$, where 2a is the distance between the two wells or pockets. In this model (1) can be worked out explicitly, and we find the formula (for the case 1 and 2 have equal <u>a priori</u> probabilities)

$$I(Q,\omega) = 2\lambda\varepsilon^2\delta^2\sin^2Qa/[\omega^2(\delta^2 + \varepsilon^2 - \omega^2)^2 + \lambda^2(\omega^2 - \delta^2)^2]. \qquad (4)$$

The ω-dependence of (4) is shown in figure 2 for fixed $\delta = \varepsilon = 1$ and a range of hopping rates λ. For $\lambda \to 0$, the spectrum consists of lifetime broadened inelastic line at $\omega = E = \sqrt{2}$ and a quasielastic peak at $\omega = 0$. As λ increases both lines broaden and the inelastic peak moves toward lower energies. Then as λ continues to increase, $\lambda >> \varepsilon$, the quasielastic scattering becomes too broad to observe, while the inelastic line motionally narrows and moves asymptotically toward the tunneling

BEST COPY AVAILABLE

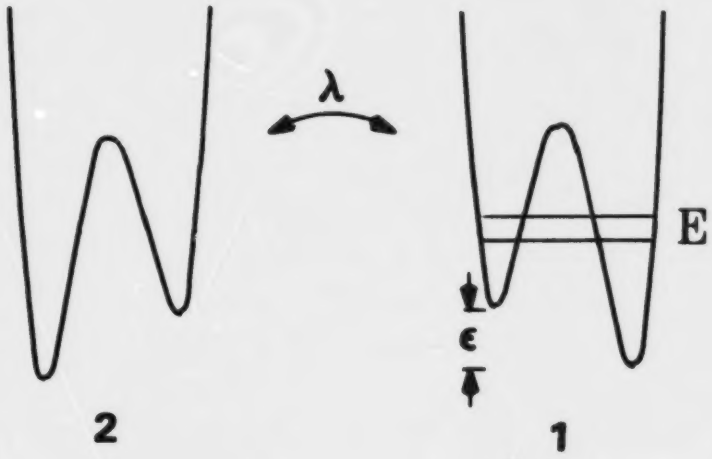

Figure 1. Stochastic states, /1/ and /2/, representing neighboring self-trapped configurations of a double-well defect vibrational potential. The model assumes random potential well flips at a rate λ.

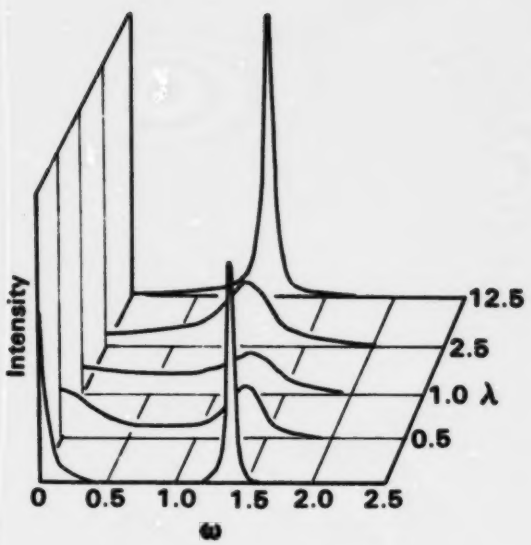

Figure 2. Neutron scattering intensity obtained from (4).

BEST COPY AVAILABLE

transition energy for the averaged Hamiltonian $\bar{H} = (H_1 + H_2)/2$, $E = \delta = 1$. The behavior of (4) is indicated succinctly in terms of the intensities at the special frequencies $\omega = 0$, δ, and E. Thus, suppressing common factors,

$$I(0) = (\epsilon/\delta)^2/\lambda,$$

$$I(\delta)/ = \lambda/\epsilon^2, \text{ and}$$

$$I(E) = (\delta/\epsilon)^2/\lambda. \qquad (5)$$

In particular, (5) shows the strong sensitivity of the relative intensities to ϵ; as ϵ increases, intensity shifts rapidly -- as ϵ^4-- into the quasielastic line. Since the model treats the hopping phenomenologically, there are no built-in constitutive relations among the parameters to delimit their ranges of variation, and not all of the behavior indicated in figure 2 may be physically meaningful in the given application. This important aspect of the problem remains for futher investigation, along with extensions to various degrees of complexity such as multi-level, multi-stochastic state generalizations.

---

1. M. Blume, Phys. Rev. 174, 351 (1968).
2. S. Dattagupta and M. Blume, Phys. Rev. B 10, 4540 (1974).
3. N. F. Berk, J. Rosenthal, and L. Yarmus, Phys. Rev. B 28, 4963 (1983).

BEST COPY AVAILABLE

THEORY OF PROCESSES CONTRIBUTING TO QUASIELASTIC NEUTRON SCATTERING FROM HYDROGEN IN METALS

R. C. Casella

I have investigated the role of thermally assisted virtual transitions of dilute hydrogen in metals from localized-oscillator ground states to excited-oscillator band states at temperatures such that direct excitations thereto are negligible ($k_B T \ll \Delta$, where Δ is the hydrogen-oscillator excitation energy). These processes can contribute to the line widths of quasielastic neutron scattering from such materials. The analysis applies to the absorption and concomitant emission of any type of bosonic mode which interacts with the hydrogen in the presence of a heat bath at temperature T. Letting $(1/\tau)$ be the nearest-neighbor jump parameter which appears in the Chudley-Elliott expression for the neutron quasielastic linewidth, I obtain

$$\frac{1}{\tau} = G^4 \, |\varepsilon(\vec{\ell})|^2 \sum_Q \sum_{Q'} \left(\frac{1}{\Delta - \omega_Q}\right)^2 \left(\frac{1}{\Delta - \omega_{Q'}}\right)^2 \left(\frac{1}{4 \sinh^2 \left(\frac{\beta\omega_Q}{2}\right)}\right) \delta(\omega_Q - \omega_{Q'}), \qquad (1)$$

where

$$\varepsilon(\vec{\ell}) = \frac{1}{N} \sum_{\vec{k}} e^{i\vec{k}\cdot\vec{\ell}} \, \varepsilon(\vec{k}). \qquad (2)$$

Here $\varepsilon(\vec{k})$ describes the excited-oscillator energy-band dispersion in tight-binding approximation,[1,2] $\vec{\ell}$ is a nearest-neighbor interstitial displacement, Q denotes the interacting boson mode, $\beta = (1/k_B T)$, and G is a coupling constant with the dimension of energy ($\hbar = 1$). The second-order process which contributes to $(1/\tau)$ involves (i) absorption of a boson of energy ω_Q, leading to (ii) virtual excitation of the hydrogen from the local oscillator ground state at $\vec{x} = \vec{0}$ to an excited band state with energy $\Delta + \varepsilon(\vec{k})$, followed by (iii) deexcitation to a local state at $\vec{x} = \vec{\ell}$, accompanied by (iv) emission of a boson of energy $\omega_{Q'}$. When the boson spectrum consists mainly of a narrow band of half-width γ centered at $\bar{\omega}$, Eq.(1) reduces to the approximate form

$$\frac{1}{\tau} = \left(\frac{g^4 \, \bar{\omega}^{-4} \, |\varepsilon(\vec{\ell})|^2}{2\gamma \, (\Delta - \bar{\omega})^4}\right)\left(\frac{1}{4 \sinh^2 \left(\frac{\beta\bar{\omega}}{2}\right)}\right). \qquad (3)$$

For $\beta\bar{\omega} > (\sim 1)$, the second factor in Eq.(3) takes on the approximate form

$$e^{-\beta\bar{\omega}} + 2 \, e^{-2\beta\bar{\omega}}, \qquad (4)$$

BEST COPY AVAILABLE

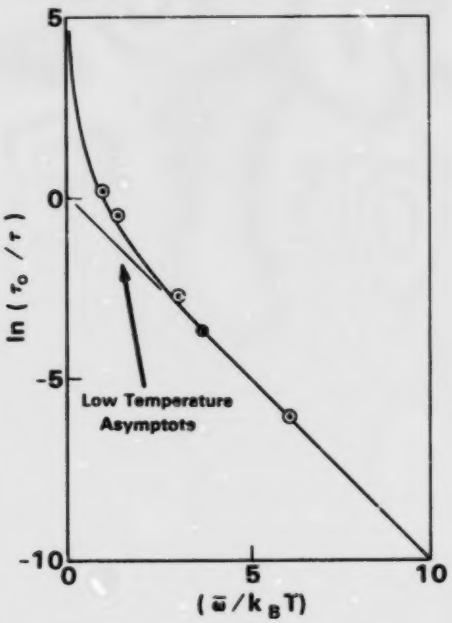

Figure 1. Temperature dependence of the jump parameter $(1/\tau)$. $\ln(\tau_0/\tau)$ vs. $\bar{\omega}/k_B T$. The curve depicts the theoretical result given by the second factor in Eq. (3) of the text. The first factor in eq (3) equals $1/\tau_0$ and is chosen to give agreement with experiments (reference 3) on dilute hydrogen in niobium at T = 212K [●]. A few other data points[3] are also indicated [⊙].

which exhibits a break in the plot of $\ln(1/\tau)$ vs. $(1/T)$. The theoretical temperature dependence in eq (3) is shown in figure 1, where comparison is made with data[3] for dilute hydrogen in niobium. The agreement is only qualitative and worsens at the higher temperatures, where multiexcitations enter and real transitions to the excited hydrogen band states can begin to occur. The boson peak energy, $\bar{\omega}$ = 68 meV, is chosen to fit the low temperature data[3] where the first term in eq (4) is adequate. This energy is considerably greater than the hard part of the niobium phonon spectrum (≈ 20 meV). The physical nature of the bosons is not clear, nor is their relative transparency to the neutron probe. Within the model, values of the dimensionless coupling constant g appearing in eq (3) are consistent with the data for τ with $g^2 \lesssim 1$. Work is continuing in this area.

---

1. R. C. Casella, Phys. Rev. B 27, 5943 (1983).

2. R. C. Casella, Phys. Rev. B 28, 2927 (1983).

3. J. Völkl and G. Alefeld, in Hydrogen in Metals I (ed., G. Alefeld and J. Völkl, Springer-Verlag, New York, 1978), p.330.

BEST COPY AVAILABLE

TRANSLATION-ROTATION COUPLING - ALKALI CYANIDE/ALKALI HALIDES

J. Bouillot
(University of Maryland)

and

F. Luty
(University of Utah)

and

K. H. Michel
Universiteit Instelling Antwerp

and

J. M. Rowe

The structure work on mixtures of alkali cyanide/alkali halide has been extended to $(KCN)_x(KCl)_{1-x}$ with x=0.8 and 0.9 as a function of temperature. In addition, the data for $(KCN)_x(KBr)_{1-x}$ has been re-analysed, allowing for the presence of a triclinic phase as suggested by x-ray data. As a result of this additional work, the phase diagram of the mixed crystals has now become reasonably clear, although some problems remain in the interpretation of the data. It is now well established that the mixed crystals go from the cubic high temperature phase to a monoclinic phase, and that at high concentrations ($x > 0.9$ for KCN/KBr; $x > 0.8$ for KCN/KCl), a mixed phase develops, with a triclinic phase and an orthorhombic phase co-existing. It has further been established that electric dipole order is only established in the orthorhombic phase - neither the pure cyanides (RbCN, CsCN) nor the mixed crystals in any ordered phase except the orthorhombic (KCN/KBr, KCN/KCl) ever show electric dipole order at any temperature. The peak shapes observed for the mixed crystals suggest the presence of strain, and this in turn implies that sample history may well influence the observed phase transitions.

We are also beginning a study of the $(RbCN)_x(RbBr)_{1-x}$ system, in which the pure RbCN transforms to a monoclinic structure at low temperatures, in the hope that this system will be less complex, and therefore more susceptible to detailed analysis. In addition, we are preparing $(KCN)_x(NaCN)_{1-x}$ samples in order to study the effects of alkali ion disorder.

With respect to the theory of the pure alkali cyanides, progress has been made on several fronts. A detailed study of the local properties of alkali cyanides, including Debye-Waller factors, orientational probabilities and reorientations has been completed, and gives good agreement with experiment in KCN. The effects of molecular symmetry on the interactions between translational and rotational motions

BEST COPY AVAILABLE

been completed, and gives good agreement with experiment in KCN. The effects of molecular symmetry on the interactions between translational and rotational motions has also been explored, and used to show the importance of this property for the types of behavior observed in the various alkali cyanides. At the present time, we are beginning a study of the predicted neutron scattering cross-sections of high concentration mixed crystals, when the usual expansions in terms of (small) displacements no longer works, and are also extending the current models to the optic mode damping.

INTERACTION OF VIBRATING H ATOMS ON THE SURFACE OF PLATINUM PARTICLES BY ISOTOPE DILUTION NEUTRON SPECTROSCOPY

J. J. Rush and J. M. Rowe

and

R. R. Cavanaugh and R. D. Kelly
(Center for Chemical Physics)

Recent developments in electron energy loss-spectroscopy and rare gas atom scattering have yielded important information on the dispersion of surface modes on metals or alkali halides and thus on the details of surface forces and interactions. There are considerable difficulties, however, in extending such studies to the dynamics of chemisorbed hydrogen or molecular species. We describe here the first results of a study of the vibrational spectrum of hydrogen chemisorbed on the surface of platinum particles by isotope dilution neutron spectroscopy. These results demonstrate that such neutron measurements are a sensitive probe of the vibrational density of states which reflect the degree of phonon dispersion, and thus directly relate to the dynamic interactions between hydrogen or hydrogeneous species on a catalyst surface.

Neutron spectra were measured at 80° K on the BT-4 beryllium-filter spectrometer, with an energy resolutin of betweeen 5 and 7 meV over the energy range scanned. The spectra of chemisorbed H at various H/D ratios were obtained by appropriate subtraction of "blank" (highly deuterated) sample spectra from the results for various H concentrations.

The neutron spectrum between 34 and 100 meV for H at saturation coverage is shown in figure 1. Spectra were taken over a much wider energy range (30 - 250 meV) for a variety of surface conditions, which will be reported later. The full coverage H spectrum shows a broad (~30 meV FWHM) band peaked at 66 meV with a shoulder at ~77 meV. Our own work, as well as other neutron studies indicate that this band is associated with a second vibration peak at ~160 meV, and that both modes are due to H

BEST COPY AVAILABLE

bound on 2 or 3 fold coordinated sites. While such "density of states" spectra can provide critical information on surface bonding, their interpretation is often not straightforward, particularly in view of the complex surface of a catalyst. One could for, e.g., explain such a broad band as due to (1) impurities, (2) closely related species on the surface, (3) anharmonicity of the metal-hydrogen forces or (4) significant dispersion of the hydrogen vibration modes reflecting strong H-H dynamic coupling.

Our recent neutron scattering measurement of the dynamics of hydrogen mass defects in palladium deuteride suggested to us that similar measurements could be valuable in probing the dynamics of hydrogenous species on surfaces. The idea is simple: namely that the substitution of chemically identical light (or heavy) mass defects, such as H for D, on a surface overlayer leaves the surface electronically and chemically unchanged, but can greatly change the dynamical coupling between oscillators or rotators on the surface. The predictions of the theory of the dynamics of isolated mass defects are given by:

$$\int \frac{g(\omega)d\omega}{\omega_\ell^2 - \omega^2} = \frac{1}{\varepsilon\omega_\ell^2} \qquad (1)$$

where $g(\omega)$ is the density of states of the host crystal or surface overlayer, $\int g(\omega)d\omega = 1$, $\varepsilon = M_h - M_\ell / M_h M_{\ell(h)}$ is the mass of the defect (host) atom, and ω_ℓ is the defect local mode frequency. This expression shows that for a large mass ratio the position of the defect mode is related to the width of the host density of states and thus to the coupling between oscillators.

In figure 1 we show the neutron spectrum measured for 10% H distributed in a deuterated monolayer on platinum black. A comparison with the spectrum for the saturated H monolayer shows a significant shift (from 66 to 73 meV) and narrowing of the peak, and an apparent disappearance of the higher energy shoulder present in the 100% H results. This result suggests that the dominant effect creating the complex density of states of the H monolayer is dispersion of the surface optical vibrations, produced by strong H-H interactions, similar to those found in f.c.c. metal hydrides. Other phenomena which could broaden the vibrational spectrum, such as strong anharmonicity or the influence of defects or mixed site occupancy, should not produce any large change in spectral bands as the H/D ratio is varied.

BEST COPY AVAILABLE

To further test these conclusions we have compared our results to the predictions of eq (1), which has been shown t work well for H vibrations in bulk $PdD_{0.60}H_{.02}$. Due to the low neutron scattering cross section of D, we have not been able to measure the D vibrational spectrum of D absorbed on the surface. However, if we assume harmonic forces, we can derive this density of states by scaling the energy spectrum in figure 1 for the 100% H overlaywer by $1/\sqrt{2}$. Using this scaled spectrum, eq (1) predicts a local oscillator energy for an H defect of

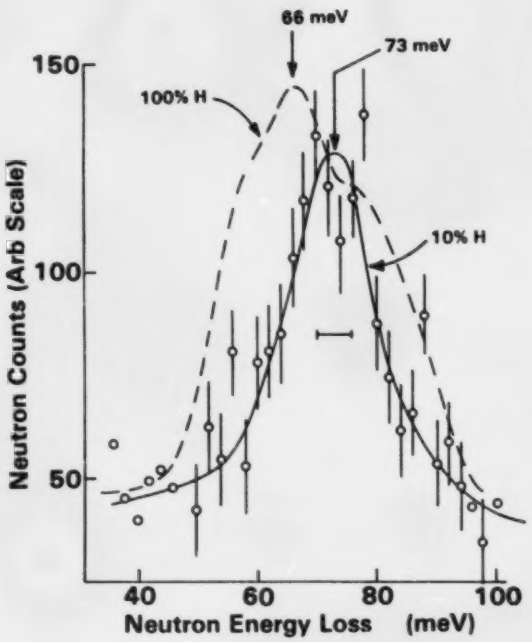

Figure 1. Neutron energy loss spectra between 34 and 100 meV at 80° K for a saturation coverage of H isotopes on cleaned Pt block. Results for 100% H are shown by the dashed lines. The energy resolution (FWHM) is indicated by the horizontal bar.

72.8 meV, in excellent agreement with the peak observed at 73 meV $\pm$ 1 for 10% H in figure 1. The observed peak is broadened beyond instrumental resolution due to the fact that defects at this concentration are far from isolated. This comparison demonstates clearly that the complex spectrum for the H overlayer is primarily due to dispersion of a vibration mode associated with a single type site on the Pt surface, which in turn reflects strong interaction of H atoms. In fact the observed spectral width suggests a H-H interaction of about 20% of the Pt-H force constant.

BEST COPY AVAILABLE

The present results show that neutron isotope-dilution spectroscopy can be a powerful probe of the origin of complex vibration bands for chemisorbed hydrogenous species and can provide direct information of the dynamical non-bonded (as opposed to chemical) interactions of such species. The method could be extended to low frequency oscillations or rotations of molecular groups (e.g. NH_2, NH_3, CH_3) on catalytic surfaces to provide insights on the intermolecular potentials experienced on catalysts, which are currently difficult or impossible to probe by other spectroscopies.

INCOHERENT INELASTIC NEUTRON SCATTERING STUDY OF THE INTERACTION OF ADSORBED HYDROGEN WITH OXYGEN ON PLATINUM BLACK

T. J. Udovic and J.J. Rush

and

R. R. Cavanagh and R. D. Kelley
(Center for Chemical Physics)

Interest in the surface chemistry of hydrogen on platinum stems from the involvement of hydrogen in the many important catalytic reactions that occur over this metal as well as its use as a titrant of platinum-catalyst surface area. In particular, various investigators have studied the adsorption of hydrogen on platinum and its interaction with oxygen; such information is beneficial for elucidating, for example, the mechanism of hydrogen oxidation. These studies have been concerned with determining hydrogen adsorption site geometry and hydrogen-oxygen surface reactivity. Vibrational spectroscopies such as high-resolution electron energy loss spectroscopy (EELS)[1,2], incoherent inelastic neutron scattering (IINS)[3,4], and infrared spectroscopy[5] have proved to be useful techniques for investigating this adsorption system.

In the present work, IINS has been utilized to probe the nature of adsorbed hydrogen and its interaction with oxygen on platinum black (i.e., high-surface-area platinum particles / 20 m^2g^{-1}). Figures 1 and 2 summarize the experimental results. The IINS spectrum for platinum black at 80 K, after hydrogen reduction at 383 K followed by vacuum evacuation at 473 K, is illustrated in figure 1a. Scattering intensity at 52, 104, 152, and 208 meV indicates the presence of "residual" hydrogen species (ca. 0.4 monolayers) believed to be associated with surface defect sites. The effect of adding a monolayer of oxygen to this surface at 80 K is illustrated by the difference spectrum in figure 1b. The vibrational modes associated with the "residual" hydrogen species have been replaced by a scattering feature at 128 meV indicative of the bending mode of adsorbed hydroxyl (-OH) species[2]. Figure 2a

BEST COPY AVAILABLE

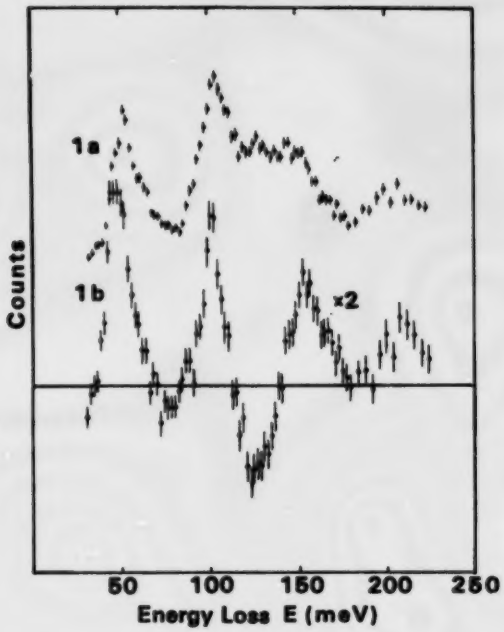

Figure 1. a) IINS spectrum for platinum black at 80K after hydrogen reduction at 383K followed by vacuum evacuation at 473K, b) difference spectrum after addition of a monolayer of oxygen at 80K (positive scattering intensity represents species removed by oxygen addition).

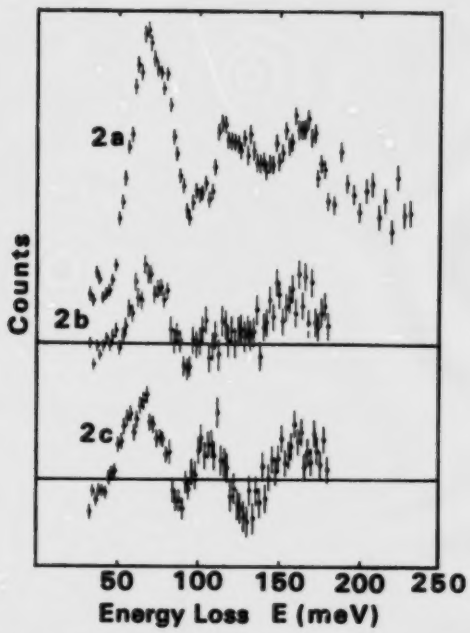

Figure 2. a) INNS spectrum for a monolayer of "adsorbed" hydrogen on platinum black at 80K, b) difference spectrum after addition of ca. 1/3 monolayers of oxygen, c) incremental difference spectrum after further addition of ca. 2/3 monolayers of oxygen (positive scattering intensities in difference spectra represent species removed by oxygen addition).

BEST COPY AVAILABLE

illustrates the IINS spectrum for a monolayer of "adsorbed" hydrogen on platinum black at 80 K with scattering intensity evident at 68, 115, and 166 meV. Figure 2b is the difference spectrum following addition of ca. 1/3 monolayers of oxygen (i.e., O/H ≈ 1/3) at 80 K. The vibrational features at 68 and 166 meV diminish in the same ratio, unlike the feature at 115 meV. This is suggestive of the existence of at least two types of hydrogen adsorption sites, one associated with features at 68 and 166 meV (more susceptible to oxygen attack) and one associated with the feature at 115 meV (less susceptible to oxygen attack). Figure 2c is the incremental difference spectrum following the further addition of ca. 2/3 monolayers of oxygen (i.e., total O/H ≈ 1) at 80 K. Now, the feature at 115 meV diminishes along with further loss in intensity at 68 and 166 meV. Concomitant with this loss is the appearance of the scattering feature at 128 meV, again indicative of the appearance of adsorbed hydroxyl species.

Force constant calculations and further experimental work are currently underway to establish the hydrogen adsorption site geometries on platinum black. It seems clear, however, that these sites are quite different than those established previously for hydrogen adsorbed on small particles of nickel[6] (which also has an FCC structure). This is suggestive of a strong correlation between adsorption site geometry and morphological behavior of the metal catalyst particles.

1. A.M. Baro, H. Ibach, and H.D. Bruchmann, Surface Sci. 88, 384 (1979).
2. G.B. Fisher and B.A. Sexton, Phys. Rev. Lett. 44, 683 (1980).
3. J. Howard, T.C. Waddington, and C.J. Wright, in Neutron Inelastic Scattering, Vol II, IAEA, Vienna, 499 (1978).
4. A Renouprez, P. Fouilloux, and B. Moraweck, in Growth and Properties of Metal Clusters (J. Bourdon, ed.) Elsevier, Amsterdam/New York, 421 (1980).
5. L.T. Dixon, R. Barth, and J.W. Gryder, J. Catal. 37, 368 (1975).
6. R.R. Cavanagh, R.D. Kelley, and J.J. Rush, J. Chem. Phys. 77, 1540 (1982).

BEST COPY AVAILABLE

NEUTRON SCATTERING STUDIES OF ZEOLITE RHO

M. J. Wax and R. R. Cavanagh
(Center for Chemical Physics)

and

G. D. Stucky, L. Abrams and D. R. Corbin
(E. I. du Pont de Nemours and Co., Wilmington, DE)

and

J. J. Rush

Catalytic activity for hydrocarbon cracking catalysts has frequently been associated with the various proton binding sites in zeolites. Direct spectroscopic measurements of these sites can permit one to follow the local properties of such adsorbed species as the zeolites are brought into the temperature range where their activity and selectivity is greatest.

Recent diffraction work on zeolite-rho has demonstrated that significant changes occur in the unit cell of this material (a non-centrosymmetric to centrosymmetric transition) upon either dehydration or deammoniation. In the present experiments, quasielastic and inelastic neutron scattering have been used to probe the diffusive motion which occurs near the transition temperature and to monitor the vibrational density of states of the adsorbed protons.

The incoherent inelastic scattering spectrum for the zeolite is shown in figure 1. Data taken above and below the structural transition temperature is shown. In addition, peaks in the IINS spectrum predicted by a simple force field model of the low temperature species are indicated by the intensity band. Comparison of the data obtained at the two different temperatures is facilitated if one focuses on the low energy range of the spectrum. As the temperature is lowered, a distinct increase in intensity is observed below 50 meV, accompanied by the loss of structure at 27 meV. This increased scattering intensity at low energy transfer is best accounted for by the presence of a new large amplitude vibrational mode which is reversibly generated upon heating. These results suggest a rearrangement of the protons bound in the zeolite cages at high temperature, which could be correlated with changes in chemical reactivity.

These initial studies of the modes of chemically active sites in zeolite-rho are currently being extended to examine the nature of the ammonia exchanged form of this material. Initial experiments have already detected the thermally activated reorientation of the ammonia and have yielded some insight into the vibrational density of states of the bound ammonia. Work is underway to extend and refine the

BEST COPY AVAILABLE

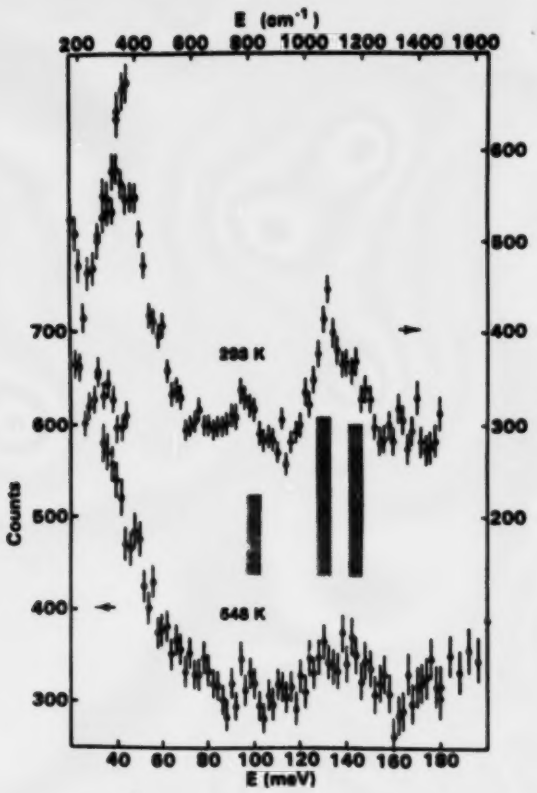

Figure 1. Neutron spectra measured for zeolite H-Rho at two temperature. The Break in the plotted intensities at 48 meV represents a change in monochromators.

study of these prototype catalytic materials. Cold neutron studies of the rotational dynamics of chemisorbed species in zeolites are also planned using the new time-of-flight spectrometer being developed at the NBS cold-source.

BEST COPY AVAILABLE

STUDY OF DYNAMICAL AND STATIC SCALING OF THE λ TRANSITION IN ^{4}HE

B. Mozer

and

B. Farnoux
(Laboratoire Leou Brillouin, CEN-Saclay, FRANCE)

and

B. LeNeindre
(Laboratoire des Interactions Moleculaires
et des Hautes Prersions, CNRS, Velletaueuse, FRANCE)

and

D. Brochier, F. Mezei, and S. Pujol
(Institut Laue-Langevin Grenoble, FRANCE)

In order to verify recent modifications to the theory underlying the critical behavior of He-4 at the λ transition, we attempted to measure the critical dynamics of second sound on IN112 just below the λ transition with as fine a temperature regulation (10^{-6}K) as used in light scattering experiments[1]. The sample cell was initially constructed at NBS and modified, finished, and carefully calibrated a I.L.L.. For the measurement, the sample cell was filled with He-4 so as to be at a pressure of 25 atmospheres at the λ transition. The temperature of the bath was held to 1.4 K and regulated to 10^{-3} Kelvin using the I.L.L. regulating system. The sample cell itself in a calibrated thermal leak configuration was regulated to 1-3 x 10^{-6} K using an AC resistance bridge and heater powered from the amplified error signal. Several germanium resistance thermometers calibrated at NBS were used in the regulation circuit as well as in various parts of the sample cell to obtain a temperature profile. The temperature remained stable over periods sufficiently long to collect neutron data of high-statistical accuracy

Inelastic neutron scattering data was first attempted for various values of wave vector difference, q, from the lowest value possible at IN11 of q = 0.25 A^{-1} and larger. Our best efforts with good statistics showed no difference in scattering above the background over reduced temperatures, $t = (T_\lambda - T)T_\lambda$, $10^{-6} < t < 10^{-1}$ for constant q or variable q for constant t. We then attempted to measure the static structure factor using IN11 as a diffractometer over the same temperature range and a wide range of q. Again we found no change in the intensity for small values of q at various t's. As a final test of our system, we measured the great increase in intensity at small q's as we allowed the He-4 system to traverse the critical gas-liquid phase transitions. The later measurement confirmed the temperature regulation, alignment, sensitivity, etc. of the system.

BEST COPY AVAILABLE

It is difficult to reconcile these null results with other known measurements around the λ transition. The bulk compressibility at our pressure and smallest t is known to increase 4 or 5 fold over the compressibility away from the transitions[2]. Therefore, we expect at q = 0 a 4 to 5 fold increase in intensity of the structure factor over the same temperature range. Assuming Ornstein-Zernicke or modified Ornstein-Zernicke behavior because of cross-over problems at q ≠ 0, we should have been able to see intensity changes in the structure factor both as a function of t at fixed q or as a function of q at fixed t. Furthermore, at our smallest reduced temperature, the intensity ratio of second sound to first sound in unity[1] which also should have allowed us to see the second sound signal. We suggest that a future measurement of the static structure factor at the transition at the smallest available q's must at least be made as to confirm the cross-over modifications to scaling theory.

---

1. G. Winterling, F. S. Holmes and T. J. Greytak, Phys. Rev. Lett., 30, 427 (1973).

2. H. Kierstad, Phys. Rev., 153, 258 (1967)

3. R. A. Ferrell, private communication.

SIMULATION OF A SLIGHTLY MORE COMPLEX CHEMICAL REACTION

D. H. Tsai
(Thermophysics Division)

and

S. F. Trevino
(U.S. Army Armament R and D Center, Dover, NJ)
and
(National Bureau of Standards, Gaithersburg, MD)

In a continuing work on the simulation of chemistry in the condensed phase of matter, we have extended the model to the reaction

$$AB \rightleftharpoons A + B - \text{energy} \qquad (1)$$

$$A + A \rightarrow A_2 + \text{energy} \qquad (2)$$

$$B + B \rightarrow B_2 + \text{energy} \qquad (3)$$

in an attempt to simulate a slightly more complex chemical system. The initial reaction is endothermic and the subsequent reactions (2) and (3) are exothermic. The properties of the system have been investigated and the response to heat pulse and shock loading is in progress .

BEST COPY AVAILABLE

NEUTRON SCATTERING STUDIES OF DILUTED MAGNETIC SEMICONDUCTOR SYSTEMS $Cd_{1-x}Mn_xTe$ and $Zn_{1-x}Mn_xSe$

T. M. Giebultowicz
(Purdue University, W. Lafayette, Indiana)
and
(National Bureau of Standards, Gaithersburg, MD)
and
J. J. Rhyne
and
W. Y. Ching
(University of Missouri, Kansas City, MO)
and
D. L. Huber
(University of Wisconsin, Madison, WI)
and
J. K. Furdyna
(Purdue University, W. Lafayette, IN)

1. Experiments and model studies on $Cd_{1-x}Mn_xTe$.

Studies of low-temperature spin dynamics in $Cd_{0.35}Mn_{0.65}$ Te have been enhanced significantly because of the recent increase of the reactor power to 20 MW. New studies of the inelastic magnetic scattering at T=4.2 K have been carried out for points in Q-space lying far away from the center of the diffuse magnetic peak (1,1/2,0), in which region the previously existing data[1] were of poor quality and could not be used for analyzing the spectrum features in detail. The results obtained presently appear to be in excellent agreement with the lineshapes predicted theoretically on the basis of a computer simulation model[2] of the zero-temperature spin dynamics in cubic dilute magnetic semiconductor (DMS) systems (fig. 1). A comparison of the measured and calculated dynamic structure factors $S(Q,\omega)$ yields the value of exchange constant for the nearest neighbors $J_{NN} = 13\pm1$ K.

Similar computer methods as in spin dynamics calculations have been applied for modeling the static spin correlations in $Cd_{1-x}Mn_xTe$. Results of such simulations predict that the short-range Type III antiferromagnetic order in this system is of anisotropic character, and should be described in terms of two different inverse correlation ranges which correspond to antiferromagnetic coupling of spins within (100)-type planes ($\kappa_\perp$), and to couplings between the planes ($\kappa_{||}$), respectively. As we have reported previously[1], diffraction experiments on $Cd_{0.35}Mn_{0.65}Te$ provided a qualitative support for these findings. Further model studies have revealed that the ratio $\kappa_\perp/\kappa_{||}$ is strongly dependent on the ratio J_{NNN}/J_{NN} between the exchange

BEST COPY AVAILABLE

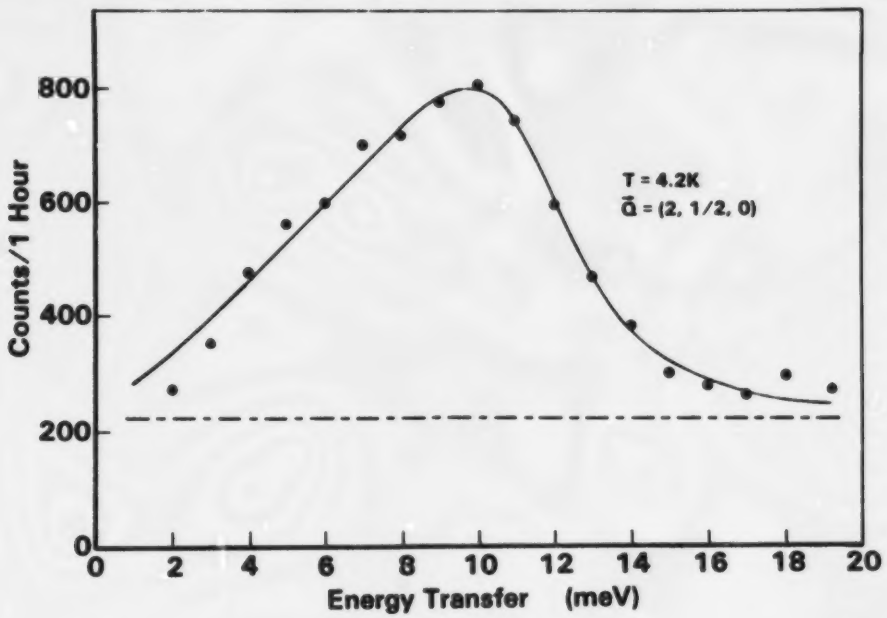

Figure 1. The spectrum of inelastic neutron scattering in $Dc_{0.35}Mn_{0.65}Te$ at 4.2 for $\vec{Q} = (2\pi/a)(2,1/2,0)$. The solid curve is the best fit of the theoretical spectrum (corrected for instrumental resolution), corresponding to J_{NN} = 12.8K. The dashed line is the background.

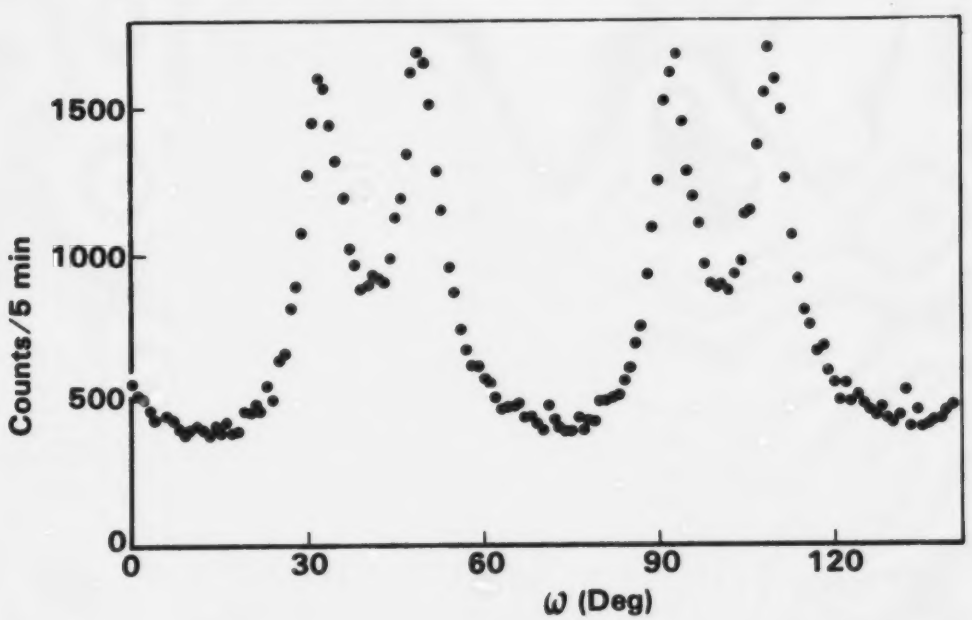

Figure 2. Extended ω-scan in $Zn_{0.45}Mn_{0.55}Se$ showing several diffuse magnetic peaks at symmetry equivalent positions.

BEST COPY AVAILABLE

constants for the next-nearest and the nearest neighbors. In order to obtain accurate experimental values of $\kappa_\perp/\kappa_\parallel$ to be compared with the theory, we carried out measurements of the (1,1/2 0) peak profiles for various scanning directions in Q-space, with particular attention to the role of instrumental effects. By comparing the measured and calculated data we find that the ratio J_{NNN}/J_{NN} in $Cd_{1-x}Mn_xTe$ is 0.12.

The mechanism of the Mn-Mn exchange interactions in DMS, and methods of measuring these interactions have recently attracted a great deal of interest[3-6]. Our studies demonstrate that neutron scattering methods offer an opportunity of determining the exchange constants for systems with high Mn concentrations, which is a region not accessible by most of the other experimental techniques[5,6]. Of particular interest is the determination of the ratio J_{NNN}/J_{NN}. The value we have found for $Cd_{0.35}Mn_{0.65}Te$ is the first direct measurement of this quantity in a DMS.

2. Spin ordering phenomena in $Zn_{0.45}Mn_{0.55}Se$

This compound is the first wurtzite-structured DMS system investigated by neutron scattering. Diffraction measurements carried out at low temperatures (4.2 K≤T≤45 K) revealed diffuse magnetic peaks (Fig. 2), the positions of which indicate an antiferrimagnetic order of the same type that occurs in the wurtzite structured modification of β-MnS[7]. The width of the peaks shows, however, that the range of such spin correlations in $Zn_{0.45}Mn_{0.55}Se$ is only ≈10Å, which is a considerably lower value than in case of cubic DMS systems with the same Mn concentration. A closer investigation of the peak lineshapes reveals that the elastic structure factor S(Q) in the basal plane can be described with a good approximation by an anisotropic Lorentzian function of the form $1/(1 + q_x^2/\kappa_x + q_y^2/\kappa_y^2)$, with $\kappa_x/\kappa_y \approx 2.1$ (however, the physical mechanism of this anisotropy is not yet as clear to us as in case of cubic DMS systems.). Studies of temperature dependences of κ_x, κ_y, and the scattering intensity show no noticeable features in the measured curves at T = 24 K, at which temperature the spin glass transition occurs in $Zn_{0.45}Mn_{0.55}Te$, as indicated by a pronounced cusp in the magnetic susceptibility vs. T (Ref. 8).

---

1. T. M. Giebultowicz and J. J. Rhyne, NBS Technical Note 1207, 66 (1985); also, T. M. Giebultowicz, J. J. Rhyne, W. Y. Ching, and D. L. Huber, J. Appl. Phys. 57, 3415 (1985).

2. W. Y. Ching, D. L. Huber, and K. M. Leung, Phys. Rev. B22, 3816 (1985); W. Y. Ching and D. L. Huber, Phys. Rev. B25, 5761 (1982), and B26, 6164 (1982).

3. B. E. Larson, K. C. Haas, H. Ehrenreich, and A. E. carlsson, to be published in the Proceedings of the International Conference on Magnetism, San Francisco 1985.

BEST COPY AVAILABLE

4. A. Lewicki, J. Spalek, J. K. Furdyna, and R. R. Galazka, ibidem.
5. Y. Shapira, S. Foner, D. H. Ridgley, K. Dwight, and A. Wold, Phys. Rev. B36, 4021 (1984).
6. R. W. Aggarwal, S. N. Jasperson, and R. R. Galazka, to be published.
7. L. M. Corliss, N. Elliot, and J. Hastings, Phys. Rev. 104, 924 (1956).
8. P. H. Keesom, private communication.

LONG-RANGE INCOMMENSURATE SPIN STATE IN DILUTE YGd ALLOYS

J.A. Gotaas
(University of Maryland, College Park MD)
and
(National Bureau of Standards, Gaithersburg, MD)
and
J.J. Rhyne
and
L.E. Wenger
(Wayne State University, Detroit, MI)
and
J.A. Mydosh
(University of Leiden, The Netherlands)
and
(University of California, Santa Barbara, CA)

Recent susceptibility and specific heat measurements on the Y-Gd alloy system have indicated that the boundary concentration between helical spin ordering and a spin glass state is lower than previously believed [1], with the spin glass occurring only for Gd concentrations below 2% [2]. In the light of this indirect evidence, we have carried out neutron diffraction measurements on Y(2.2%Gd) to directly determine the magnetic state.

Measurements were made on BT-6 with a variety of collimations in both the double-axis diffraction configuration and in the triple-axis mode with energy analysis to select out only the elastic scattering, using incident neutrons of 1.709A wavelength. A single crystal of nominal concentration Y(2.2%Gd), with the natural istopic abundant Gd, was shaped into a thin (1 mm) disk to reduce absorption.

Diffraction patterns display magnetic satellite peaks about the allowed (00ℓ) reciprocal lattice positions, including the origin, separated by 0.28c* from the nuclear peaks. Thus the magnetic moments order in a modulated state with a wavelength of ~20A and a propagation vector along the c axis [3], with moments in the basal plane. The diffraction peaks in the ordered state are resolution limited, indicating that the scattering originates from a long-range ordered state. No change

BEST COPY AVAILABLE

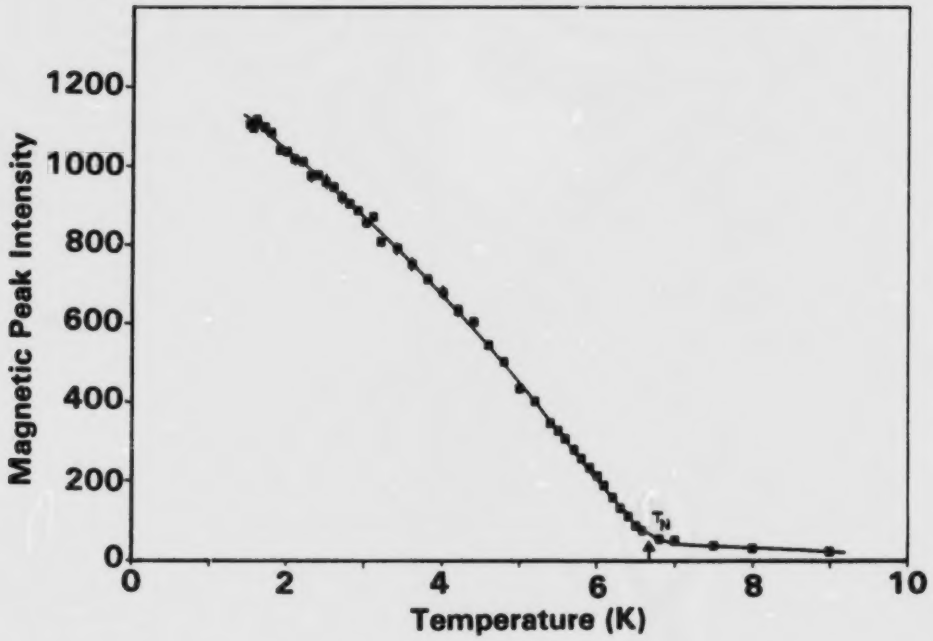

Figure 1. Magnetic intensity at the ordering wave vector of the oscillatory structure as a function of temperature.

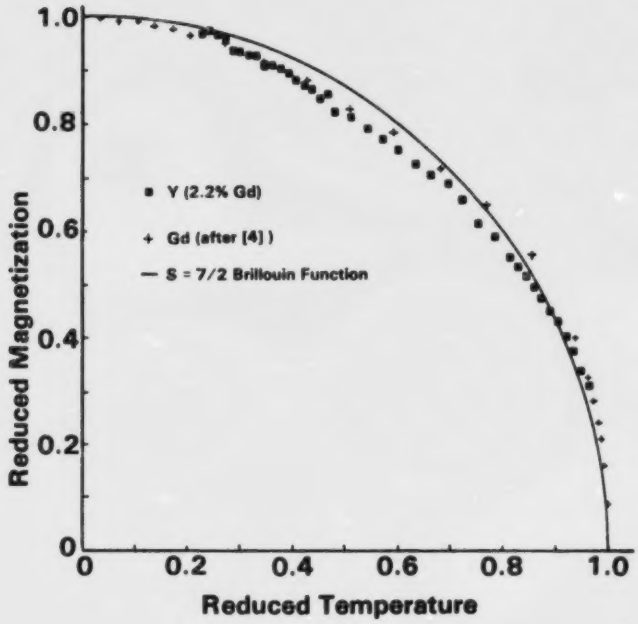

Figure 2. Reduced magnetization versus reduced temperature for Y(2.2%Gd) [■], Gd metal [+] and the Brillouin function for S=7/2 [line].

BEST COPY AVAILABLE

in the position or width of the satellite peaks is seen from the transition temperature (6.64 K) down to 1.5 K.

The temperature dependence of the magnetic peak intensity at q=0.28c*, which is proportional to m^2, is shown in figure 1, where the arrow indicates the estimated T_N. Intensity is present above the transition temperature, which would normally be interpreted as critical scattering. However this magnetic scattering persists at least to 25K (~$4T_N$), with a monotonic decrease with temperature. The incommensurate peak is broadened above T_N, indicating shortened correlation lengths, which however remain approximately 330±35A at 8 K and 315±35A at 12 K.

Figure 2 presents the square root of the magnetic intensity (proportional to the magnetization) versus temperature. For comparison, we include the magnetization of Gd metal [4] and the Brillouin function for S= 7/2 (which should be appropriate for a Gd moment), with the data plotted in reduced variables by normalizing the magnetization to the saturation value and the temperature to the transition temperature. Since our data only extend down to 1.5K ($0.226T_N$), we have normalized the moment scale to that of Gd at the equivalent reduced temperature. The similarity between the curves is apparent and indicates no unusual properties of the Gd moment in the ordered state.

The magnetic scattering can be placed on an absolute basis by comparing to the known nuclear scattering cross sections. The expression for the magnetic form factor depends in detail on the magnetic structure assumed for the system. The incommensurate satellites indicate that the magnetic moments order in a modulated state, but the intensities will be determined by the exact nature of the phase. Rare earths and their alloys commonly order in the basal plane spiral, with the moments in a given basal plane aligned ferromagnetically, but each plane rotated with respect to neighboring planes. The interlayer turn angle derived from the displacement of the incommensurate peaks is 50.4°. Assuming this structure, we derive a value for the Gd moment at 1.5K of $6.26\pm0.90\mu_B$ after correcting the data for extinction effects (~35%) on the intensity. Any deviation from the nominal concentration would lead to a shift in the calculated value of the magnetic moment.

---

1. B.V.B. Sarkissian and B.R. Coles, Commun. Phys. 1, 17 (1976). J.B. Sousa, J.M. Moreira. M.E. Braga, S.B. Palmer, S. Bates and B.J. Beaudry, J. Phys. F15 1171 (1985).

2. L.E. Wenger and J.A. Mydosh, J. Appl. Phys. 55 1850 (1984). P. Pureur, A. Fert, R. Wendler and K. Baberschke, J. Appl. Phys. 57 3230 (1985).

3. W.C. Koehler, Ch. 3 in Magnetic Properties of Rare Earth Metals, ed. R.J. Elliott (Plenum Press, London, 1972). W.C. Koehler, J. Appl. Phys. 32 20S (1961).

BEST COPY AVAILABLE

FIELD DEPENDENCE OF THE TWO-SPIN CORRELATION FUNCTION IN A REENTRANT SPIN GLASS

R. W. Erwin and J. W. Lynn
(University of Maryland, College Park, MD)
and
(National Bureau of Standards, Gaithersburg, MD)

Previous investigations of the reentrant spin-glass state[1] have been continued by studying the magnetic field dependence of the two-spin spatial correlations in the metallic-glass $(Fe_{0.25}Ni_{0.75})_{75}P_{16}B_6Al_3$ using small angle neutron scattering (SANS) techniques. In this magnetically isotropic system the application of a uniform magnetic field allows a determination of the correlation functions for spin components both parallel and transverse to the applied field direction. The scattering function can then be separated as,

$$S(q,\theta) = (1 - \cos^2\theta)S^{zz}(q) + (1 + \cos^2\theta)S^{xx}(q) \quad , \qquad (1)$$

where q is the magnitude of the wave vector transfer and θ is the angle between q and the field direction. S^{zz} and S^{xx} are defined as configurational (domain) averages.

The present alloy exhibits a conventional second-order ferromagnetic phase transition when cooled below T_c = 198 K. At lower temperatures spin-glass behavior is observed, which includes a strong decrease of the low-field d.c. magnetization.[2] The signature of the low temperature spin-glass state in the zero-field neutron scattering is the appearance of a component with a Lorentzian-squared wave vector dependence. Thus the scattering function[3] can be written in the form,

$$S(q) = \frac{(kT)A}{\kappa^2 + q^2} + \frac{\kappa B}{(\kappa^2 + q^2)^2} + C\delta(q) \quad . \qquad (2)$$

The first term is the product of the thermal population factor and the usual Lorentzian wave-vector-dependent susceptibility arising from the spin-wave fluctuations. Associating the last two terms with the static magnetic configuration of the spin system leads by a sum rule to the conclusion that $B \propto q_{EA} - m^2$ and $C \propto m^2$, where q_{EA} is the Edwards-Anderson order parameter $\langle\langle S_i \rangle^2\rangle$ and m^2 is the square of the site-averaged magnetization. Note that the last term (C) is

EST COPY AVAILABLE

unobservable for the present neutron scattering measurements and that B is an order parameter for the spin glass.

The angular dependence of the SANS data in an applied field was fit to the functional form in eq (1), to extract the separate correlation functions S^{zz} and S^{xx}. These functions could then be analyzed via eq (2) to obtain the parameters (A^x,B^x,κ^x) and (A^z,B^z,κ^z). These fits have been performed over a wave vector range $(0.012\ A^{-1} \leq q \leq 0.40\ A^{-1})$ which ensures that inelasticity corrections are negligible, although resolution corrections are important. Care has also been taken to align the sample ribbons with the magnetic field direction in order to minimize demagnetizing fields. The results are shown in figure 1 for three temperatures: just below T_c, 0.75 T_c and 0.05 T_c. Although these data are preliminary, there are several significant trends to be noted. First, for some temperature range below T_c the data are described simply by a Lorentzian q-dependence ($B^x = B^z = 0$), while at lower temperatures curvature of the Ornstein-Zernike plots produces fits with non-zero values of the parameters B^μ. The temperature and field dependences of B^μ are then in qualitative accord with the same dependences measured by bulk magnetization[2] with the assumption that $B^\mu \propto q_{EA} - m^2$. Also observe that the Lorentzian amplitude A^x is independent of applied fields up to 0.2 Tesla over the entire temperature range measured. This fact lends support to the conjecture that the transverse Lorentzian term in the scattering function arises from dynamic spin-wave fluctuations. Further evidence for this argument is the fact that just below the Curie temperature $A^z = A^x$ (as $H \to 0$) as predicted for isotropic ferromagnets. Additionally, in the ferromagnetic temperature regime κ^x and κ^z have qualitatively the field dependences predicted by mean-field theory[4], where $A^x \propto q_{EA}/D$, $(\kappa_x)^2 \propto A^x/\chi^x(q=0,H)$ and $\kappa^z \geq \kappa^x$. Here D is the spin-wave stiffness and $\chi^x(q=0,H)$ is the bulk transverse susceptibility. These mean-field results also explain the temperature independence of A^x near T_c where q_{EA}/D is slowly varying, as well as the increase of A^x in the spin-glass temperature regime where the spin-wave stiffness is decreasing as q_{EA} is monotonically increasing. In contrast, at low temperature κ^z rises less rapidly with applied field than κ^x. This would be expected for static fluctuations where κ^z should decrease for sufficiently large applied fields as the spins are increasingly aligned. Of course, the observed increase of κ^z and κ^x may be due to the preferential alignment of the larger clusters of spins over the smaller clusters.

In conclusion, the anisotropy induced by an applied field for the magnetic scattering from an amorphous reentrant spin-glass alloy has been shown to yield self-

BEST COPY AVAILABLE

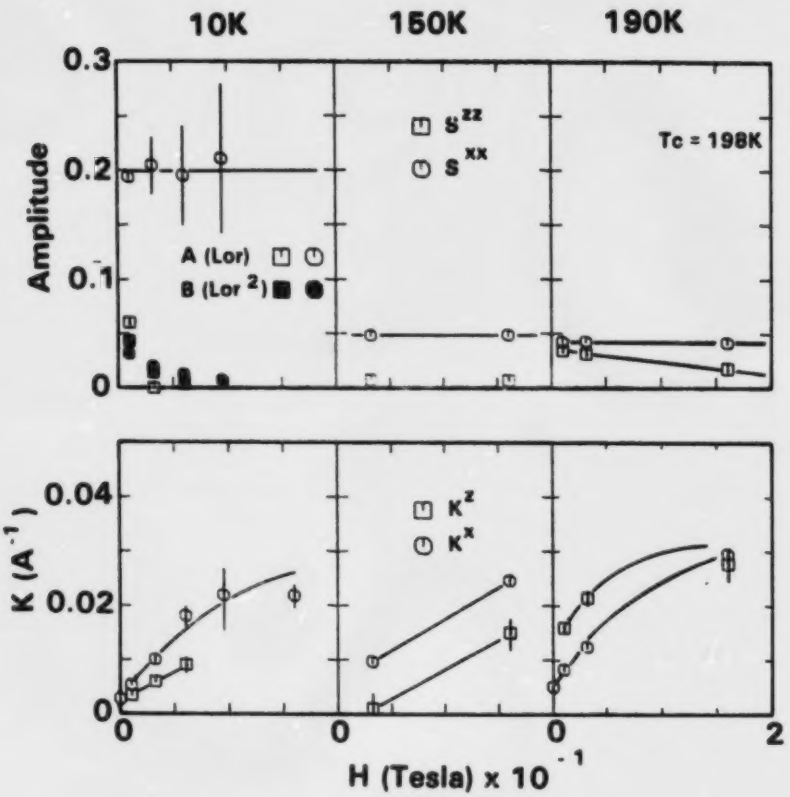

Figure 1. Parameters determined from the fits to the SANS data using the form of the scattering function in eqs (1) and (2) in the text.

consistent information about the static and dynamic parts of the two-spin correlation functions. A quantitative comparison with theory will require further measurements.

---

1. R. W. Erwin, J. W. Lynn, J. J. Rhyne and H. S. Chen, J. Appl. Phys. 57, 3473 (1985).

2. P. Mazumdar, S. M. Bhagat, M. A. Manheimer and H. S. Chen, J. Appl. Phys. 55, 1685 (1984).

3. From the doctoral dissertation by R. W. Erwin, University of Maryland 1985.

4. S. K. Ma, Modern Theory of Critical Phenomena, Benjamin/Cummings 1976, p. 87.

BEST COPY AVAILABLE

NEUTRON SCATTERING STUDY OF THE SPIN DYNAMICS OF AMORPHOUS $Fe_{70}Ni_{20}Zr_{10}$

J.A. Fernandez-Baca
(University of Maryland, College Park, MD)
and
(National Bureau of Standards, Gaithersburg, MD)
and

J.J. Rhyne

and

G.E. Fish
(Allied Corporation, Morristown, NJ)

The iron rich $(Fe_{90-x}Ni_x)Zr_{10}$ amorphous system exhibits Invar characteristics[1] where the thermal expansion and a large positive spontaneous volume magnetostriction nearly cancel below the Curie temperature. Furthermore, it is known that the magnetic properties of this system are very peculiar [1] : The Curie temperature decreases with decreasing Ni content, and below x≈18 the magnetic moment also decreases monotonically. In fact when x→0 the system does not order ferromagnetically , as has been found from neutron critical scattering measurements on $Fe_{91}Zr_9$ [2] . At this nominal concentration of Fe and Zr the system enters a spin-glass state at T ≈ 210K.

These anomalous properties [1-5] have been attributed to the existence of competing ferromagnetic and antiferromagnetic exchange interactions originating from the distribution of Fe-Fe nearest neighbor distances in the amorphous state. Thus for the high Fe concentrations ferromagnetic ordering is destroyed by increasing antiferromagnetic exchange couplings.

In order to obtain a better understanding of the magnetic properties of the iron rich (Fe-Ni)Zr alloys we have started a neutron scattering study of the spin dynamics of this system for various concentrations of Ni. Results of our measurewments on $Fe_{70}Ni_{20}Zr_{10}$ are reported here. The amorphous nature of the system required that measurements be taken near the forward (000) beam position. Fixed incident energies of 28.5 or 13.8 meV were used and a PG filter was placed after the monochromator to suppress higher order wavelength contaminations. Soller slit horizontal collimators of 15'-12'-11'-25' were used to produce a FWHM of 0.70 meV (for E_i=28.5 meV) or 0.35 meV (for E_i=13.8 meV) at the elastic position. Wave-vector transfers examined were in the range $0.07\ A^{-1} \leq q \leq 0.12\ A^{-1}$ and the temperature range was 250K ($0.55T_c$) to 403K ($0.89T_c$). Well defined spin waves were observed at all the temperatures studied. In analyzing the data, spin-wave energies and linewidth information were

BEST COPY AVAILABLE

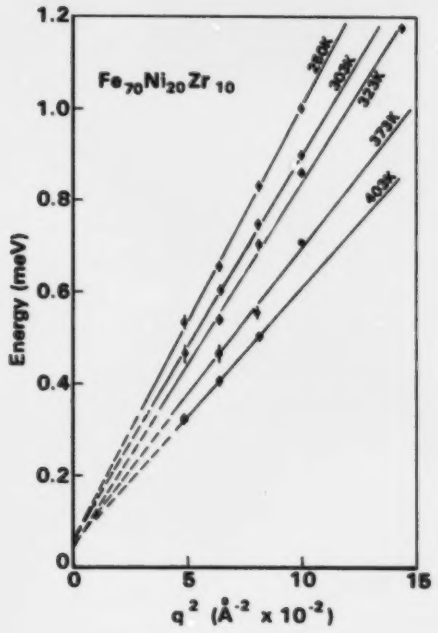

Figure 1. Temperature dependence of spin-wave excitiationat q = 0.10 A^{-1}. The solid lines are the least squares-fit to the convolution of a Lorentzian cross-section with the instrumental resolution. The spin-wave energy positions are indicated by arrows.

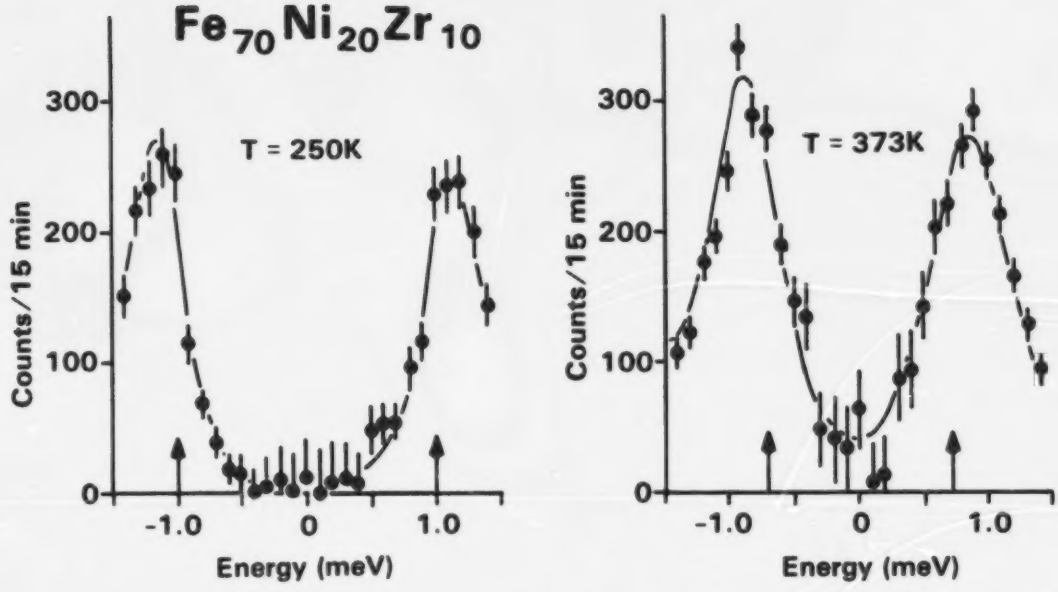

Figure 2. Quadratic spin-wave dispersion relations for the $Fe_{70}Ni_{20}Zr_{10}$ amorphous system at several temperatures.

BEST COPY AVAILABLE

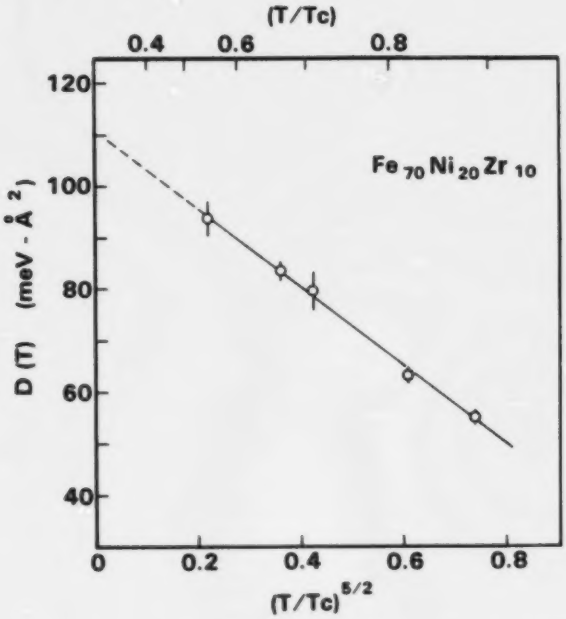

Figure 3. Stiffnes constant `D' plotted as a function of $(T/T_c)^{5/2}$ in the range of temperatures under study ($0.55T_c$-$0.89T_c$), showing the typical two-magnon Dyson form of renormalization.

obtained by convoluting a theoretical cross-section with the instrumental resolution and least-squares fitting to the observed spectra, after subtraction of the background scattering. The spectral weight function used in the convolution was a double Lorentzian. Figure 1 shows two sets of typical constant-q scans for q=0.10 A^{-1} at T=250 and 373 K. The background and parasitic elastic scattering principally from the cryostat or furnace have been subtracted. The solid lines are the result of the least squares fit , and the spin-wave positions for both neutron energy gain (E<0) and energy loss (E>0) are indicated by arrows. The actual spin wave energy is shifted lower than the peak energy by resolution effects. There is a gradual broadening of the peaks with increasing temperature, but the linewidths are relatively small compared to the instrumental energy resolution .

The spin-wave energies at all temperatures under study were found to obey the quadratic dispersion relation expected for a Heisenberg ferromagnet :

$$E = \Delta + D(T)q^2 + \ldots \quad (1)$$

(see figure 2) where Δ = 0.05 meV is an effective anisotropy gap which originates mainly from the dipole interaction, and shows no temperature dependence. 'D' exhibited a temperature dependence of the form :

$$D(T) = D(0)[1-a(T/T_c)^{5/2}] \quad (2)$$

(see figure 3) with D(0) = 110.9 ± 1.5 meV-A^2 and a=0.68 ± 0.01.

BEST COPY AVAILABLE

As seen in figures 2 and 3, the long-wavelength spin waves in amorphous $Fe_{70}Ni_{20}Zr_{10}$ show the behavior expected for a conventional Heisenberg ferromagnet over an unusually wide range of temperatures as found also in other amorphous ferromagnets. The stiffness constant D(0) is about 1.5 times the value calculated from the magnetization measurements by Krishnan et al.[5] . Such a discrepancy implies that additional excitations other than spin waves are present and lead to the anomalously rapid decrease of the bulk magnetization with increasing temperature. Similar behavior has also been reported for other Invar systems and is likely to be an intrinsic dynamic property of the Invar state.

1. K.Shirakawa, S.Ohnuma, M.Nose and T. Masumoto. IEEE Trans. Mag. 16,910 (1980).
2. J.J. Rhyne and G.E. Fish. J. Appl. Phys. 57,3407 (1985).
3. S. Ohnuma, K. Shirakawa, M. Nose and T. Masumoto . IEEE Trans. Mag. 16,1129 (1980).
4. H.Hiroyoshi and K.Fukamichi. J. Appl. Phys. 53,2226 (1982).
5. R. Krishnan , K.V. Rao and H. H. Liebermann, J. Appl. Phys. 55,1823 (1984).

MAGNETIC ORDER IN THE SUPERCONDUCTOR $Tm_2Fe_3Si_5$

J. W. Lynn, J. A. Gotaas
(University of Maryland, College Park, MD)
and
(National Bureau of Standards, Gaithersburg, MD)
and
R. N. Shelton
(Iowa State University, Ames, IA)

There is currently great interest in the behavior of superconductors which contain a sublattice of magnetic (rare earth) ions. In materials where the magnetic system prefers ferromagnetic alignment of the spins the superconductivity is quenched at low temperatures[1], or the magnetic ground state is modified from ferromagnetism to a long-wavelength sinumagnetic state where coexistence can occur.[2] In the case of antiferromagnetic order, on the other hand, coexistence with superconductivity is found to the lowest temperatures.[1] A singular exception to this rule appears to be the system $Tm_2Fe_3Si_5$. In the absence of applied pressure this material becomes antiferromagnetic at $T_N \sim 1.1$ K, with the absence of superconductivity.[3-5] With applied pressure, however, superconductivity appears above the magnetic ordering temperature, but then disappears again at T_N. The magnetic transition itself is insensitive to the pressure so that it appears that the superconductivity is quenched

BEST COPY AVAILABLE

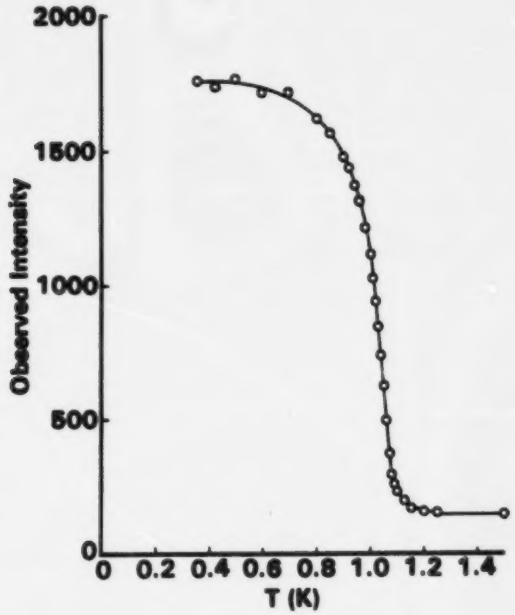

Figure 1. Observed magnetic intensity for the {100} antiferromagnetic Bragg peak as a function of temperature, with an applied pressure of 2.3 kbars. No hysteresis was observed between warming and cooling cycles.

by antiferromagnetic long range order. We have been carrying out neutron diffraction measurements as a function of temperature and pressure to investigate the influence of the superconductivity on the magnetic structure in this material.

The sample was loaded in an aluminum sample cell with an inner diameter of 3/32". Pressure could then be applied by forcing and clamping a piston at room temperature. The actual applied pressure achieved in the cell was determined by a measurement of the lattice parameter, and then comparing with the room temperature lattice parameter determined from measurements on the identical sample using a hydrostatic helium pressure system. The sample cell was then mounted in He^3 refrigerator to measure the magnetic scattering.

With no pressure applied the magnetic order is a relatively simple antiferromagnetic type, with the full 6.5 μ_B Tm^{3+} moment ordering.[5] The intensity of the {100} antiferromagnetic Bragg peak is shown in figure 1 for an applied pressure of approximately 2.3 kbars, which should be just above the critical pressure where superconductivity appears. The magnetic order parameter is still continuous and reversible, and shows no signs of the presence of superconductivity. Similar

BEST COPY AVAILABLE

behavior has been found in the coexistent antiferromagnetic superconductors.[1] We also found no evidence of any magnetic scattering at small angles, either near T_N or at low temperatures. Work is in progress to extend these measurements to higher pressures, where the superconductivity is well established before magnetic order sets in at lower temperatures.

---

1. W. Thomlinson, G. Shirane, J. W. Lynn and D. E. Moncton, Chap. 8 in Superconductivity in Ternary Compounds, ed. by M. B. Maple and O. Fischer, Springer-Verlag (New York, 1982).

2. J. W. Lynn, J. A. Gotaas, R. W. Erwin, R. A. Ferrell, J. K. Bhattacharjee, R. N. Shelton and P Klavins, Phys. Rev. Lett. 32, 133 (1984).

3. C. U. Segre and H. F. Braun, Phys. Lett. 85A, 372 (1981).

4. C. B. Vining and R. N. Shelton, Solid State Commun. 54, 53 (1985).

5. A. R. Moodenbaugh, D. E. Cox and C. B. Vining, Phys. Rev. B (to be published).

MAGNETIC AND SUPERCONDUCTING PROPERTIES OF HOLMIUM-RICH $(Er_{1-x}Ho_x)Rh_4B_4$

J. W. Lynn and J. A. Gotaas
(University of Maryland, College Park, MD)

and

(National Bureau of Standards, Gaithersburg, MD)

and

R. N. Shelton and H. E. Horng
(Iowa State University, Ames, IA)

and

C. J. Glinka

Neutron scattering, susceptibility and resistivity measurements have been carried out on $(Er_{1-x}Ho_x)Rh_4B_4$ for concentrations x = 1.0, 0.89, 0.84, 0.75, which span the "multicritical" point ($x_c \approx 0.9$) where the magnetic and superconducting phase boundaries meet. For all concentrations studied a transition to long-range ferromagnetic order is observed, with the Ho moments ordering along the tetragonal axis. The spins are in fact locked along the c-axis by strong crystal-field anisotropies, yielding Ising-like magnetic behavior in this concentation region. The temperature dependence of the order parameter is mean-field like, suggesting that the range of the magnetic interactions is large, and we attribute this behavior to the importance of dipolar interactions. In the concentration range $x < x_c$ where superconductivity is observed, the magnetic transition appears to be continuous and reversible, and occurs within the nominal superconducting interval $T_{c2}(x) < T <$

BEST COPY AVAILABLE

$T_{c1}(x)$. Thus there is some kind of "coexistence" of long range magnetic order and superconductivity in the samples, but the nature of this coexistence cannot be determined unambiguously. In particular the experimental evidence in this system is not sufficient to decide if there is true microscopic coexistence, or whether some portions of the sample are ferromagnetic and normal while other regions are superconducting and paramagnetic (or magnetically ordered with a very long wavelength sinusoidal periodicity). Below T_M strongly temperature-dependent small angle scattering is observed, characterized by a cross section of the Porod form $S(Q) = A(T)/Q^4$ where A(T) increases monotonically with decreasing temperature. This wave vector dependence is consistent with the assumption that the scattering originates from domain walls whose widths are large compared to the inverse Q range explored (~250 A). In particular, no oscillatory component to the magnetization was observed for any concentration or temperature within the experimentally accessible wave vector range of $Q > 0.003\ A^{-1}$, in contrast to the behavior of $ErRh_4B_4$. At the lowest concentration studied (75% Ho) the magnetization was found to be reduced in the temperature region where superconductivity appeared. The magnetic order parameter, however, was still found to be continuous and reversible.

ADVANCED NEUTRON METHODS

N. Berk, D. Fravel, C. Glinka, J. LaRock, J. M. Rowe, and T. Udovic

1. Small Angle Neutron Scattering (SANS)

During the six month shutdown for doubling the reactor power to 20MW, a number of improvements were made to the SANS instrument. Chief among these were the modifications made to the facility's 65 x 65 cm^2 position-sensitive detector. The detector's anode and two cathode wire grids were replaced with improved versions which have faster response times thus reducing detector dead time and thereby increasing its count rate capability (now estimated to be about 10 kHz). In addition, the detector was refilled with a new gas mixture of $^3He/CF_4$, which tests have shown to be far less sensitive to gamma rays than the $^3He/Xe$ mixture used previously. The overall detector background count rate (per MW) is now one-third of what it was prior to these modifications. This reduction in background, combined with the doubling in the reactor power has greatly increased the sensitivity of the instrument for measuring weak scattering signals.

Other improvements to the instrument include the installation of quick-connect flanges on the pre-sample flight path to facilitate changing beam collimation, added data storage capacity at the instrument's computer and the implementation of a high speed data link to a VAX computer to enable data to be transferred and reduced more

BEST COPY AVAILABLE

rapidly. The facility's sample environment equipment has been augmented by the purchase of a computer programmable temperature controller and power supply which will control and monitor the temperature of a variety of vacuum of furnaces as well as the instrument's multi-specimen sample changer. One such furnace has been adapted to mount between the pole pieces of an electromagnet for in-situ high temperature measurements of magnetic materials in an applied field of up to 10 kilogauss.

Since resuming operation at 20 MW reactor power, the SANS instrument has once again been heavily utilized by NBS, university and industrial scientists for structural experiments in polymers, metallurgy, ceramics, magnetism and biology. C. Han and coworkers in the Polymer Division have recently completed a detailed study of the miscibility limits of blends of polystyrene and polyvinyl methyl ether (PVME) as a function of temperature and PVME volume fraction. By making temperature jumps into the immiscible region of the phase diagram the first stages of phase separation have been observed and found to exhibit many of the features of spinodal decomposition. W. Wu and B. Bauer, also of the Polymer Division, along with collaborators from the University of Massachusetts have continued their work on the formaton of network structures in epoxys. Evidence for the formation of paracrystalline-like networks have been seen through the use of deuterium labeling of one component of the epoxy.

The relationship between precipitate size and morphology and the strength and hardness of structural alloys has been the focus of a number of recent SANS studies in metallurgy. The formation of iron-copper precipitates in reactor pressure-vessel steels due to fast neutron irradiation has been observed by G. R. Odette from the University of California at Santa Barbara. In his most recent experiments, Odette has followed the coarsening of these precipitates, which can lead to embrittlement of the steel, via in-situ annealling measurements in an applied magnetic field. The effects of various alloying elements on the high temperature strength of new types of single crystal superalloys used in advanced turbine engines is being studied in joint collaboration with researchers from General Electric. Initial experiments have probed the effects of small additions of rhenium on the morphology of the γ' precipitates which are the main strengthening mechanism in these alloys.

Use of the SANS facility for structural studies in biology has increased in the past year as a result of joint NBS - National Institutes of Health collaborations. In one of these, R. Nossal of NIH, along with S. H. Chen of MIT, have completed a study of concentrated solutions of the globular protein bovine serum albumin. In this study, interparticle interactions were clearly observed and could be effectively modeled by screened Coulomb forces to yield values for the protein surface charge and screening length under a variety of solvent conditions. In another important study, A. Wlodawer of NBS and coworkers at NIH, along with G. Zaccai of the Institut Laue

BEST COPY AVAILABLE

Langevin, have successfully measured some of the dimensional parameters of DNA-protein complexes known as gyrosomes.

Additional details of some of the work mentioned above, as well as other reports of SANS studies, appear elsewhere in this issue.

OLD NEUTRON RESEARCH FACILITY

I. Anderson and J. Gotaas

(University of Maryland, College Park, MD)
and
(National Bureau of Standards, Gaithersburg, MD)
and
C. G. Glinka, J. M. Rowe, J. J. Rush, T. Udovic and R. Williams

The conceptual design of the proposed new cold neutron guide hall was completed by the architect/engineer, and cost estimates were prepared. After full review of this concept, a contract for the final architect/engineer is now (July 1985) being negotiated that will lead to final design drawings suitable for the solicitation of a fixed price construction contract. The new building will be constructed adjacent to the north side of the existing reactor confinement building, and will provide approximately 30,000 square feet of additional space for cold neutron instrumentation. It is anticipated that construction of the new experimental hall will begin in 1986. The cold neutron beams will be brought into the new experimental hall by means of neutron guides, plated with either normal nickel or Ni-58, as appropriate for the proposed instruments on the particular guide. The detailed design of the neutron guides and reactor modifications is now under way.

Up to 1/3 of the 15 proposed experimental facilities are to be developed by Participating Research Teams, which will be responsible for the design, construction and maintenance of the facilities. A notice was published in The Commerce Business Daily (Issue No. PSA-8795, March 14, 1985) soliciting expressions of interest from prospective PRT's. Several replies have been received, and are being actively pursued, with the intent of negotiating final agreements in the near future. We will continue to solicit further PRT's as the facility development progresses.

The design of the first instruments to be constructed for the new cold neutron experimental hall is continuing. The two proposed Small Angle Neutron Scattering (SANS) are in the final stages of conceptual design, and detailed design will begin

BEST COPY AVAILABLE

in the coming year. The conceptual design for one Time Of Flight (TOF) instrument is continuing, and many of the ideas are being tested in the TOF spectrometer now being installed in the existing reactor hall. A new data acquisition system, based on the micro-VAX II 32 bit microcomputer is now in the final stages of completion, and will be installed on the existing SANS and TOF instruments in the next few months. It is anticipated that this system will become the standard for all new cold neutron instruments, assuming that operation of the test stations is satisfactory.

NBSR COLD NEUTRON SOURCE

R. S. Carter and P. A. Kopetka

The NBSR Cold Neutron Source is progressing well. The Safety Analysis Report[1] has been completed and reviewed by the Safety Evaluation Committee, and all necessary approvals have been obtained for final installation.

Figure 1 is a schematic illustration of the cold source. The moderator is a block of D_2O ice 14" in diameter and 13" thick with an 8" diameter, 6" deep reentrant hole. (The reentrant hole is not shown in figure 1.) The ice will be frozen in layers to avoid damage to the ice chamber. Other features include a helium filled jacket around all vacuum regions and tubes connected to the ice chamber. The vacuum pump itself is wholely enclosed within the helium containment gas. During operation, the region over the ice and all the lines into the ice chamber are backfilled with helium. These lines are all isolated within the helium containment and connected to the ballast tank. The ballast tank is sized so that the pressure of the cover gas over the ice which is normally about 19 psia at operating temperature (25°K) will not exceed 30 psia at room temperature. During operation, a deuterium getter is open to the helium cover gas to absorb deuterium that might be released if the cooling system failed and the ice temperature should start to rise. The mass of ice is such that even if the cooling should fail, almost an hour is required at full reactor power before the ice reaches its melting temperature. Thus, ample time is available to take appropriate action.

The cryostat is made of a magnesium alloy to minimize heating from capture γ-rays and is surrounded by a lead and bismuth shield to reduce heating by core -rays as shown in figure 2. The bismuth shielding is completed and the manufacture of the cryostat will be completed by July 1985. Installation in the reactor is expected shortly thereafter.

1. R. S. Carter, Safety Analysis Report on the D_2O Cold Neutron Source for the NBSR, NBSR 13 (1984).

BEST COPY AVAILABLE

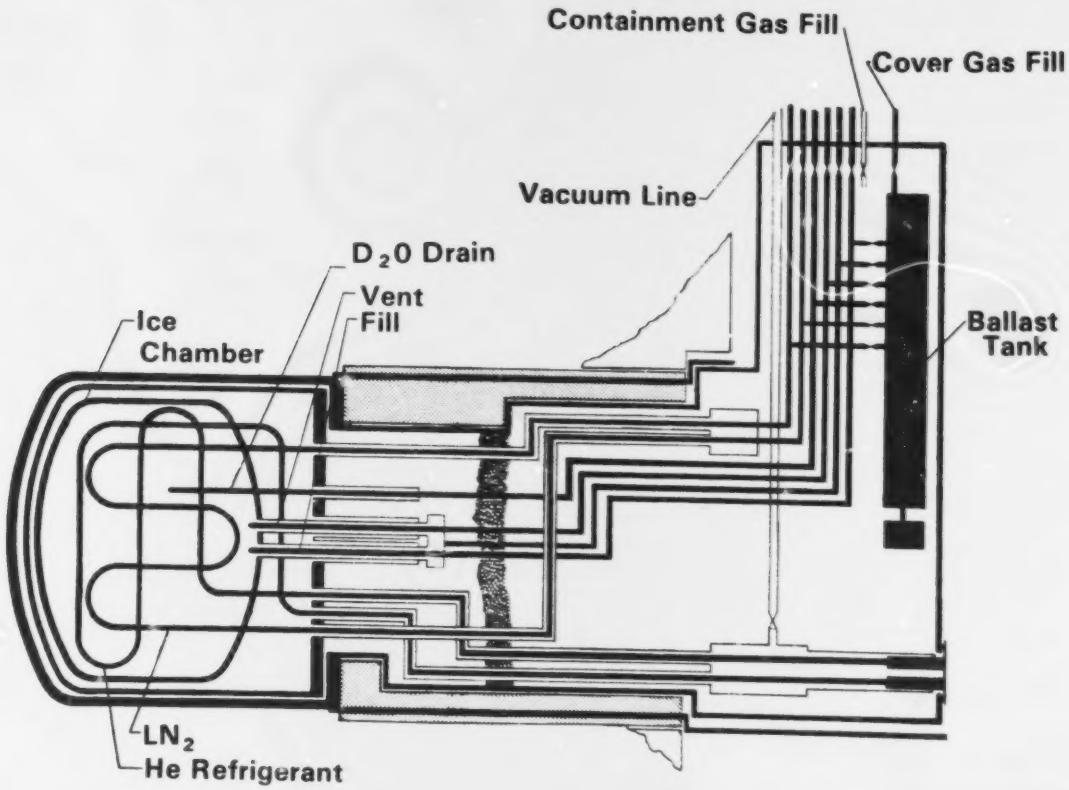

Figure 1. Schematic illustration of cold source facility.

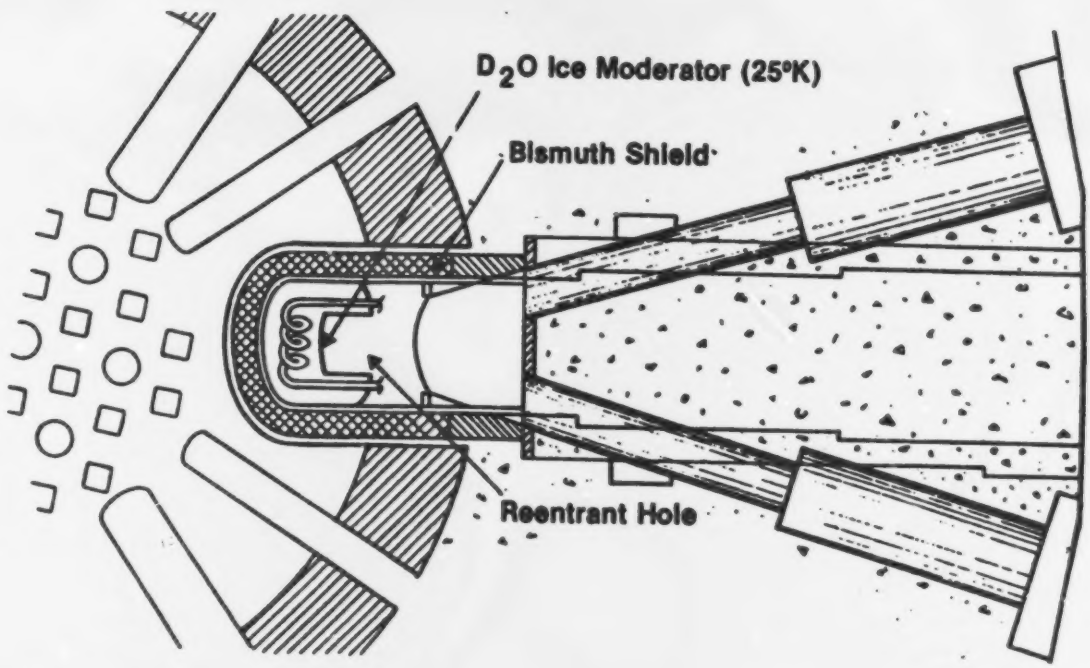

Figure 2. Cold neutron source.

BEST COPY AVAILABLE

THE NBS NEUTRON TIME-OF-FLIGHT SPECTROMETER

I. S. Anderson
(University of Maryland, College Park, MD)
and
(National Bureau of Standards, Gaithersburg, MD)
and
T. J. Udovic, J. M. Rowe, and J. LaRock

A schematic outline of the new high-resolution time-of-flight (TOF) spectrometer under construction at the NBS reactor is shown in figure 1. The beam from the CTW tube at the reactor is monochromated by means of two pyrolitic graphite crystals separated by a shielding drum containing a replaceable collimator. The rotation of the drum moves the crystals parallel to each other on two shafts which are also used to reorient each crystal about a vertical axis. The absolute position of the drum and rotation of each shaft are encoded by means of vector resolvers directly coupled to each movement. A second collimator mounted on an optical bench after the monochromator ensures that the energy resolution of the instrument is not limited by the effective mosaics of the graphite crystals. At present, three secondary collimator exist with 40', 20' and 10' collimation and the corresponding primary collimators are under construction. The wavelength may be continuously varied between 2.2 Å and 6 Å using this system; for wavelengths above 4 Å, a cooled Be filter is available to remove higher-order contamination.

A multiple-slit Fermi chopper is used to pulse the monochromatic beam producing one pulse per revolution. Two slit packages are available with the curvatures and the slit lengths optimized for 1.5 Å and 4 Å neutrons, respectively. The chopper rotates at a speed of 10,000 to 18,000 rpm depending on the condition for frame overlap. Both the chopper and secondary collimator are mounted on an optical bench permitting easy interchange of the collimators and of the relative positions of the collimator and chopper. Thus, the chopper is normally placed as close as possible to the sample to reduce the time spread of the incident pulse, although for certain experiments, it may be advantageous to place the collimator closer to the sample. Under normal operating conditions, an additional collimator is used to eliminate scattering from the chopper. Various other components such as beam monitor and a collimating diaphragm may also be mounted on the optical bench.

The sample area consists of an aluminum drum with thin windows for the incident and scattered beams. The drum will be designed to support a secondary vacuum so that it may be used as the outer wall of a cryostat or furnace thus eliminating one containment wall in the beam path.

BEST COPY AVAILABLE

The flight path is shielded by 6" of paraffin and 1" of boron carbide and has an inner lining of cadmium sheeting in order to minimize the neutron background. The entrance window of the flight path is constructed from pure 0.04" thick aluminum curved around a supporting frame and bolted to the flight path with a vacuum seal such that the whole flight path may be evacuated. The detection system consists of 71 18" active-length, 1" diameter detectors filled with 4 atmospheres of He-3 covering the range of scattering angles from 25° to 120° and 20 similar detectors of 9" active length covering the range from 10° to 25°. At a later date, a small angle detection system will be implemented consisting of an array of linear position-sensitive detectors allowing the Debye-Scherrer rings to be mapped out directly under software control. A radial collimator to be placed between the sample chamber and the flight path is under design. The function of this collimator is to ensure that the detectors only "see" scattering from the sample, thus eliminating background scattering from sample containment vessels and the chamber itself. The collimator is made to oscillate in order to give a uniform transmission over the whole angular range of the detectors. Lastly, a second beam monitor and the final beam stop are mounted on the outside of the flight path after a 0.12" thick aluminum exit window.

The associated electronics have been specified and the system in now undergoing tests. A dedicated Microvax II will control and collect data from the instrument interfaced via a Camac system. The Camac control features include programmable modules to drive the stepping motors, input registers to read the corresponding coder information and interrupts to control error events at the instrument level. The Camac also features a memory histogrammer linked via a dedicated bus to two 32K, 16-bit memories in which the incoming data from the TOF unit may be directly histogrammed as a function of detector number and TOF channel. The advantage of this system is that the memory may be extended at a later date, if necessary, simply by adding more memory modules. The data in the Camac memories may be simultaneously displayed and transferred to the Microvax II by the Camac bus by direct-memory access.

Table 1 shows the calculated elastic resolution of the instrument for 1" detectors.

Table 1. Elastic Resolution (FWHM μeV) For 1" Diameter Detectors.

WAVELENGTH (A)			
	40	20	10
4	140	80	50
6	30	30	18

BEST COPY AVAILABLE

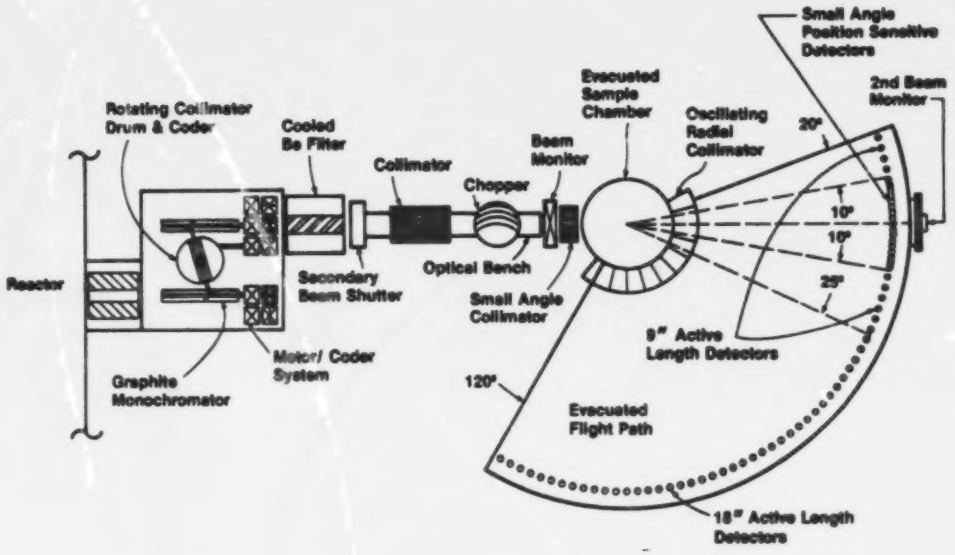

Figure 1. The NBS neutron time-of-flight spectrometer.

THE PHASE SHIFT AND MULTIPLE SCATTERING IN SMALL ANGLE NEUTRON SCATTERING: APPLICATION TO BEAM BROADENING FROM CERAMICS

N. F. Berk

and

K. H. Hardman-Rhyne
Inorganic Materials Division

Small angle neutron scattering from ceramic materials in early stages of processing, including the powder and green state, usually is characterized by the observation of "beam broadening" --an apparent broadening of the incident beam well beyond instrumental resolution and the absence of a weakly scattered component, in contrast to the typical SANS diffraction experiment. Since this behavior is generally observed to depend strongly on the wavelength, λ, of the incident beam it is sometimes assumed to be desirable as multiple refraction. In fact, λ-dependent beam broadening is a signature for incoherent multiple scattering which, in terms of the underlying single-particle phase shifts may be far removed from the refractive regime of very large single-particle phase shifts. Indeed, for particle or void sizes of typical concern in such materials, say radii, R, encompassing the range 0.1-10 μm, the phase shift

$$\nu = 2R\rho\lambda \qquad (1)$$

BEST COPY AVAILABLE

where ρ is the scattering length density, will tend to lie in a regime (0.1-10) not evidently characterized as either refraction, $\nu \to \infty$, or diffraction, $\nu \to 0$. Thus it is useful to incorporate the ν-dependence of the single-particle scattering into a formalism for incoherent multiple scattering from a population of particles or voids[1]. While such an approach falls short of the dynamical scattering theory ultimately required for such complex systems, it does provide a means of dealing with actual data and of helping to sharpen some of the basic concepts[1,2].

We have assumed that the SANS intensity is the result of incoherent multiple scattering from monodisperse, randomly distributed, structureless spheres in a uniform background. Then, the neutron cross-section per unit of area from sample of thickness z and area A, as a function of wavevector $Q^{\rightarrow}$ in the plane of a two-dimensional, position sensitive detector, and with pinhole collimation, is [1,3,4]

$$W(Q|z) = e^{-\bar{z}}\delta(\vec{Q}) + \frac{kR}{2\pi}\int_0^2 \zeta J_0(QR\zeta)\left[e^{-\bar{z}(1-q(\zeta))}e^{-\bar{z}}\right]d\zeta \qquad (2)$$

where $q(\zeta)$ in the exponent is completely determined by the single-particle, ν-dependent, cross-section,

$$\sigma(Q,\nu) = k^2R^4\left|\int_0^1 J_0(xu)\left[e^{i\nu\sqrt{1-u^2}} - 1\right]udu\right|^2. \qquad (3)$$

In lowest order, $O(\nu^2)$, the right hand side of (3) easily reduces to the Born approximation or diffraction limit. Also in (2), the scattering power $\bar{z} = z/\ell$, where ℓ is the scattering mean-free-path.

Numerical evaluations of $q(\zeta)$ are shown in figure 1 for a range of ν. For $\nu \leq 1$ the curves are indistinguishable to within 0.1% from the diffraction limit ($\nu \to 0$)

$$q^0(\zeta) = \theta(2-\zeta)\left\{(1 + \xi/2)\sqrt{1-\xi} - 2\xi(1 - \xi/4)\ln\left[\frac{2}{\xi}(1 + \sqrt{1-\xi}\right]\right\}, \qquad (4)$$

with $\xi = \zeta^2/4$. Even for $\nu = 2$ Born approximation is effectively stable but breaks down quickly for larger values, as shown. The leading singularity of $q(\xi)$ at $\xi = 0$ is determined entirely in $O(\nu^2)$ and is thus the same as in the diffraction limit, which from (4) is given by $1/2\zeta^2\ln\zeta$. It is this singularity which fixes the

BEST COPY AVAILABLE

asymptotic fall of $\sigma(Q)$ as $Q \to \infty$ and gives the Porod law, which is thus seen to be invariant in ν[1,6]. Moreover, the N-fold single-particle limit, where N is the number of particles, defines the $Q \to \infty$ behavior of the multiple scattering since the asymptotic behavior of (2) is determined by the leading singularity of the integrand at the origin; and since $q(\zeta) \to 1$ as $\zeta \to 0$, this is established in $O(\bar{z})$ and is the singularity of $q(\zeta)$[1]. Thus, for $Q \to \infty$, $NAW(Q|z)/V \to N\sigma(Q,\nu)/V \sim P/Q^4$, where $P = 2\pi(S/V)$ is the Porod constant, and S is the total surface area of the N particles.

These ideas have been successfully applied to a SANS beam broadening study of high purity alumina (Al_2O_3) powder[2]. Equation 2 was used to fit the curvature κ of measured intensity curves at $Q = 0$ for several incident neutron wavelengths, allowing the determination of ϕ and R--interpreted as an effective radius, see below. Parameters were in the ranges: $\lambda = 0{,}45\text{-}1.0$ nm, $z = 2.0\text{-}10.0$ mm, $\phi = 0.25\text{-}0.33$, and $\bar{z} = 5\text{-}400$. The corresponding phase shifts, $\nu = 0.15\text{-}0.30$, were well within the limit shown above, figure 1, to justify analysis as multiple diffraction. To apply the method to polydispersed powder, the radius measured from the small-Q data was interpreted as an effective radius, R(0), defined by the rigorous extension,

$$\bar{z} = N\sigma/A \to z\phi\langle\sigma\rangle/\langle v\rangle \to z\phi\nu^2\lambda^2 R(0), \qquad (5)$$

where $\langle\cdot\rangle$ denotes the average over the particle-size distribution (PSD). The last equivalence in (5) applies only to the diffraction regime, where $\sigma \to \sigma^0 = 1/2\nu^2\pi R^2$ (13), and $R(0) = \langle R^4\rangle/\langle R^3\rangle$. The best fit determination of R(0) from all data was found to be 265 nm within a 2-5% uncertainty. Once R(0) is known, all the small-Q data can be represented on a universal curve for multiple diffraction, $r_c[QR]$ vs $\bar{z}$, where $r_c[QR] = 1/\sqrt{-\kappa}$ is the radius of curvature of the scattered intensity at $Q = 0$ in dimensionless units and is effectively a measure of the width of the intensity curve near the origin[1]. This is shown in figure 2, comprising the results from 25 data sets, where the theoretical curve is well-approximated in the range shown by

$$r_c[QR] = 0.92[\bar{z}\ln^{0.85}\bar{z}]^{0.5} \qquad (16)$$

BEST COPY AVAILABLE

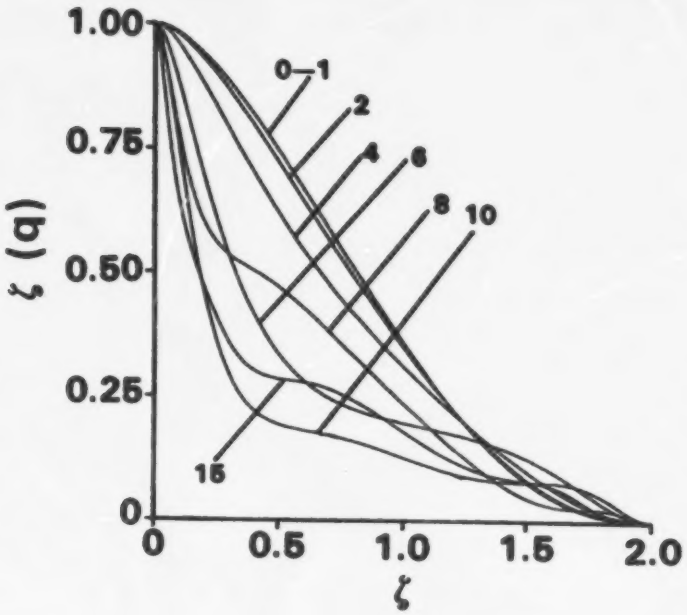

Figure 1. The function q(ξ) for several values of the phaseshift ν.

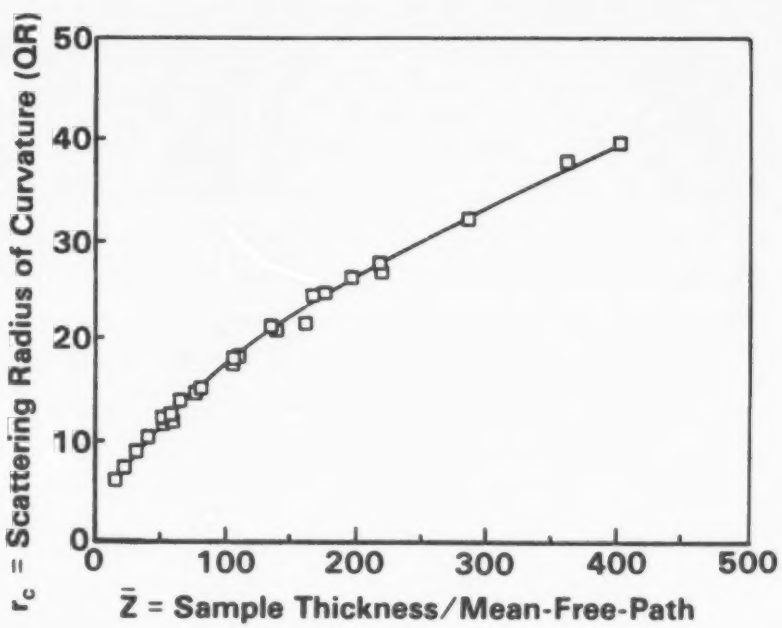

Figure 2. Radius of curvature of multiple scattering intensity at Q = 0.

BEST COPY AVAILABLE

For the limit of single-particle scattering by a sphere, $r_c[QR] = \sqrt{(5/2)}$. Large-Q data were analyzed using the Porod law, expresssed in terms of the effective particle radius $R(\infty) = \langle R^3 \rangle / \langle R^2 \rangle$, which results from its extension to polydispersed systems. The result[2] was $R(\infty) = 232$ nm within 15%. The values of $R(0)$ and $R(\infty)$ were rationalized by assumption of a lognormal PSD, from which $\langle R \rangle = 171$ nm and dimensionless width parameter $\beta = 0.382$ were derived. These results were found to be in good agreement with powder size determinations by laser light scattering and by x-ray sedigraph methods[2].

1. Berk, N. F. and Hardman-Rhyne, K. A. (1985). J Appl. Cryst., 18, in press.
2. Hardman-Rhyne, K. A. and Berk, N. F. (1985). J. Appl. Cryst., 18, in press.
3. Snyder, H. S. and Scott, W. T. (1949). Phys. Rev. 76, 220.
4. Bethe, H. A. (1953). Phys. Rev. 89, 1256.
5. Weiss, R. J. (1951). Phys. Rev. 83, 379.
6. Berk, N. F. and Hardman-Rhyne, K. A. (1986). Proceedings of the 1985 Santa Fe International Conference on Neutron Scattering, Physica B, to be published.

STUDY OF PLASMA SPRAY COATINGS BY SMALL ANGLE NEUTRON SCATTERING

S. F. Trevino
(U.S. Army Armament R and D Center, Dover, NJ)
and
(National Bureau of Standards, Gaithersburg, MD)
and
N. F. Berk

Yttria stabilized Zirconia is used as a coating in various applications, which coating is produced by the techniques of plasma spraying. It is of interest to measure the size of pores and their density in these spray coatings to determine their role in the physical properties of the coatings. Small angle neutron scattering measurement in the multiple scattering regime were performed on four samples of the coatings consisting of 7% yttria with no heat treatment Z7Y(0) and 100 hours of heat treatment Z7Y(100) and corresponding 8% yttria Z8Y(0), Z8Y(100). Incident neutron wavelengths of 10, 12, and 14 A were used. Using the theory of multiple scattering developed at NBS (See N. F. Berk and K. A. Hardman-Rhyne -- elsewhere in this summary) it is possible to determine the relationship between the diameter of the pores and their volume fraction for any given spectrum. These are plotted in figure 1 for the four samples and various wavelengths. The point of

BEST COPY AVAILABLE

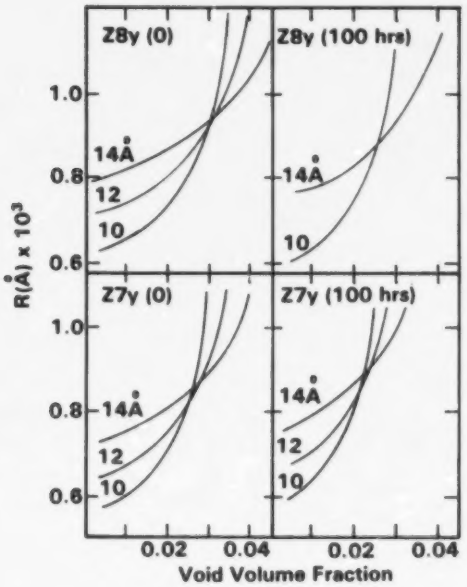

Figure 1. A plot of the pore diameter R vs volume fraction for four samples s determined by SANS spectra obtained with 10, 12 and 14 A wavelength neutrons.

intersection of the curves for the several wavelengths is taken as determining the radius and volume fraction. To our knowledge this is the first quantitative such use of small angle neutron scattering from these materials.

CRITICAL FLUCTUATION AND PHASE BEHAVIOR OF A BINARY POLYMER SYSTEM

C. Han and B. Bauer
(Polymers Division)

and

Y. Muroga
(Nagoya University, Nagoya, Japan)

and

M. Okada
(Tokyo Institute of Technology, Tokyo, Japan)

and

Q. Tran-Cong
(Kyoto University, Kyoto, Japan)

I. Introduction

For a binary polymer blend, the concentration fluctuation length near the phase boundary may be described by the Ornstein-Zernike[1] form in the small q region which in turn gives a Lorentzian shape for the static structure factor.

BEST COPY AVAILABLE

$$S(q)/S(q=0) = \frac{1}{1 + q^2\xi^2} \qquad (1)$$

Recently, P. G. deGennes has obtained S(q) for binary polymer blends in one phase for all q-regions[2,3]. This calculation is based on the random phase approximation together with the mean-field model. The structure factor S(q) can be expressed as

$$\frac{K_N}{S(q)} = \frac{1}{\phi_A z_A v_A S_D(A)} + \frac{1}{\phi_B z_B v_B S_D(B)} - \frac{2x}{v_o} \qquad (2)$$

with

$$K_N = N_A \left(\frac{a_A}{v_A} - \frac{a_B}{v_B}\right)^2 \qquad (3)$$

here N_A the Avogadro's number; a_i, v_i, ϕ_i, and z_i are the scattering length, molar volume, volume fraction and the degree of polymerization of the i^{th} component; $S_D(i)$ is the Debye function of i^{th} polymer; χ is the binary interaction parameter and v_o is the molar volume of a reference cell.

By expanding the Debye function up to the second moment, eq (2) is reduced to the Ornstein-Zernike form as in eq (1). The correlation length ξ can be expressed as:

$$\xi^2(T,\phi) = \frac{\overline{b^2}}{36} \left[\phi_A\phi_B(\chi_x - \chi)\right]^{-1} \qquad (4)$$

with χ_s as the interaction character χ at spinodal temperature, Ts. and b as the statistical segment length of polymer.

Since the correlation length ξ normally expands a range from a few tens of Angstroms to a few hundreds of Angstroms in a convenient temperature range for binary polymer systems, small angle neutron scattering provide just this wave length (q^{-1}) range with sensitivity when one of the polymers is deuterated. Therefore, SANS technique is used in this study to provide all static information. We may notice that $\frac{\chi}{v_o}$ can be easily obtained from Eq. 2 as q approaches zero. Therefore, the same set of SANS measurements provide both ξ and χ/v_o as a function of T and ϕ in the miscible region.

BEST COPY AVAILABLE

By extrapolating ξ to its infinite value, one could obtain the spinodal temperature of the system for that volume fraction. Therefore, a complete phase diagram can be constructed in this fashion, as will later be demonstrated in the results section.

II. Experiments

Aionically polymerized deuterated polystyrene (dPS) with $M_w = 4.35 \times 10^5$ and $M_w/M_n = 1.45$ was used as one component in this experiment. The other component is a cataionically polymerized and fractionated poly(vinylmethylether) (PVME) sample, with $M_w = 1.88 \times 10^5$ and $M_w/M_n = 1.32$. This molecular weight ratio was chosen to match the contour length of both components approximately.

Small angle neutron scattering, (SANS), experiments were performed at the SANS facility at the National Bureau of Standards.

III. Results and Discussion

Two kinds of SANS data were obtained for each volume fraction. First, a total detector count, I_{tot} was taken as a function of temperature during heating-cooling cycles. This provides a sensitive method to define the one phase region which is needed for the second part of the SANS experiment. The second kind of SANS data was

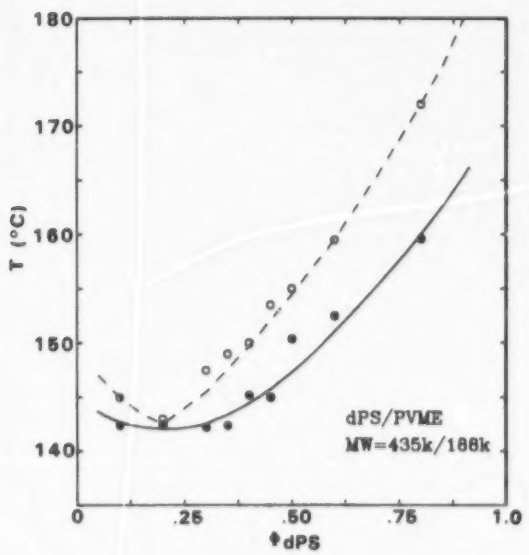

Figure 1. Phase diagram of ^{d}PS/PVME blend with MW=435k/188k. Solid circles and open circles are cloud points and spinodal points respectively.

BEST COPY AVAILABLE

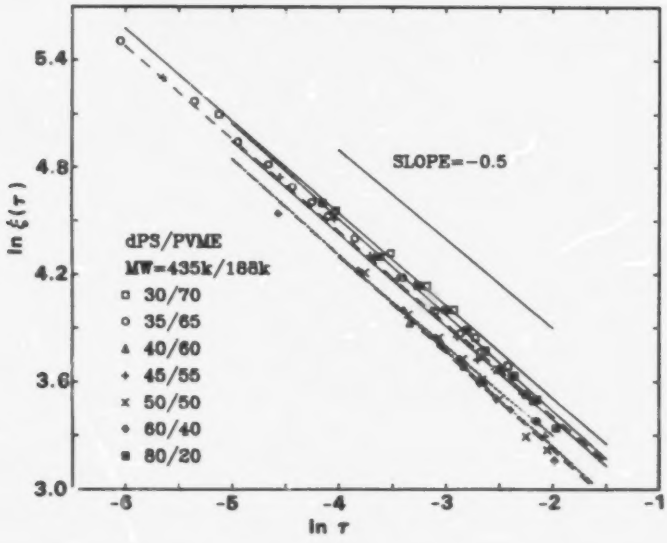

Figure 2. The reduced temperature dependence of the correlation length, ξ, for various compositions. A solid line with slope of -0.5 is drawn for comparison.

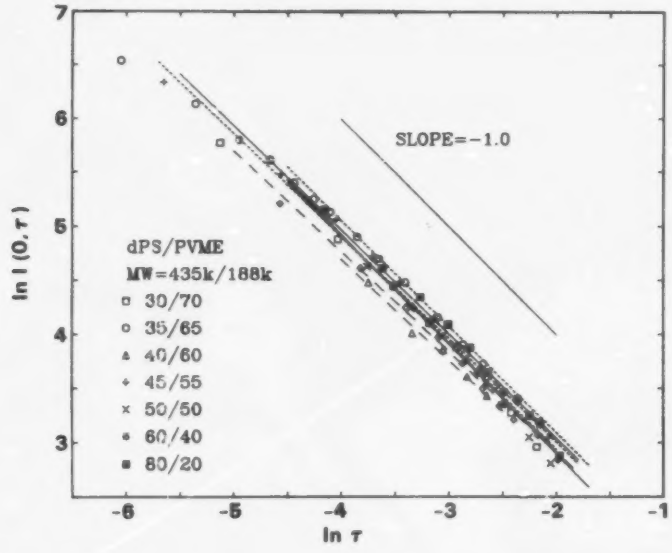

Figure 3. The reduced temperature dependence of S(q=0) for various compositions. A solid line with slope of -1.0 is drawn for comparison.

BEST COPY AVAILABLE

obtained and normalized as S(q) for various temperatures below cloud point temperature, T_c, which was obtained as described above. This structure factors, S(q), at various temperature and volume fraction was then fitted according to eq (2) with a non-linear regression routing to obtain χ/v_o and the statistical lengths used in the Debye functions. Then, the correlation lengths were calculated according to eq (4).

The linear dependence of χ/v_o on 1/T is then checkd. This 1/T dependence together with Eq.(4) implies a relationship of

$$\xi^{-2} \alpha |T - T_s| \qquad (5)$$

Equation 5 provides a procedure of extrapolating ξ^{-2} against T to obtain the spinodal temperature, T_s, which is the temperature where $\xi \to \infty$ (or $\xi^{-2} \to o$). With the cloud points and spinodal temperatures, the phase diagram is constructed and displayed in figure 1. The mean-field nature of a polymer-polymer binary system can be easily demonstrated through the critical exponents of $\nu = 1/2$ and $\gamma = 1$ where

$$\xi = \xi_o \left| \frac{T - T_s}{T_s} \right|^{-\nu}$$

and (6)

$$S(q = 0) = S_o \left| \frac{T - T_s}{T_s} \right|^{-\gamma}$$

In figure 2 and 3, $\ell n\ \xi$ and $\ell n\ S(q = 0)$ is displaced as a function of $\ell n\ \tau$, with $\tau = \frac{T - T_s}{T_s}$ for various compositions.

These equilibrium results have clearly demonstrated the mean-field nature of a binary polymer system. Also the phase diagram and χ parameters have been used to evaluate spinodal decomposition binetics of the same system[4,5].

---

1. L. S. Ornstein and F. Zernike, Proc. Acad. Sci., Amsterdam, 17, 793 (1914).
2. P. G. deGennes, J. de Physique, 31, 235 (1970).
3. P. G. deGennes, J. C P. 72, 4756 (1980).
4. C. C. Han, M. Okada, Y. Muroga, B. J. Bauer and Q. Tran-Cong. SPE ANTEC '85 Conf. Proc. 306, 43, (1985).
5. C. C. Han, M. Okada, YU. Muroga, F. L. McCrackin, B. J. Bauer and Q. Tran-Cong, Polymer Engineering and Science, (in press).

BEST COPY AVAILABLE

REACTOR RADIATION DIVISION AND COLLABORATIVE PROGRAMS

SMALL NETWORK STRUCTURE STUDIED WITH SMALL ANGLE NEUTRON SCATTERING

Wen-li Wu and B. J. Bauer
(Polymer Division)

The network structure of thermosetting resins used as composite matrix materials largely determines some of the key properties for composite materials. This structure refers to the arrangement of chemical crosslinks which converts the liquid monomers into a rigid solid. The network structure in these materials is not amenable to characterization by standard techniques such as small angle x-ray scattering, electron microscopy, nuclear magnetic resonance, etc. One of the major aspects characterizing the network structure within epoxies is the spatial distribution of the crosslinks. Work over the past two years has demonstrated that elastic neutron scattering has the unique potency for addressing this problem. Neutron measurements have been carried out successfully to characterize the molecular networks in one of the commonly used types of resins - i.e., the expoxies. A partially deuterated diglycidyl ether of Bisphenol A (DGEBA) and a curing agent based on polypropylene oxide diamine were chosen as the model system for the study. The neutron scattering results can be analyzed by expressing the scattered intensities in terms of a form factor of an individual network of infinite molecular weight. Based on this formulation, the average size of the mesh and the rigidity of the network could be deduced from the scattering data. In addition, a decade-old controversy concerning the homogeneity of the networks within thermosets can now be treated analytically using this neutron technique. The heterogeneity in epoxies can be divided into two categories; the compositional fluctuation and the topological fluctuation. Schemes to quantity these two types of heterogeneity have been developed.

In an effort to broaden the molecular weight distribution between crosslinks, polymers of different molecular weight were blended together and cured with a stoichiometric amount of epoxy monomers. The molar ratio of the long chain amine (D-2000) to the short chain amines (D-400 to D-230) were kept at either 1.0 or 0.5. Every one of these cured mixtures gave rise to a pronounced scattering maximum at a Q value smaller than those observed in the epoxy containing only one of the contituent amines (see figure 1). Theoretical consideration based on this experimental observation strongly suggested that the long chain and the short chain diamines incorporated themselves within the epoxy network in a highly regular manner. The connecting linkage between a pair of short chain diamines is a long chain diamine and

BEST COPY AVAILABLE

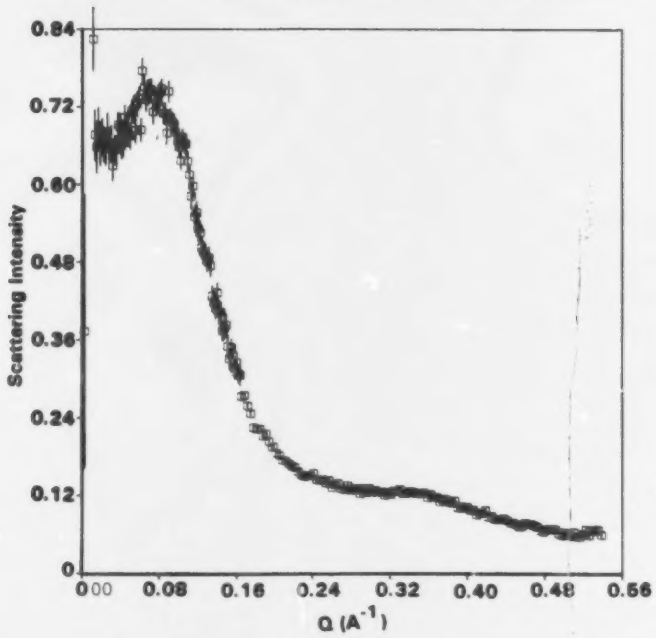

Figure 1. Small angle neutron scattering pattern from a cured epoxy. The multi-peaked structure in the pattern is due to the formation of a semi-regular network of chemical crosslinks. For the measurement the crosslinking agent was deuterated to enhance scattering contrast with the matrix.

vice versa. Such a regularly alternating block structure within a amorphous material is rather striking. Work is now in progress to identify the mechanism of this regular network formation which can not be understood in terms of our current knowledge about epoxies.

SANS STUDY OF A CONCENTRATED PROTEIN SOLUTION

R. Nossal
(National Institutes of Health, Bethesda, MD)

and

S. H. Chen
(Massachusetts Institute of Technology, Cambridge, MA)

and

C. J. Glinka

Small angle neutron scattering (SANS) has been used to examine concentrated aqueous solutions (up to 20% by weight) of the protein bovine serum albumin (BSA)[1]. At higher protein concentrations, the scattering data shown distinct features which can be ascribed to strong intermolecular interactions. For example,figure 1 shows the scattering for various concentrations of BSA in D_2O buffered with 0.03 molar

BEST COPY AVAILABLE

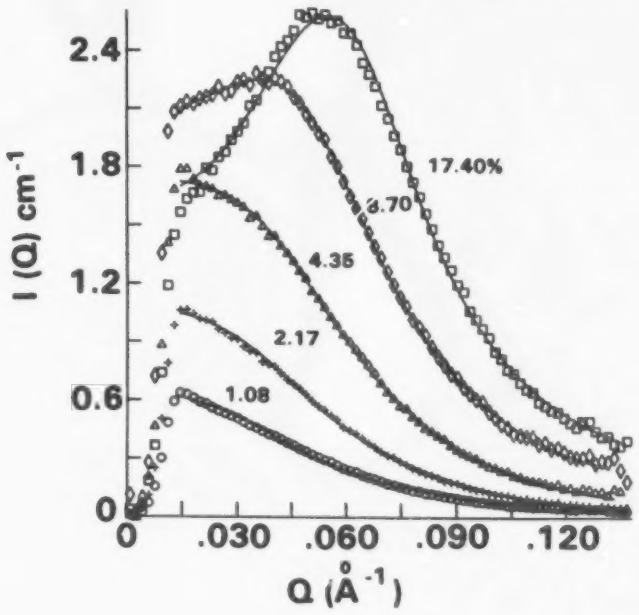

Figure 1. Differential scattering cross section, I(Q), for various concentrations of BSA in 0.03 M k Acetate. Solid lines are computer-fitted spectra (see text).

potassium acetate. The pronounced peak which develops in these data with increasing protein concentration is caused by the mutual repulsion of the proteins which imposes well defined nearest neighbor spacing (inversely related to the peak position) on the system. The solid lines are fits to a theoretical model of the interparticle potential consisting of a hard-core plus an exponentially decaying "tail". For moderate ionic strength (0.03 M k Acetate, pH 5.9), the intermolecular interaction agrees with the double layer repulsive part of the well-known DLVO theory for interacting colloidal particles. These results demonstrate that it is possible to determine size parameters and surface charge of proteins in dense solutions. At high salt concentration (> 0.2 M NaCl) the data can be fitted by the same potential model, although interpretation in terms of DLVO theory is not possible. Even in this case, however, effective molecular size and potential parameters can be determined.

---

1. R. Nossal, C. J. Glinka and S. H. Chen, submitted to Biopolymers.

BEST COPY AVAILABLE

JOINT NEUTRON AND X-RAY STRUCTURAL REFINEMENT OF PORCINE INSULIN.

A. Wlodawer and H. Savage.

Joint x-ray/neutron refinement of insulin has been performed using 2.2A neutron data collected on the BT8 flat cone diffractometer at the NBS and 1.5A x-ray data provided by Dr. G. Dodson, University of York, England. Several different models were calculated, using the x-ray structure as a starting point. The first model was essentially a refinement of the x-ray data alone, lowering the R-factor to 0.148. Next, 24 cycles of joint refinement resulted in a model with R factors of 0.176 and 0.199 respectively for the x-ray and neutron data. The main problem with this model was posed by the movement of solvent atoms out of x-ray density, particularly severe for alternately occupied sites closer than 2A. Another model was calculated by fixing solvent positions to the initial values and allowing only the atomic positions belonging to the protein to refine. Finally, occupancies of amide hydrogens were refined using neutron data only in order to study hydrogen exchange in the crystals. The R factors in the final model were 0.183 (x ray) and 0.191 (neutron). The bond lengths deviated by 0.02A from their ideal values.

The structure of two insulin molecules present in the asymmetric unit was compared in order to correlate the differences with the crystal packing. The two crystallographically distinct molecules differ by the following RMS deviations: 1.88 A in their positions of all non-hydrogen atoms and 2.23A for all atoms. This apparent discrepancy is due mostly to concerted rearrangements in which the individual elements of secondary structure such as α helices do not vary in an appreciable manner, but their relative positions are strongly influenced by crystal packing forces. The overall average temperature factors for the two molecules were very similar (18.5A^2 and 17.0A^2). However, large local differences were observed in regions connecting α helices and irregular parts of both terminii of the chain B. A number of hydrogen positions could be found directly in the neutron density maps, showing that all histidines were fully protonated, and confirming direct bond between histidine B10 and the zinc, without an intervening hydrogen.

The pattern of protection of amide hydrogens from exchange is strikingly different in insulin than in any other proteins studied so far - see figure 1. The only region of significant protection under experimental conditions employed by us (over four months soak of crystals at pH=6.5) was found in the center of the helical region in the B chains (residues 14-19 in molecule 1 and 12-19 in molecule 2). No significant protection of amide hydrogens was observed in areas of β sheet. Insulin is comparatively less rigid than proteins such as BPTI and ribonuclease and thus is more

BEST COPY AVAILABLE

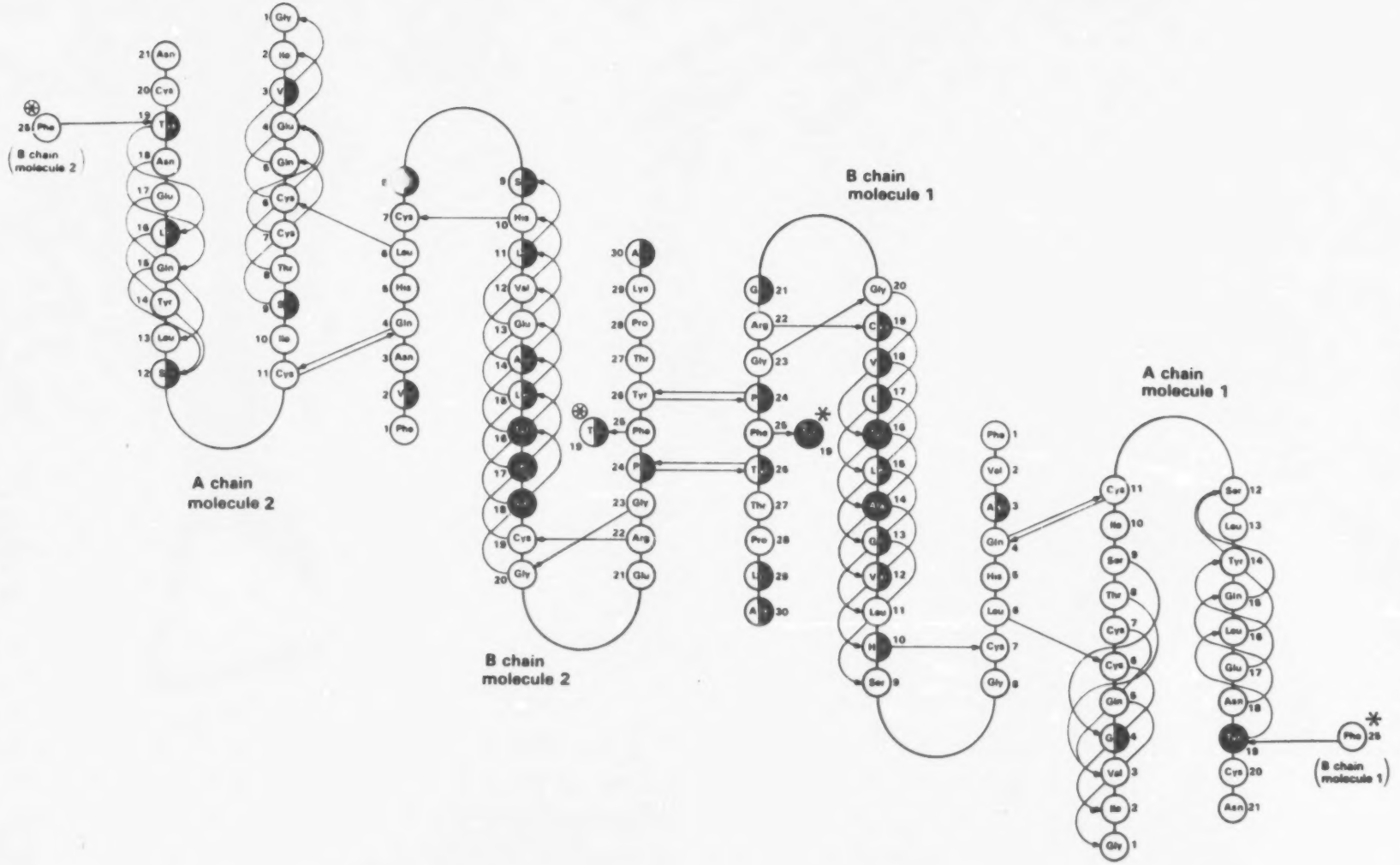

Figure 1: Diagram of the hydrogen bonds involving the main chain atoms and the level of protection of the amide hydrogens (H exchanged for D): Black residues are fully exchanged, half black/white are partially exchanged and the white residues are unexchanged.

susceptible to processes leading to exchange which is in good agreement with the available solution exchange data.

Most of the strongly bound solvent appears to occupy similar positions in the neutron and x-ray $2F_o-F_c$ maps but, there were significant differences in the more disordered regions away from the protein surface.

NEUTRON ACTIVATION AUTORADIOGRAPHY STUDY OF PAINTINGS

Yu-Tarng Cheng, M. J. Blackman and J. S. Olin
(Smithsonian Institution, Washington, DC)
and
(National Bureau of Standards, Gaithersburg, MD)
and
Martin Ganoczy

The engineering detailing study to produce construction drawings for the proposed autoradiography facility at the NBSR is nearly completed. The study will give a more accurate estimate of the anticipated construction cost. Meanwhile, a fund raising effort has been coordinated by the Smithsonian Institution to secure financial support for the proposed new facility.

Due partly to the shortened reactor schedule last year only one printing was studied using the existing thermal column facility. The study of the 17th century Dutch Master painting "The Portrait of a Woman" was in collaboration with the New York Metropolitan Museum of Art where a number of old master paintings have been studied using the medical reactor at Brookhaven National Laboratory. The autoradiography study can provide informations concerning the artist's style, technique, construction of painting images and type of pigments used. This information then becomes an integral part of an interdisciplinary study of art history of the said artist along with results from other painting examination methods.

If the neutron activation autoradiography technique is to gain acceptance among people interested in studying paintings, the radiation dosage of about 300 rads that the painting is subjected to during the activation process, though small by industrial standards, must be addressed. We have reported last year concerning the study of the image recording efficiency of different film systems, as a more efficient autoradiograph recording system would reduce in direct proportion the amount of radiation the painting received. The Kodak XAR film together with a Du Pont Quanta III scintillation screen appears to be the most effective. However, the

BEST COPY AVAILABLE

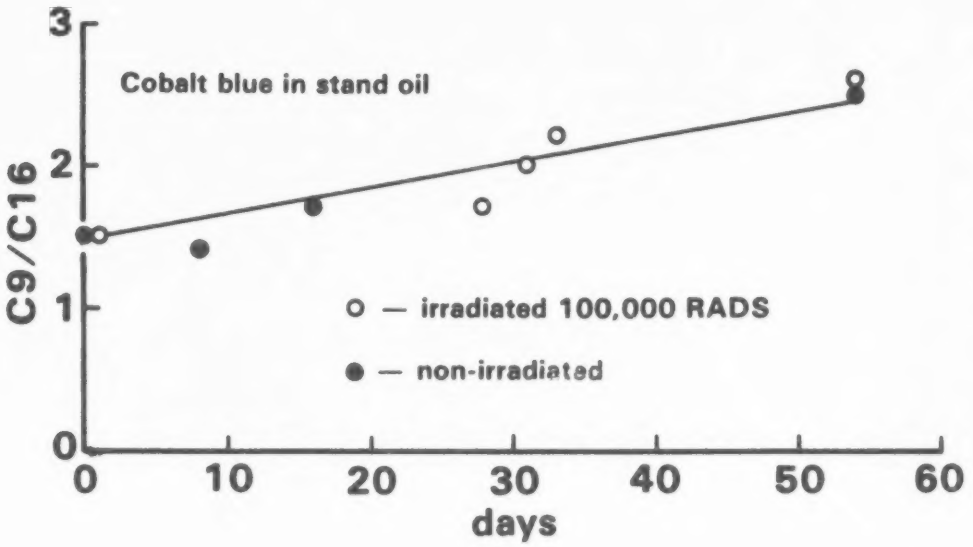

Figure 1. Ratio of azelaic (C_9) to palmitic (C_{26}) acids in irradiated and non-irradiated raw number paint samples as function of time.

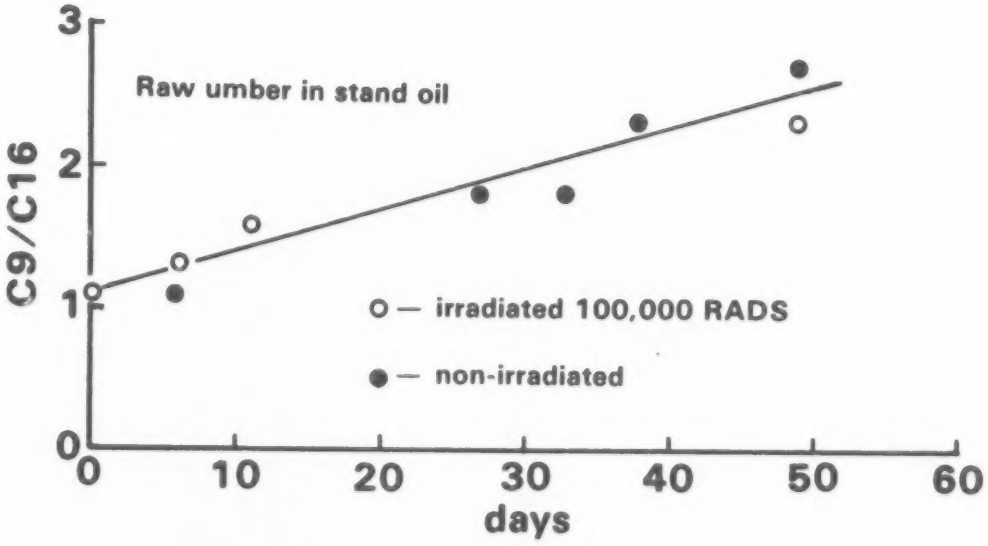

Figure 2. Ratio of azelaic (C_9) to palmitic (C_{26}) acids in irradiated and non-irradiated cobalt blue paint samples as function of time.

BEST COPY AVAILABLE

increase in the imaging speed is accompanied by certain trade offs. Elements that emit very low energy beta particles do not benefit from the scintillation screen system because the low energy beta particles are being stopped within the plastic film base before it can reach the scintillation screen. Reducing the painting activation level by using the faster imaging device will then also reduce the sensitivity for studying elements with very low energy beta particles.

In connection with the film efficiency study, another project was initiated in the past year to investigate the effects of the small amount of radiation on the natural aging process of painting materials. Eight commercially prepared pigments were mixed in with linseed oil and then thinly painted on microscope glass tray. Half of the samples were left as control and the other half were subjected to 100,000 rads of gamma radiation. The dosage level was chosen to eliminate the uncertainty about threshold effects. Gas chromatography technique was used to monitor the chemical changes, that being the formation of C_9 from the breaking down of unsaturated long carbon chains in the linseed oil. Figure 1 and 2 show the growth of C_9 normalized to the saturated C_{16} amount in both irradiated and non-irradiated samples of raw number in stand oil and cobalt blue in stand oil. This type of aging test certainly requires time and statistics before any definitive conclusion can be drawn. The initial results indicate that the irradiated samples cannot be discerned from the non-irradiated ones. To accelerate the aging process, the common practice is to use raised temperature or UV irradiation. An UV chamber has been constructed to accomodate the use of both long and short wavelength UV sources. We will study the effects on the normal aging process of painting materials from UV and gamma radiation and also any possible synergistic effect.

BEST COPY AVAILABLE

NUCLEAR METHODS GROUP: OVERVIEW

R. Fleming
(Center for Analytical Chemistry)

The development and application of nuclear analytical techniques for greater accuracy, high sensitivity and better selectivity are the goals of the Nuclear Methods Group. A high level of competence has been developed in reactor-based activation analysis, which includes instrumental and radiochemical neutron activation analysis (INAA and RNAA), and in LINAC-based activation analysis using photons (PAA). In addition, the group has a unique capability in neutron beam analysis with both prompt gamma activation analysis (PGAA) and neutron depth profiling (NDP). The NDP technique utilizes prompt charged particle emission to determine elemental distributions within the first few micrometers of a surface while the PGAA technique utilizes prompt gamma-ray emission to measure the total amount of an element in a sample, regardless of its distribution. These techniques provide an arsenal of tools to address a wide variety of analytical problems in science and technology.

The activities during the past year have been dominated by the upgrade of the NBS Research Reactor to an operating power of 20 MW from its previous 10 MW level. The power increase and the associated repositioning of the irradiation tubes resulted in the NBSR being shutdown during the first half of the year and required a total recharacterization of our irradiation facilities. The reactor characterization has been completed and the Group's irradiation capability has been significantly improved. The result has been a doubling of the neutron flux available for both our beam and incore measurements, and the installation of the new cold neutron source. When completed, the Cold Neutron Guide Hall Facility will result in a least a one hundred times improvement in our sensitivity for NDP and PGAA measurements.

With the NBSR unavailable for use for the first half of the year, we had the opportunity to gain experience with other reactors. The ability to irradiate large samples in a well-thermalized neutron flux made the MIT reactor the facility of choice for bioanalytical measurements, especially for the activation of whole electrophoresis gels. The nearby light-water reactors at the University of Maryland (College Park) and the University of Virginia (Charlottesville) were used for a variety of irradiations. The relatively high fast-to-thermal neutron flux ratio at these latter two facilities made epithermal and fast neutron activation analysis convenient, especially for iodine and silicon.

BEST COPY AVAILABLE

Radiochemical neutron activation analysis (RNAA) continues to make significant contributions to the Group's measurement capability. The determination of tin in the milk powder, wheat flour and rice flour SRM's at the few ng/g level and the determination of gold and platinum in the human urine SRM at the few pg/ml level are examples of this work. The determination of platinum, in particular, at environmental baseline levels means that this important element can be added to the list of those which can be monitored in real samples.

Largely at the instigation of the Group's members, a new ASTM Task Group on Nuclear Methods of Chemical Analysis (E10.05.12) has been formed to insure that the ASTM standards in this area reflect the current state-of-the-art and to enhance communication within this community. After three meetings the group has over forty members and six active subgroups: Quality Assurance, Biology Medicine and Health, Geochemistry and Archeometry, Reactors, Neutron Generators, and Forensic Applications.

The Group's collaborative research with industry and other government agencies continues to increase. Thirteen fluoropolymer materials were analysed for over twenty elements with Dupont and a series of high purity quartz samples were analysed for Fort Monmouth. Neutron depth profiling continues a strong interaction with US industry on the measurement of elemental distributions in high-technology materials. In addition to our ongoing bioanalytical collaborations with NOAA, NIH, USDA and EDA, a new IAEA program in nutritional monitoring of the human diet has been initiated jointly with EDA and USDA.

The National Environmental Specimen Bank, which in prior years has been devoted to a pilot program of collecting, analysing and banking human liver samples under EPA sponsorship, has expanded this year to include several new sample types. Preliminary banking has begun on honey bee samples from EPA and on the USDA/EDA human diet samples. In collaboration with the NOAA Nation Status and Trends program, samples of marine sediment and fish liver and muscle are being banked. A goal for the coming year is the development of one or more of these materials as standards or reference materials.

The past year has seen a major upgrade in our detection and data analysis capability. A second front-end detector system (ND6700) has been installed for low level counting with two new germanium detectors. A duplicate ND 6620 counting system with an automated sample changer has been obtained for the analysis of the diet samples in the nutritional program. The VAX computer is now fully operational for data acquisition with its own sample changer. The addition of this improved data

BEST COPY AVAILABLE

acquisition and computational capability for modeling the measurement process will continue to enhance our accuracy and throughput for Activation Analysis.

During the coming year the Group will continue to consolidate the development of its data acquisition and computation capability and to apply nuclear methods to elements which are not done well presently. These new elements will include nickel, silicon and iodine by fast or epithermal NAA, nitrogen and phosphorus by thermal NAA with beta counting, and lithium and boron by neutron activation mass spectrometry. In addition to the ongoing application programs, work will continue in reducing and quantifying the various sources of systematic error in analysis by nuclear methods.

HIGH RESOLUTION NEUTRON DEPTH PROFILING (NDP) AND SECONDARY ION MASS SPECTROMETER (SIMS) OF BORON THROUGH OXIDE-SILICON INTERFACES

W. Vandervorst, F. R. Shepherd
(Bell-Northern Research, Ottawa, Canada)

and

R. G. Downing, J. T. Maki, and R. F. Fleming
(Center for Analytical Chemistry)

The neutron depth profiling (NDP) facility[1] has now been operational for three years at beam port-3 of the NBS Research reactor. During this time NDP has been used to profile the concentration of light elements in many high technology materials. The most frequent material analyzed has been the silicon based semiconductor[2], often covered with a thin oxide insulating layer. When boron in implanted through this oxide in the production of an electronic device it is of interest to understand the distribution of boron at and near the oxide-silicon interface particularly after the device has undergone thermal processing. Secondary ion mass spectrometry (SIMS), due to its high resolution and low detection limits, is widely used to profile boron implanted in silicon, however the presence of an oxide layer gives rise to rapidly changing sputtering yields, secondary ion yields, collisional mixing, and radiation enhanced diffusion near the oxide-silicon interface. This generates unreliable concentration profiles using SIMS under these conditions. On the other hand, matrix effects which complicate SIMS analysis are not a problem for NDP and make it an attractive method for checking the calibration factors needed to convert SIMS data to boron concentration and for identifying artifact peaks. This interface region is confined to a band a few nanometers in breath and requires higher resolution techniques than normally used for NDP profiling. In this work, higher depth resolution in NDP profiles has been achieved by employing a grazing exit geometry.

BEST COPY AVAILABLE

Since the dynamic range of sensitivity for the detection of B-10 with good resolution is less for NDP than for SIMS, the B-10 profiles can only be compared in regions where the concentration is greater than 10^{19} cm^{-3}.

In this work an N-type Si wafer with 194 nm of thermal oxide was implanted with B-10 ions at 70 keV to a dose of 10^{16} ions cm^{-2}. The wafer was analyzed by NDP and SIMS and then furnace annealed at 1000°C for 30 minutes in dry nitrogen for the second analysis.

Boron profiles were measured by NDP using the $^{10}B(\nu,\alpha)^{7}Li$ reaction. The typical depth resolution previously obtained was ≈40 nm^2. In order to imprové the depth resolution of the technique a grazing take-off angle was employed with the detector at 75° to the sample surface normal. In order to limit the variation in exit angles and because of the 1 cm spot of the neutron beam the detector was moved 15 cm away form the sample and a slit 1 mm wide was placed in front of the detector. This limited the angular variation to less than 0.1° but also reduced the intensity of the signal significantly. In this configuration the energy per ADC channel of 2.1 keV corresponds to ≈1.8 nm and since the energy resolution of the detector used was 12 keV, the depth resolution expected is ≈10nm.

SIMS depth profiles were recorded with an ion microscope equiped with a duoplasmatron ion source, primary mass filter, and a leak valve for flooding the specimen surface with oxygen. Depth profiles were generated using a 5.5 keV O_2^+ beam

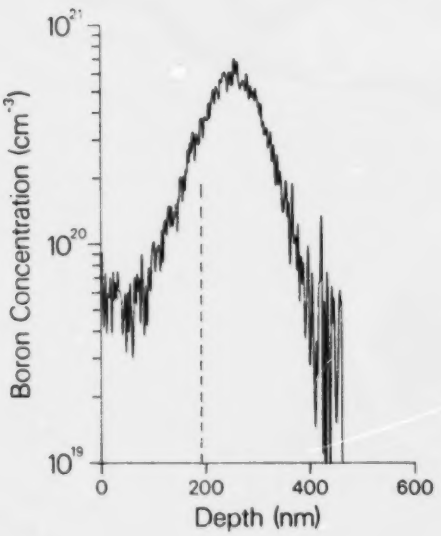

Figure 1. Neutron depth profile of a Si wafer implanted with 70 keV $^{10}B^+$ to a dose of 1 x 10^{16} cm^{-2} through 194 nm thermal oxide. The vertical dashed line indicates the location of the oxide-silicon interface.

BEST COPY AVAILABLE

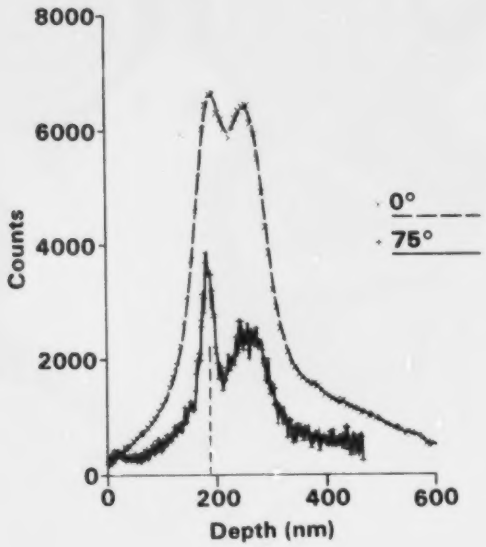

Figure 2. Neutron depth profiles of the sample from figure 1 measured after annealing at 1000°C for 30 minutes in dry nitrogen. The upper dashed curves (x) was recorded for normal emergence (θ=0°) and the lower solid curve (+) for grazing emergence (θ=75°) of the alpha particles.

rastered over 250 micrometers, and secondary ions were extracted from a 60 micrometer diameter central field with the energy slits wide open. An electron flood gun was used together with a microprobe imaging system[3] to ensure that charging was properly neutralized and that the detected signal was always being extracted from the center of the crater. Crater depths were measured with a surface profilometer.

Figure 1 shows the neutron depth profiles measured from the wafer. From the measured energy of detected alpha particles, the depth scale in figure 1 was established using stopping power values for Si from Ziegler[4]. Bragg's Law addition for SiO_2 and densities of 2.33 and 2.27 gm cm^{-3} were used for Si and SiO_2 respectively. The concentration scale has been established by equating the integrated counts to the implant doses (having been previously verified by checking against an NDP concentration standard). Note that the distribution of boron varies smoothly through the oxide-silicon interface at the depth of about 200 nm. The SIMS profile (not shown) gave an artifact peak at this location when analyzed for boron.

Figure 2 shown NDP's for the same specimen after annealing at 1000°C for 30 minutes in dry nitrogen. The upper curve shows the profile measured for normal emergence of the alpha particles. The lower curve, whose intensity has been multiplied by 3 in this plot shows the improvement in the depth resolution in the interface region (195 nm) obtained with grazing exit geometry (75°). Although the intensity is reduced, the grazing exit geometry shows a much higher resolution and

BEST COPY AVAILABLE

dynamic range for the segregation peak. At 0° only a variation of 10%-11% is observed whereas at 75° the signal varies by a factor of 2. The FWHM of the segregated boron peak is 20nm. The small peak at a depth of about 20 nm in the

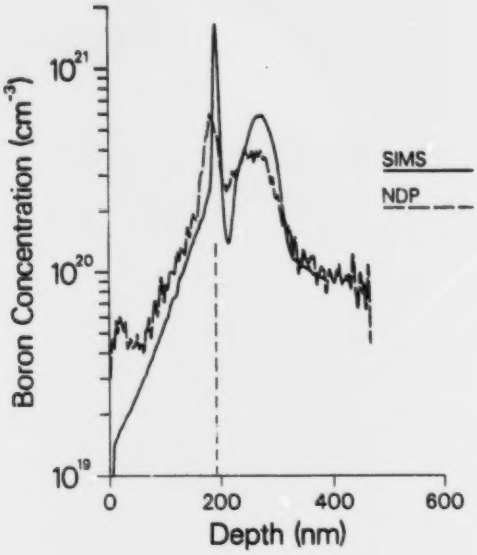

Figure 3. SIMS (solid line) and NDP (dashed line) data for the annealed sample normalized to a total B concentration f 8.4 x 10^{15} cm^{-2}.

spectrum recorded at 75 degrees is a weaker replica of the peak at 270 nm, and arises from another decay transition in the $^{10}B(n, \alpha)^{7}Li$ reaction. At normal emergence this replica is more displaced from the main alpha spectrum and is not seen in the upper curves in figure 2, but is present in the lower curve.

Measurements made by SIMS on the annealed sample were compensated for signal enhancements due to preferential sputtering, charging effects, sputtering rate variations, and by omitting the oxygen flooding due to loss in overall resolution. Both the SIMS and NDP curves are presented in figure 3. A sharp rise in boron concentration can be seen at the interface. Beyond the interface is an immobile boron peak followed by an "outdiffused" tail. The two curves are normalized to the total boron concentration of 8.4 x 10^{15} cm^{-2}, the balance of the implanted dose of 10^{16} cm^{-2} being continued in the long diffusion tail. Note that the SIMS profile resolves a much sharper (FWHM = 8nm) more intense segregated boron peak (labeled 'α' in figure 3) than the NDP data and that the broader peak at 270 nm is also more intense in the SIMS profile. The discrepancy between SIMS and NDP results near the surface (~20 nm) is largely associated with the interfering replica in the alpha spectrum discussed above. Aside from the intensity of the 2 main peaks, the remaining differences between the 2 curves in figure 3 appear to be associated with a

BEST COPY AVAILABLE

slight (≈3 nm) shift. Repeating the SIMS profile sometimes gave closer agreement in the peak positions and threfore may be associated with the overall error in determining the depth scale from crater depth measurements.

The integrated amount of boron in the interfacial peak (figure 4) is 2.4 x 10^{15} cm^{-2} from SIMS and 2.2 x 10^{15} cm^{-2} from NDP. The broader peak in NDP is probably a result of the lower depth resolution. The boron peak in the Si (labeled β in figure 3) is approximately the same width in both NDP and SIMS, and the integrated B concentration in this peak is 4.4 x 10^{15} cm^{-2} from SIM and 3.6 x 10^{15} cm^{-2} from NDP.

Although the discrepancy between SIMS and NDP in the intensity of the interfacial peak could be partly due to the difference in depth resolution, both techniques resolve peak β with approximately the same measured width. At these high boron concentrations, there may be an enhancement in the $^{10}B^{+}$ secondary ion yield particularly if the B is in a different chemical or structural form. Hofker[5] has reported a 30% enhancement in B^{+} yield at similar concentration levels, which would account for the high peak intensities observed in the SIMS profiles.

By using neutron depth profiling with grazing exit geometry to measure boron distributions in the region of oxide-silicon interfaces. A depth resolution of 10 nm has been achieved at 75° take-off angle. SIMS depth profiling of the same sample has been compared to NDP and the NDP technique used to determine total boron concentration. In the future, the depth resolution in NDP can be further improved when higher flux neutron sources are available and by incorporating a precision goniometer in the target chamber to allow high take off angles to be used.

Acknowledgements. The technical assistance of D. Johnston, from Surface Science Western Ontario, with the SIMS measurements is gratefully acknowledged. We wish to thank J. R. Ehrstein of the Center for Electrical and Electronic Engineering for supplying a number of the samples. We also wish to thank the staff of the NBSR for their kind assistance.

---

1. R. G. Downing, R. F. Fleming, J. K. Langland and D. H. Vincent, Nucl. Instr. and Meth., 18, 47 1983.

2. J. R. Ehrstein, R. G. Downing, B. R. Stallard, D. S. Simons and R. F. Fleming, in Semiconductor Processing, ASTM STP 850, edited by Dinesh C. Gupta, ASTM, 1984

3. J. D. Brown and W. Vandervorst, Surf. Int. Anal. (in press).

4. J. F. Ziegler, "Helium Stopping Powers and Ranges in All Elemental Matter", Pergamon Press, New York.

5. W. K. Hofke, Philips Research Reports Supplements, 1975, No. 8.

BEST COPY AVAILABLE

HIGH-SENSITIVITY DETERMINATION OF IODINE ISOTOPIC RATIOS BY THERMAL AND FAST NEUTRON ACTIVATION

Richard M. Lindstrom and George J. Lutz
(Center for Analytical Chemistry)

Methods for the determination of Iodine-129 concentrations and of I-129/I-127 ratios, to be most useful for studying the trasformations of iodine in the environment, must be capable of measuring concentrations down to the present-day background level, of order 10^8 atoms/gram (5 aCi/g), with acceptable precision and low blank. A neutron-activation procedure has been developed to perform reliable concentration measurements down to this level in a few grams of sample. I-129/I-127 ratios as low as 6×10^{-10} have been measured. Oxygen combustion is used both before and after irradiation to separate iodine. Bromine-82 and other interferences are efficiently separated by the use of gas-solid reaction with Hydrated Manganese Dioxide. Intense neutron irradiation is performed with optimized fluxes of both thermal and fast neutrons.

Experience with the University of Virginia Reactor at Charlottesville during the NBSR shutdown encouraged a detailed reexamination of the irradiation process with the goal of determining both iodine isotopes simultaneously. The parameters used in the calculation are as follows:

A sample contining 10^8 atoms of I-129 and 10^{-6} g of I-127.

12 hours irradiation time: one half-life of I-130.

6 hours elapsed time between the end of irradiation and the start of counting, during which time the radiochemical separtation of I is carried out.

16 hours counting time: overnight, somewhat over one half-life.

A counting efficiency of 0.03 counts per disintegration, that of a large high-resolution Ge detector with the source as close as possible to the crystal.

Thermal neutron capture cross sections for I-127, I-128, and I-129 are 6.13, 107, and 27 barns, respectively. The fission-spectrum cross section for the I-127(n,2n)I-126 reaction is 0.9 mbarn.

Mapped onto a space of thermal neutron flux versus fast (fission spectrum) neutron flux (figure 1), the analytically useful region is defined by four boundaries:

- The I-130 signal must be large enough to be detectable. If measurement is considered to be accomplished when 10 or more net counts are detected, then under the assumed experimental conditions the thermal neutron flux must exceed 5×10^{12} $n/cm^2 s$

BEST COPY AVAILABLE

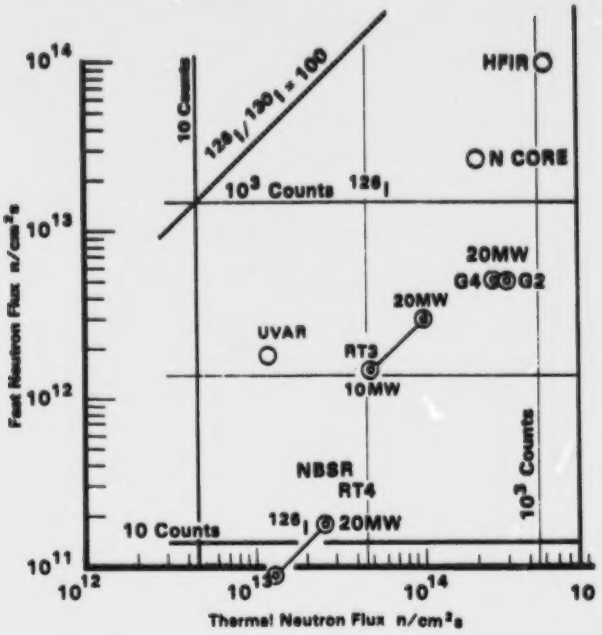

Figure 1. All double circles are NBS Reactor; single circles are other reactors.
UVAR - University of Virginia Reactor
N - Hanford N reactor, core position
HFIR - High Flux Isotope Reactor, ORNL
Conditions of calculation are: 10^8 atoms ^{129}I, 1 μg ^{127}I, 12 hour irradiation, 6 hour delay, 16 hour count, and ε=0.03 count/disintegration.

- The I-126 signal must be detectable. If 10 counts are detectable, the fast flux must exceed 1.4×10^{11} n/cm^{2}s.
- Iodine-130 can be produced from triple neutron capture on I-127 as well as by single capture on I-129. This interfering signal is proportional to the cube of the thermal flux. If no more than 50% correction for this effect is tolerable, the thermal flux cannot exceed 8×10^{14} n/cm^{2}s.
- The activity of I-126 must not be so high as to impair the measurement of I-130. If an activity ratio 126/130 of less than 100 is tolerable, then the fast/thermal flux ratio must not exceed 1.1.

The characteristics of the reactors used in NBS measurements are plotted in the fast/thermal flux space in figure 1. The RT4 facility of the NBSR at 10 MW has been used for I-129 irradiations through August 1984. Since it is outside the useful region for measurement of I-127 through the (n,2n) reaction, a separate short irradiation has been used for stable I measurements through the 25-minute I-128 isotope.

BEST COPY AVAILABLE

The UVAR facility is marginal for measuring I-129 in the lowest-level samples, and nearly optimum for I-127. Other irradition facilities are also plotted on this graph, with data taken from Brauer et al (1) and and from other measurements at the NBSR. It is clear from this analysis that a heavy-water reactor like the NBSR is nearly ideal for I-129 measurements, and that an irradiation facility tailored and dedicated specifically for this task could bring dividends in the quality of iodine isotopic ratio measurements.

Future enhancements in sensitivity to the determination of I-129 by neutron activation analysis beyond the level presently attainable cannot be reached by adjusting irradition conditions, but will require more efficient counting procedures.

---

1. F. P. Brauer, R. S. Strebin, Jr., W. A. Mitlaff, and J. H. Kaye (1984), Irradiation and Gamma-Ray Spectrometric Parameters for I-129 Neutron Activation Analysis, In W. S. Lyon (ed): Analytical Spectroscopy (Anal. Chem. Sympos. Ser. 19). Amsterdam: Elsevier-North Holland.

NEUTRON-CAPTURE PROMPT-γ ACTIVATION ANALYSIS AND RELATED STUDIES

D. L. Anderson, G. E. Gordon, M. E. Kitto, L. McCarthy, and A. Bates
(University of Maryland, College Park, MD)

and

R. M. Lindstrom
(Center for Analytical Chemistry)

The increase in reactor power (to 20 MW) has doubled the thermal neutron beam flux (now 2.9 x 10^8 n/cm^2·s) at the prompt-γ activation analysis (PGAA) facility with no accompanying increase in elemental background interferences in terms of mg detected per irradiation for the elements H, B, C, N, Al, and Fe. This is of great benefit, as analysis times have been cut in half while retaining the original analytical quality (in terms of minimum detection limits).

In collaboration with Dr. Nathalie Valette-Silver of Carnegie Institute of Washington and Dr. Jody Deming of Johns Hopkins University, we are analyzing a large number of geological and biological samples from deep ocean region (13° North and 21° North, East Pacific Rise). With Dr. M. P. Failey of Battelle Columbus Laboratories, we have analyzed various samples related to processes in the oil industry. One of us (RML) is currently analyzing a number of steel samples for boron.

Much of our effort has been dedicated to developing a technique by which particles and gas-phase species in the atmosphere may be separately and

BEST COPY AVAILABLE

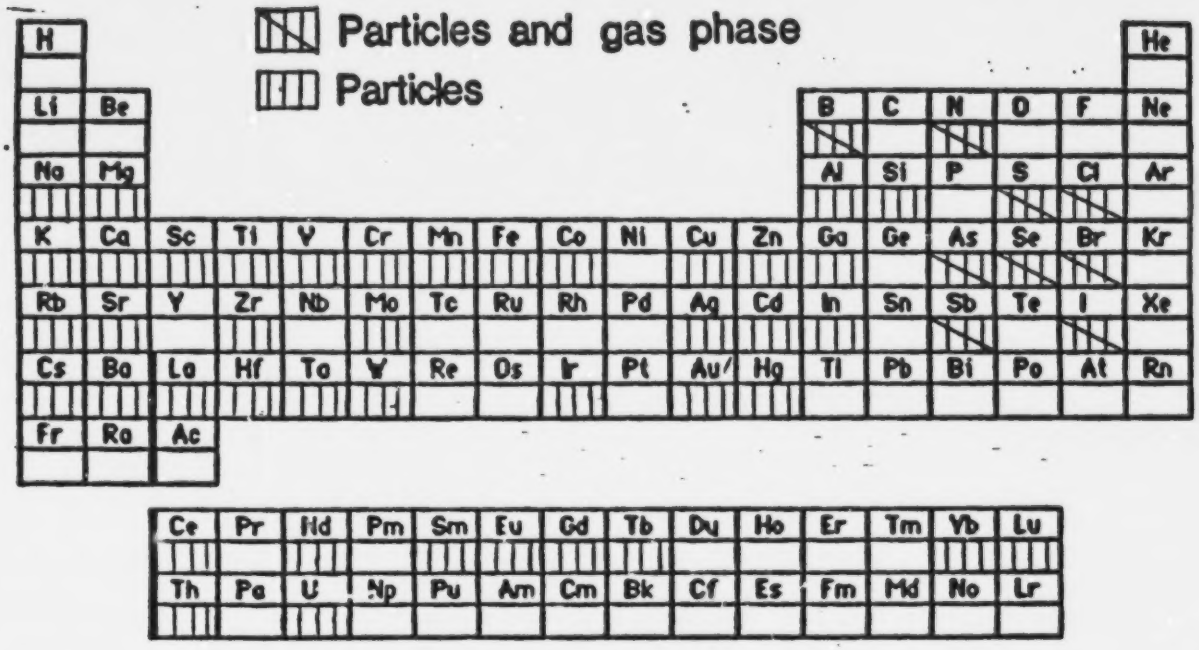

Figure 1. Elements Detected on Atmosheric Samples Using Multifilter Sampling Technique and INAA, PGAA, and IC.

simultaneously collected and their concentrations measured. Using a particle prefilter followed by ^{7}LiOH-treated and/or activated charcoal-doped cellulose filters and subjecting these to analysis by PGAA, instrumental neutron activation analysis (INAA) and ion chromatography (IC), we are able to determine concentrations of the elements shown in figure 1. In table 1, we present the minimum detection limits, an example of actual measurements, ^{7}LiOH-treated filter blank values, and minimum necessary volume data for the gas-phase elements detected by the combined techniques.

Boron (which can be readily detected by PGAA) is, we suspect, an especially important tracer element for large-scale coal-burning emissions, when detected away from oceanic influences. H_3BO_3 has a substantial gas-phase component in many areas, as seen in table 2. We are now trying to correlate gas-phase born with SO_2 emissions from coal-fired power plants and its subsequent transport and conversion to SO_4^{2-}.

Another possible tracer is Se, which may occur as SeO_2, elemental Se, or organic Se in the gas phase. We have some evidence of speciation, based on comparisons of our Se measurements (using base-treated filters) with those of Mosher

BEST COPY AVAILABLE

Table 1. Minimum detection limits by INAA, PGAA (P) and IC, and Whatman blank values (ng/110-mm filter).

Element	(keV)	(a)	(b)	x +/-	s	(d)
B (P)	472	1.80E-01	3.04E+01	6.65E+02	2.15E+02	11.5
NO3 (IC)	(e)	3.50E+01	1.00E+04	1.75E+04	2.10E+03	1.0
S	3104	6.46E+02	1.21E+04	8.00E+04	4.00E+04	5.0
S (P)	841	7.58E+02	1.40E+04	1.00E+05	5.00E+04	5.5
Cl	2168	1.35E+00	9.91E+02	3.24E+04	1.23E+04	22.5
Cl (P)	517	2.42E+01	1.10E+03	3.15E+04	3.10E+03	15.5
As	560	4.30E-03	2.20E-01	7.10E+00	3.00E-01	17.0
Se	264	1.22E-03	2.10E-01	3.53E+00	2.75E+00	15.0
Br	777	4.70E-03	5.30E+01	2.50E+02	7.07E+01	3.0
Sb	564	5.06E-04	4.20E-03	1.10E+00	3.60E-10	175.0
I	443	1.92E-01	1.61E+01	1.25E+02	6.01E+01	6.0

(a) based on a sample volume of 500 m3, not including blank

(b) College Park, MD sampling site, volume = 712 m3

(c) for 8 blank filter samples (ng/110-mm filter)

(d) volume necessary to observe elements 1 sigma above treated Whatman blank levels for measured sample

(e) based on Whatman blank levels and 500 m3 sample volume

Table 2. Ambient Particulate and Gas-Phase Boron Concentrations (ng/m^3) at Measured Several Locations.

Location	Particulate B	Gas-Phase B	Mean Gas/Particle Ratio	# Samples
Mauna Loa Observatory	0.2 ± 0.2	0.5 ± 0.3	2.5	3
Cape Kumukahi, HI	< 0.2	25 ± 11	125	2
Wallops Is., VA	2.9 ± 1.3	70 ± 52	24.1	12
College Park, MD	6.7 ± 0.3	9.5 ± 0.5	3.7	1
Gaithersburg, MD	2.6 ± 0.3	9.5 ± 0.5	3.7	1
Fairbanks, AK	12.2 ± 4.6	0.5 ± 0.4	0.04	4

BEST COPY AVAILABLE

Table 3. Comparison of Measured Se Values: Base-treated vs. Activated Charcoal Filters.

Location	Se Concentration (ng/m3) gas	particles	Range (ng/m3) gas	particles	# of meas.
URBAN					
Providence, RI	(a) 0.41 ± 0.18	1.26 ± 0.36	0.21 - 0.47	0.93 - 1.65	3
College Park, MD	(b) 0.14 ± 0.11	2.05 ± 1.09	0.019 - 0.45	0.37 - 4.45	23
Gaithersburg, MD	(b) 0.13 ± 0.06	1.40 ± 0.25	0.07, 0.19	1.14, 1.65	2
RURAL					
Narragansett, RI	(a) 0.25 ± 0.16	0.93 ± 0.59	0.07 - 0.60	0.25 - 1.97	17
Wallops Is., VA	(b) 0.080 ± 0.050	1.76 ± 0.95	0.032 - 0.32	0.74 - 3.66	12
REMOTE MARINE					
Oahu, HI	(a) 0.035 ± 0.014	0.14 ± 0.03	0.020 - 0.053	0.13 - 0.18	4
Cape Kumukahi, HI	(b) 0.016 ± 0.004	0.13 ± 0.04	0.013, 0.020	0.088, 0.165	2

(a) Activated Charcoal Filters (Mosher and Duce)
(b) 7LiOH Treated Whatman 41

and Duce of the University of Rhode Island (who used charcoal-doped filters) at similar locations (see table 3). While local or temporal variations may be responsible for the factor of 3 difference in the measurements, we are now doing side-by-side sampling using both types of filters to see if the differences are due to the presence of both acidic gas-phase Se species and elemental and organic Se species. Many other potential gas-phase elemental tracers (e.g. As, Sb, and I are also under investigation.

BEST COPY AVAILABLE

NON-RRD PROGRAMS

IAEA COORDINATED RESEARCH PROGRAM ON HUMAN DAILY DIETARY INTAKES OF NUTRITIONALLY IMPORTANT TRACE ELEMENTS

V. Iyengar and R. Zeisler
(Center for Analytical Chemistry)

and

J. T. Tanner
(U.S. Food and Drug Administration, Washington, DC)

and

W. Wolf
(USDA Human Nutrition Research Center, Beltsville, MD)

The IAEA international study is a comprehensive project aimed at obtaining comparable data on dietary intakes of 23 nutritionally important minor and trace elements through diets consumed in a variety of developed and developing countries. The project also involves estimating phytate and energy content of the diet. The scope of the study, which includes contribution to the core program as well as allowing for supplementary research, provides an unique opportunity to develop a coordinated approach by collaborators of the 3 participating agencies, the FDA, the NBS and the USDA.

The combined expertise of the participants will be aimed towards a significant improvement and development of analytical methodology needed for the accurate assessment of the dietary intakes of trace elements. Aspects of quality assurance in sampling, sample preparation, analysis and data evaluation will be treated. In addition, long term monitoring will be addressed by storing part of the samples in a specimen bank.

As part of the first year work plan drawn up for the joint FDA-IAEA-NBS-USDA project, precision and accuracy aspects related to Flame Atomic Absorption Spectrophotometry (AAS-Flame), Atomic Emission Spectro-photometry with an Inductively Coupled Plasma source (AES-ICP) and Neutron Activation Analysis (NAA) were evaluated by analysing the same test samples by all the three methods. As a first step, investigation of the elemental compostions of available dietary reference materials was taken up. The materials considered were IAEA Mixed Diet (IAEA-H9), USDA Mixed Diet (USDA TDD-1D), NBS Rice Flour (NBS-1568 and NBS-1568a) and NBS Wheat Flour (NBS-1567a). Basically, a set of 23 elements of biological significance was sought in all the samples as envisaged in the project protocol. These were As, Ca, Cd, Cl, Cr, Cu, F, Fe, Hg, I, K, Mg, Mn, Mo, Na, Ni, P, Pb, Se, Si, Sn, V and n. Depending upon the capabilities of the technique, additional data on other elements, were also Cr, Cu, F, Fe, Hg, I, K, Mg, Mn, Mo, Na, Ni, P, Pb, Se, Si, Sn, V and n. Depending upon the capabilities of the technique, additional data on other elements, were also gathered.

BEST COPY AVAILABLE

DETERMINATION OF GOLD AND PLATINUM IN HUMAN URINE, SRM 2670

Robert R. Greenberg and Rolf Zeisler
(Center for Analytical Chemistry)

There is continuing concern about the possible impact of platinum on the biosphere due to the increasing industrial and medical uses of this metal. Approximately 18700 kg (600,000 troy ounces) of platinum are used annually by the automotive industry, while theraputic utilization of platinum compounds for their anti-cancer properties is increasing. Due to this expanding use of platinum it is important to be able to measure platinum at the naturally occurring levels.

Accurate determination of gold and platinum at concentrations below 1 ng/g is extremely difficult and requires rigid control of the blank. Radiochemical neutron activation analysis (RNAA) provides an ideal method to determine these elements in that it can be performed in an almost blank-free manner. After irradiation, but before chemical manipulation of the samples, unirradiated carriers of the elements of interest can be added to minimize losses which typically occur when processing extremely dilute solutions of the noble metals. Several years ago a procedure was developed to determine both gold and platinum in biological materials via RNAA (1). This procedure has been modified to allow the determination of these metals in both the elevated and the natural level fractions of the Trace Elements in Urine Standard Reference Material (SRM 2670). Urine is a difficult matrix for NAA for two reasons. First, the high salt level in urine produces a large amount a background radiation which must be removed prior to gamma-ray spectroscopy, and second, a liquid is considerably more difficult to irradiate than is a solid, and often requires a pretreatment step, such as lyphilization, which can increase the blank.

Elevated Level Samples - The entire contents of each of five bottles of Urine was dissolved in 5 mL of ultrapure water and transferred to an LPE (polyethylene) bag which had repeatedly been washed in a mixture of NBS subboiling distilled nitric and hydrochloric acids. The samples were than lyophilized, sealed, and placed in a second acid washed LPE bag. The samples were irradiated with Au and Pt standards for 36 s in RT-3. Midway through the irradiation the rabbit was removed from the reactor, flipped end-over-end, and reinserted into the reactor to insure a uniform neutron fluence throughout the rabbit. Approximately 1 day after irradiation the outer bag from each sample was discarded and the inner bag containing the sample was opened. The opened bags were transferred to 400 mL beakers along with 85 mg of Au carrier, 50 mL of water, 25 mL of nitric acid, and 25 mL of hydrochloric acid. The

BEST COPY AVAILABLE

bags were allowed to sit in this solution for at least two hours and the solutions were occasionally stirred to dissolve all material. The bags were then washed with water and this was added to the appropriate beaker. Finally each bag was allowed to sit in 100 mL of 8 mol/L sulfuric acid for 3 hours after which the bags were discarded and the sulfuric acid solutions were added to the appropriate solutions. Since chemical yields were determined, a quantitative transfer of material was not necessary as long as equilibration between sample and carrier was achieved. An additional 100 mL of water was added to each sample and the samples were heated overnight at low heat. The next morning the heat level was increased and the remaining water, nitric acid and hydrochloric acid were allowed to evaporate. The heat level was then slowly increased until the temperature of the solutions was just below the boiling point of sulfuric acid. The solutions were covered with watch glasses and were heated at this temperature until all the metallic Au had precipitated. The separated Au samples were sequentially washed in water, nitric acid, water, hydrofluoric acid, water, hydrochloric acid and finally water. The samples were then heated to 500°C to ensure that all sulfuric acid was removed, and were then cooled, weighed to determine chemical yield, transferred to polyethylene bags, and counted on a gamma spectrometer with Compton suppression. Gold was determined via the Au-198 isotope and Pt was determined via the Au-199 daughter of Pt-199. The second order Au interference is Pt was extrapolated from Au standards irradiated for 1 h in Rt-3. Since this second order interference is proportional to neutron fluence squared, while the production of Au-199 from Pt-198 is proportional to neutron fluence (for irradiation times short compared to the half life of Au-199), the interference for the 36 s irradiation was 1% of the interference for the 1 hour irradiation. The magnitude of the interference correction for the elevated urine was 3% of the total Pt concentration and the additional uncertainty from this interference correction was approximately 0.3% of the Pt concentration in the elevated urine.

Normal Level Samples - The procedure was essentially the same as for the Elevated Urine samples except that the samples were individually irradiated for 1 hour in RT-3. Three such samples were analyzed as well as a blank sample of ultrapure water processed the same way as the samples. The magnitude of the Au interference for Pt was approximately equal to 50% of the uncorrected Pt concentration and the additional uncertainty due to this correction was 10% of the Pt concentration.

BEST COPY AVAILABLE

Table 1. Concentrations (ng/mL) Observed in Elevated Level Samples of Urine, SRM 2760:

Sample	Au	Pt
1	242.0 ± 0.7[a]	122.9 ± 2.5[a]
2	244.7 ± 0.7	126.0 ± 2.3
3	247.7 ± 0.7	125.5 + 2.7
4	241.4 ± 0.7	122.5 ± 3.4
5	246.1 ± 0.7	128.4 ± 3.8
Mean ± 1s	244.4 ± 2.7	125.1 ± 2.4
Estimated 95% Confidence Interval	± 8.2	± 8.0

[a]Uncertainties are 1 σ counting statistics of sample and standards.

Table 2. Concentrations (pg/mL) Observed in Normal Level Samples of Urine, SRM 2670

1	8.0 ± 0.1[a]	8.5 ± 1.1[a]
2	8.5 ± 0.1	8.3 ± 1.9
3[b]	7.5 ± 0.1	7.2 ± 2.3
Mean ± 1s	8.0 ± 0.5	8.0 ± 0.7
Estimated 95% Conference Interval	± 1.4	± 2.7
Blank	- 0.1	- 0.2

[a]Uncertainties for individual measurements are 1 σ counting statistics of sample and standards

[b]This sample contains 2 bags (double blank).

The results of these analyses are listed in table 1 and 2; the concentrations listed are for the specified dilution of the contents of each bottle of Freeze-Dried Urine to 20.0 mL. Uncertainties for individual measurements are 1 sigma combined counting statistics for sample and standards. The estimated 95% confidence intervals for the results are also listed in these tables. The confidence intervals were calculated by combining the standard deviation of the mean for each set of values muiltiplied by the appropriate t-value for the 95% confidence level and than adding the estimated systematic error. For the Au measurements in both the elevated and normal level urine samples the estimated systematic error was 2% which was due mainly to potential counting geometry errors since the samples were counted directly on top of the detector. For the Pt in the elevated urine the estimated systematic error was 4%: 2% from counting geometry and an additional 2% from possible bias in peak

BEST COPY AVAILABLE

integration of the 158 keV peak of Au-199 which lies directly upon the backscatter peak of Au-198. For the Pt in the normal urine the estimated systematic error was 12% (2% from counting geometry and 10% from the determination of the Au interference; this 10% error also includes the bias from peak integration so that an additional 2% was not included).

The observed sample standard deviation (1s) for Au in the elevated fraction of the Freeze-Dried urine (1.1%, relative) was slightly greater than expected from counting statistics. This excess variance was probably due to counting geometry errors (discussed above). The observed sample standard deviation for Au in the normal fraction of the Freeze-Dried Urine was significantly greater than the counting statistics. This may have been due to variable losses of Au onto the walls of glass bottles (prior to lyophilization) that this SRM was packaged in.

With an appropriate separation procedure, RNAA can be used to determine the concentrations of gold and platinum in biological samples at the picogram per gram level. Both solid and liquid samples can be submitted for analysis, however a lyophilization step prior to irradiation may be advantageous.

---

1. Zeisler, R. and Greenberg, R. R., "Ultratrace Determination of Platinum in Biological Materials via Neutron Activation Analysis and Radiochemical Separation," J. Radioanal. Chem. 75, 27 (1982).

MULTIELEMENT ANALYSIS OF BIOLOGICAL MACROMOLECULES

Susan F. Stone, Rolf Zeisler and Diane Hancock

The importance of the role of trace elements associated with biological macromolecules has become increasingly apparent in the last twenty years. For example, studies of metalloproteins has revealed the structural and functional importance of certain trace metals associated with proteins. The biological specificity of metalloenzymes depends on the presence of both the protein and the metal ion. Removal of the metal ion results in a loss of biological activity. Trace metals have also been found to be structurally important in stabilizing secondary, tertiary, or quarternary protein structures. Detection of trace elements associated with proteins may be accomplished with a newly-developed combination of biological separation techniques with analytical nuclear methods.

Polyacrylamide gel electorphoresis (PAGE) separation of proteins by molecular weight is one technique that we have used. Several proteins were separated by

BEST COPY AVAILABLE

Analysis of Gel Reagents

	Cr	Fe	Co	Zn
Acrylamide				
10% gel	230ng	10µg	54ng	360ng
20% gel	480	22µg	120ng	760ng
Bis-acrylamide				
10% 20% gel	6.7ng/14ng	540ng/1110ng	1.45ng/3.00ng	29ng/60ng
Tris base				
Trizma	57ng/44ng	2.3µg/1.8µg	20ng/15ng	94ng/72ng
Ultrol	140ng/11ng	22µg/17µg	66ng/51ng	720ng/560ng
Tris HCl				
Calbiochem	190ng/150ng		19.8ng/15.1ng	
Sigma	52ng/40ng		40ng/30ng	138ng/105ng
SDS				
Lot D	47ng/39ng			
Lot P	17ng/14ng			
NH4 Persulfate	42ng/14ng	270ng/90ng	2.2µg/0.7µg	14ng/5ng
Glycine				
(in 13L buffer)	3.4µg		561ng	
SDS				
(in 13L buffer)	2.4µg			
Tris base (Trizma)				
(in 13L buffer)	0.20µg	8.3µ	70ng	0.33µg
Per gel(worst case)				
10% part	0.66µg	33µg	0.16µg	1.26µg
20% part	0.81µg	40µg	0.20µg	1.49µg
Total (ng/cm^2)	$5.8ng/cm^2$	$290ng/cm^2$	$1.4ng/cm^2$	$11ng/cm^2$

electrophoresis on a 10-20% gradient polyacrylamide gel. A whole gel was then irradiated with neutrons, and following a short decay time, an autoradiograph was developed to detect any beta-emitting isotopes of fairly high energy that were produced. The location of phosphorous-associated protein, phosvitin, was visualized in this way as shown in figure 1(b). P-32 was the isotope detected in the autoradiograph. This technique shows a much more sensitive threshold of phosphorous detection than does a non-specific protein stain, such as a Coomassie Blue stain. A duplicate gel treated with Coomassie Blue is shown in figure 1 as an overlay of the autoradiographed gel. The protein bands visualized by the stain are carbonic anhydrase (a) and serum (c). The gel location corresponding to the phosvitin band is not visible with the Coomassie Blue stain.

BEST COPY AVAILABLE

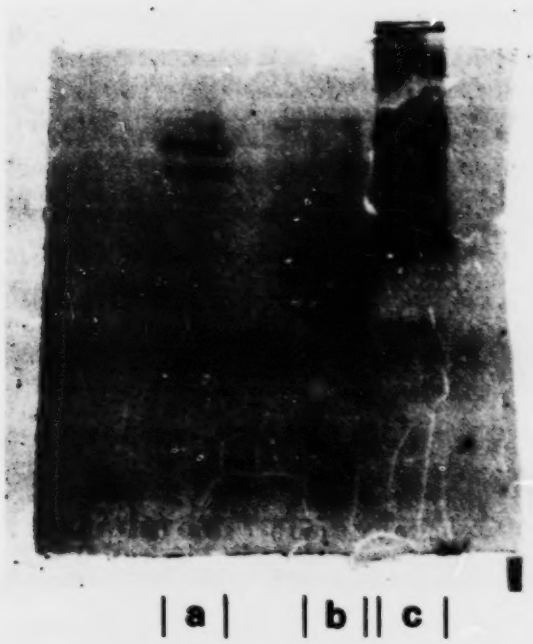

Figure 1. Comparison of protein bands, separated by PAGE, using two detection techniques. One gel shows the phosvitin (strip b) using autoradiography of P-32. A duplicate gel, stained with Coomassie Blue dye, has been placed over the autoradiograph, matching the protein band locations. The stained gel shows cabonic anhydrase (strip a), and serum (strip c), but no phosvitin.

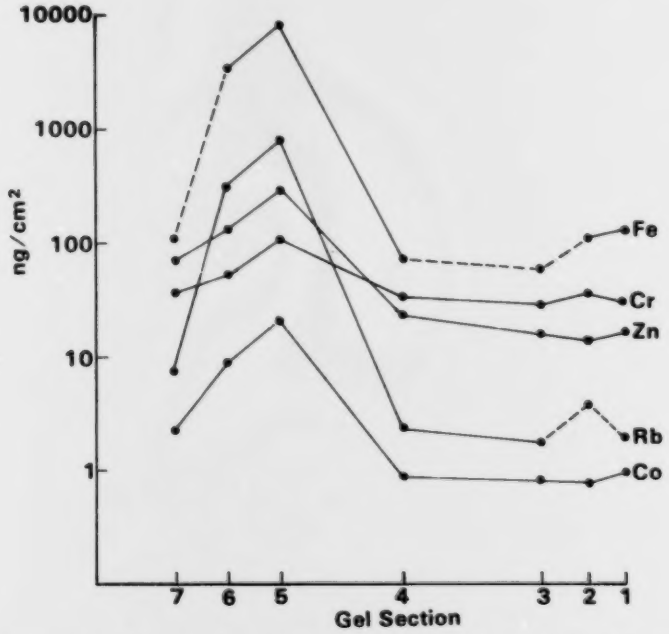

Figure 2. Comparison of five trace element concentrations in a PAGE separation of carbonic anhydrase. Protein bands were included in gel sections 3 and 5, while the other gel sections represent background.

BEST COPY AVAILABLE

In addition to autoradiography, gamma-counting has also been done for separated metalloproteins using neutron activation analysis. Protein electrophoresis is normally done using a detergent, sodium dodecyl sulfate (SDS), which is a denaturing agent. An electrophoretic separation of carbonic anhydrase was done using SDS, and trace element analysis of gel sections was performed. Results for five elements are shown in figure 2. A marked increase in zinc, which is associated with enzyme, was found in the protein band (gel section 5), compared to the background, as expected. However, many other trace elements, which have no known association with the enzyme, increased as well. In addition, the zinc concentration found in the protein band was more than should have been present from the amount of protein applied. Studies are currently in progress to learn more about trace element associations with proteins under both denatured and non-denatured conditions.

Calculations showed that the actual zinc concentration in a protein band would not be easily discernible above existing background concentrations. This finding initiated research to reduce the trace element background in the polyacrylamide gels. Table 1 lists some of the results from an analysis of reagents used in the preparation of polyacrylamide gels. Rubidium is not listed because only upper limit concentrations were obtained (at 1ng/cm2). Using worst case approximations, the concentrations (ng/cm2) for zinc, rubidium, and cobalt do not completely account for the trace element background concentrations found under denaturing conditions. Research is continuing for the reduction of trace element background.

BEST COPY AVAILABLE

DEVELOPMENT OF BIOMONITORING SPECIMEN BANK IN THE UNITED STATES

Stephen A. Wise and Rolf Zeisler
(Center for Analytical Chemistry)

Since 1975 the National Bureau of Standards, in conjunction with the U.S. Environmental Protection Agency (EPA), have been involved in the development of methods and procedures for environmental specimen banking. In 1975 the Federal Republic of Germany and the U.S. agreed to cooperate in the study of environmental specimen banking activities and proposed the establishment of "Pilot Phase" specimen banks in both countries. An EPA-NBS workshop in 1976 recommended the establishment of a pilot environmental specimen banking program to evaluate the feasibility of a National Environmental Specimen Bank (NESB) by providing working experience in all aspects of specimen banking, that is, in specimen collection, processing, storage, and analysis. The goals of this pilot phase were:

1. to develop procedures for the sampling, processing, storage, and analysis of four types of environmental accumulators:
    a. human soft tissue,
    b. a marine accumulator,
    c. a food accumulator, and
    d. an air pollutant accumulator;
2. to evaluate and improve analytical methods for the determination of trace element and organic pollutants in biological matrices;
3. to evaluate the feasibility of long-term storage of environmental samples under various conditions;
4. to establish baseline data on selected environmental samples, and;
5. to evaluate specimen banking as a means of storing samples for trend monitoring and of permitting retrospective analyses as concerns about new pollutants arise and as new analytical techniques are developed.

Since 1980 the EPA-NBS pilot environmental specimen bank has been involved in the collection, processing, storage, and analysis of the first sample type, human liver tissue. However, because of funding limitations, the remaining three samples types (i.e., marine, food and air accumulators) were not incorporated fully into the pilot banking program as originally designed. During the past year the specimen banking concept at NBS has been modified based on current funding levels from EPA and

BEST COPY AVAILABLE

the interest of other agencies in specimen banking activities.

1. Project Phase

a. Existing Projects

1. EPA Specimen Bank Program

As the "pilot phase" (1980-1985) nears completion, the program will move towards a "project phase" of the Biomonitoring Specimen Bank Research Project. At present there are two existing specimen banking projects and several proposed projets to be funded in FY 86.

The EPA-NBS Specimen Bank Program will continue to serve as the focal point for related activities during the project phase. During the next year the activities of the EPA-NBS project will be directed towards the following milestones:

a. Continued collection of human liver specimen (~50/year);
b. Analysis of 30 liver specimens from 1984 set;
c. Verification of sample stability through reanalysis of specimens from 1980 and 1982 collections;
d. Trend monitoring, e.g., Pb (1980-1985), and;
e. Analytical quality assurance.

2. NOAA National Status and Trends Program

In 1985 a specimen banking project was initiated at NBS with the National Oceanic and Atmospheric Administration (NOAA) as part of their National Status and Trends (NS&T) Program to monitor the U.S. marine environment. The NS&T program consists of two monitoring programs, the Benthic Surveillance Program, in which sediment and fish tissue (muscle and liver) will be collected from approximately 50 coastal sites, and the Mussel Watch Program, in which mussels and sediment will be collected from approximately 150 coastal sites. As part of the NOAA NS&T program, NBS will provide the following specimen banking activities:

a. Development of sampling protocols for the collection of sediment, mussels, fish muscle, and fish liver;
b. Bank specimens of sediment and tissue from 12 sites of the Benthic Surveillance Program and mussels and sediment from 30 sites in the Mussel Watch Program;
c. Analyze six different specimens of mussels and sediment for the determination of selected trace elements (15 elements) and organics (organochlorine pesticides, PCBs, and PAH), and;
d. Analyze four reference materials for quality assurance.

BEST COPY AVAILABLE

3. IAEA/FDA/USDA/NBS Nutrients in Human Diet Program

NBS, Food and Drug Administration (FDA), and the Department of Agriculture (USDA) are collaborating in a project sponsored by the International Atomic Energy Agency (IAEA) to obtain comparative data on the dietary intakes of 23 nutritionally important minor and trace elements in a number of developing and developed countries. The combined expertise of the various agencies is directed towards the development and improvement of analytical methodology for the accurate assessment of dietary intakes of trace elements. As part of this interagency collaboration, several tasks related to specimen banking will be included:

a. Methods development, analyses, and quality assurance.
b. Intercomparison of analytical methods for trace elements in existing dietary reference materials.
c. Preparation of U.S. mixed diet research material from the 200 different food groups in the FDA Total Diet Study (~10 kg).
d. Determination of long-term stability of trace constituents in the total diet composite.
e. Bank aliquots of the total diet sample.

Future collections of total diet specimens will be made in four different geographical regions of the U.S. Representative portions of these total diet composites will become part of the Biomonitoring Specimen Bank.

b. Proposed Projects

Several additional projects will start in FY 86 which will broaden the scope of the specimen bank program to include projects related to nutrient as well as pollutant determination in biological matrices.

1. NCI Nutrients in Human Serum

As part of a three-year quality assurance program of the National Cancer Institute (NCI), NBS is developing analytical methods for the determination of nutrients in human serum. One aspect of this program will be the determination of the long-term stability of selected nutrients in serum (frozen and lyophilized). The following analytes will be studied:--zinc, selenium, beta-carotene, retinol, alpha-tocopherol, retinyl palmitate, retinyl acetate, and ascorbic acid.

2. Human Liver Standard Reference Material

As a result of the past five years of experience in the analysis of human liver samples as part of the EPA-NBS pilot banking program, NBS will prepare and certify a human liver Standard Reference Material (SRM). This SRM will be useful to laboratories involved in the measurement of trace elements in human tissue, since the

BEST COPY AVAILABLE

concentration levels of several elements of environmental (e.g., Pb) and nutritional (e.g., Se) interest are considerably lower in human liver as compared to the existing bovine liver SRM. In addition, the human liver SRM will be prepared using the contamination minimizing homogenization techniques developed in the specimen banking program. In addition to the certified values for the trace element concentrations, information values for several organochlorine pesticide residues will be provided.

3. EPA Human Adipose Tissue Monitoring Program

Since the mid-1960's, EPA has conducted a monitoring Program to measure organochlorine pesticides and PCB's in human adipose tissue. At present adipose tissue samples are collected from approximately 1000 sites across the U.S. Portions of the tissue specimens have been stored if excess material was available after analyses. Recently, this tissue monitoring program has expanded their analytical procedures to include volatile organics as well as the semi-volatile compounds measured in the past. EPA has expressed interest in including NBS in this program to serve a quality assurance and specimen banking role. NBS would store a small number of specimens from the program to serve as reference samples and to investigate storage stability. A number of these samples would be analyzed at NBS to provide method validation and baseline data.

2. Network Phase

The project phase will provide experience in the sampling, processing, storage and analysis of a variety of biological matrices as originally intended for the pilot program (e.g., human tissue and fluids--liver, adipose, and serum; marine accumulator--mussels, fish, and sediment; and food accumulator--total diet samples). The project phase will also bring together the different government agencies responsible for both contaminants and nutrients in these various matrices to coordinate their efforts in specimen banking. The result will be the establishment of a National Biomonitoring Specimen Bank System consisting of a network of satellite banks derived from the project phase as illustrated in figure 1. NBS will serve as resource facility to conduct research related to the needs for specimen banking and as a quality assurance laboratory for the analytical measurements required in the various satellite banking programs.

BEST COPY AVAILABLE

FACILITIES AND EQUIPMENT FOR ACTIVATION ANALYSIS

Richard M. Lindstrom and John K. Langland
(Center for Analytical Chemistry)

A new VAX 11/730 computer (in the minisupermini class) has been added to the Group's counting systems. With a 120-megabyte disk and a much more powerful operating system than the PDP 11/44 which it replaces, the mechanism is in place for development of an optimimum mixture of distributed processing (for data acquisition, text processing, and interactive data analysis) and centralized computation (for database management, NAA data reduction, and numerical simulation).

A new computer-based data acquisition and processing system (Nuclear Data 6700) to operate in parallel to the existing system, a display and acquisition minicomputer (DEC Pro-380) to act as a buffer for the ADCAM systems, and a general-purpose microcomputer (Zenith Z100) for communication and reporting have all been acquired in the past year.

Links have been established among almost all counting and computing systems in the Group (figure 1). Already it is possible to interchange spectral data files among all the Nuclear Data MCAs, and text files among all computers, allowing users to choose the most suitable device for the application.

A 30-Mb Winchester disk drive has been added to the ND6620 system. This drive includes a 1-Mb flexible disk by which data may be transferred to or from the

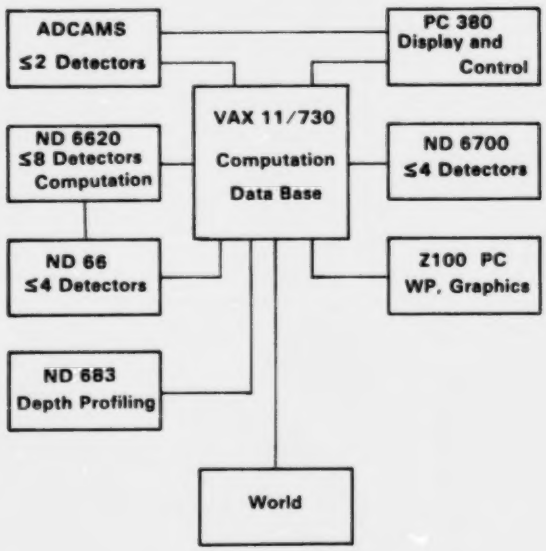

Figure 1. Nuclear Methods Group data acquisition and computation system.

BEST COPY AVAILABLE

identical drive in the 6700 system. The redundancy now available with these serial links and removable disks makes diagnosis of hardware and software problems much more easy.

A prototype rabbit receiver has been built and is installed in room B-121 connected to RT-5, for testing. This receiver provides improved operator safety in that it is remotely operated via an electro/phenumatic control system. Rabbits may be fired into the reactor, returned, flipped, sent to storage, or dropped into a transport pig without any radiation exposure to the operator.

Another automatic sample changer has been added to the group's equipment. This Smithsonian owned changer works with the Smithsonian's ND-66 M.C.A. and the groups DEC-VAX computer. It is currently set up with an Ortec gem series germanium detector. It holds up to fifty samples, mounted in saml glass test tubes, which may be stationary or rotating during counting. The sample to detector distance is variable from contact to 50 centimeters.

ATMOSPHERIC AND ENVIRONMENTAL STUDIES BY INSTRUMENTAL NEUTRON ACTIVATION ANALYSIS

G. E. Gordon and W. H. Zoller
(University of Maryland, College Park, MD)

We continue to make extensive use of instrumental neutron activation analysis (INAA) to determine concentrations of about 35 elements in samples of atmospheric particulate matter collected from ambient air (now mostly at remote sites such as Hawaii and rural sites in the continental U.S.) and in particles released from major sources such as power plants. By measuring concentrations of such large number of elements, we are able to identiy contributions from the sources to the atmospheric burden at ambient sampling sites. Examples of some of these studies are discussed briefly in the following sections. Because of the shutdown of the reactor for much of the past year, we focused more of our effort on interpretation and write-up of results from analyses performed in previous years. Now that the reactor is again functioning, we are using it extensively for analyzing samples collected before and during the hiatus.

1. Rare Earth Elements on Particles Released by Oil Refineries and Power Plants

Based on the results of analyses of many types of samples analyzed by INAA at the NBS reactor, ranging from source samples collected in Philadelphia to Asian dust samples collected at Mauna Loa Observatory (MLO) in Hawaii, plus the use of

BEST COPY AVAILABLE

literature data from other groups, we have found that (a) fluid catalytic converters of oil refineries and, to a lesser extent, oil-fired power plants release fine particles containing high concentrations of rare earth elements (REE) to the atmosphere and (b) the pattern of REE released is different from that of the Earth's crustal abundance pattern, being more enriched in the light REE, especially La. Regarding the latter point the La/Sm ratio for typical crustal material is about 5, whereas the ration for particles from oil-fired plants and refineries is typically in the 20 to 40 range. It appears that the source of the REE released by these plants is ziolite catalyst used to "crack" large molecules present in raw petroleum. The catalysts typically contain 1-3% mixed REE oxides. The unusual REE pattern is typical of the major U.S. ore of REEs, bastnasite.

The large amount of REEs released on fine particles from these sources provides an excellent signature for tracing their emissions over long distances. In the most spectacular demonstration of the potential use of this "tracer of opportunity", we think that REEs observed at certain times at MLO in Hawaii originate from the oil industry in Japan and elsewhere in Asia, representing a travel distance of about 6000 km! One important aspect of this problem is the fact that the tracer is normally observable only when samples have been analyzed by INAA, as no other commonly used method has the necessary sensitivity for REEs.

A paper describing this work in more detail has been accepted by Science.[1] M. Kitto, D. L. Anderson and I. Olmez are presently analyzing samples of about a dozen catalysts used in the oil industry. Both INAA and PGAA (see Anderson et al. section) are being used.

2. Compositions of Atmospheric Particles at Mauna Loa Observatory, Hawaii

Until recently, there existed no long continuous record of concentrations of elements on particles at a site remote from local activities despite demonstration of the enormous value of the long-term CO^2 seasonal variations and long term increase. Fortunately, since mid-1979, the National Oceanic and Atmospheric Agency (NOAA) has supported weekly collections of filters at MLO and analysis of them by our group using INAA. Results of analysis of the MLO samples through 1982 were discussed in last year's Progress Report. Since Jan. 1983, we have continued to collect samples on a weekly basis, but analysis of the samples was interrupted because of eruptions from Kilauea and Mauna Loa volcanoes off and on since that time. As discussed below, we have instead analyzed samples of the volcanic material. Recently, we have again begun to analyze MLO samples taken since Jan. 1983.

BEST COPY AVAILABLE

3. Composition of Emissions from Volcanoes

To interpret compositions of particles collected at MLO and other remote sites, we must know compositions of particles released by various natural source is volcanic emissions, which have been heavily investigated by this group for several years. This year we have focused attention on the Hawaiin volcanoes, Kilauea and Mauna Loa.

Kilauea erupted in Jan. 1983 and has continued to erupt at various times since then. Emissions from the initial eruptivie phase were inadvertently collected at the MLO sampling station (see Sect. 2) and analyzed by INAA at the NBS reactor, revealing unusually large concentrations of Se, As, In, Au, and S, as expected for volcanic emissions. In a paper published in Science Zoller et al.[2] noted that strikingly large concentrations of Ir were also observed. As Ir enrichments have not previously been observed in volcanic emissions, the results suggest that Kilauea is part of an unusual volcanic system which may be fed by magmas from the earth's mantle. The Ir enrichment appears to be linked with the high F content of the volcanic gases, suggesting its release as IrF_6. Previous workers[3] observed huge Ir enrichments at the Cretaceous-Tertiary (K-T) boundary layer in sediments, which they suggest arose from the impact of a very large meteorite. The results obtained from Kilauea suggest that volcanic emissions of this type might provide an alternate explanation.

Samples were subsequently taken much closer to the volcano to obtain much greater masses of volcanic material and analyzed these samples at the NBS and Los Alamos reactors. The results confirm and extend the results obtained from the MLO samples. A paper concerning these results has been submitted for publication.[4]

Mauna Loa volcano began erupting on 24 March 1984. Members of our group began collecting samples on 27 March and continued sampling, both with airplanes and on the ground until 15 April. The samples are being analyzed by INAA at the NBS and Los Alamos Reactors.

4. South Pole Aerosol

As a part of the study of particles in global circulation, particles have been collected from the very pristine atmosphere of the South Pole since 1971 (e.g. Ref. 5). During the past year, G. Tuncel completed analysis of the samples collected there since 1977. Results for some of the elements observed were given in last year's Progress Report.

Most analyses of South Pole samples were done by INAA. However, chemical separations were used on some South Pole samples to observe Ir, which is present in extremely small concentrations, typically 10^{-4} pg/m^3 of air. On the basis of concentrations of several metals at the South Pole, Cunningham and Zoller[5] estimated the total influx of meteoritic material to the earth's atmosphere. However, Ir is a

BEST COPY AVAILABLE

much more sensitive indicator of meteoritic material than most other metals. The estimated yearly infall rate of extra-terrestrial material based on Tuncel's Ir measurements is 27,000 tons/yr, which is in the range of estimates based on a wide range of other methods. Because the South Pole atmosphere receives very small inputs of material from terrestrial sources, even the minute amounts of material from extra-terrestrial sources can account for non-negligible fractions of the observed concentrations of several elements, especially 4% of the Mn, 6% of Fe and 12% of Co.

The work is included in the thesis of G. Tuncel[6] and is being prepared for submission to journals.

5. Composition of Particles from Polluted Cities

The Asia dust transported to MLO in Hawaii in large amounts each spring (see Sect. 1) often has composition quite unlike that of soils from other parts of the world (e.g. high concentraion of Ag). We now have evidence that the dust, which originates from dust storms in China, picks up contaminants as it passes over the populated and industrial areas of Asia. As a start to identifying sources of these contaminants, we obtained fifteen air filter samples collected in Beijing, China by T. Novakova's group in Berkeley and previously analyzed by x-ray fluorescence (XRF) by them. D. Hermann and Ilhan Olmez subjected them to INAA to obtain data for additional elements.

Results for a number of elements are listed in Table 1 where, for comparason, we have listed concentrations of the same elements in the Washington, D.C. area obtained from previous studies by our group that involved use of the NBS reactor.[7] Beijing has one of the highest particulate loadings of any city in the world. For many elements, the average concentrations are about an order-of-magnitude greater than in Washington, D.C. These very high concentrations are caused mainly be two sources. First, during the Spring season, when the Beijing samples were collected, huge dust storms to the west of Beijing bring great masses of airborne dust to the city and beyond to the Pacific. Second, most cooking and heating is done with coal with essentially no pollution controls. Both sources contribute strongly to the atmospheric concentrations of many crustal elements: Al, K, Ca, Sc, Ti, Mn, Fe, Co, Ba, La and Sm. Coal is enriched in a number of trace elements, which are preferentially released to the air (relative to lithophile elements, which mostly remain in the ash), accounting for the high concentrations of Zn, As, Se and Sb. Although coal combustion is a major source of airborne sulfate in the U.S., the S concentration is not much greater in Beijing than in Washington. There are at least reasons for this. First, the Washington samples were collected in late summer, when conversion rates of SO_2 released hundreds of km upwind and slowly converted to

BEST COPY AVAILABLE

Table 1. Comparisons of Particle-Borne Atmospheric Concentrations in Beijing, PRC and Washington, DC area.[a]

Element	Concentration	Beiging	Washington, D.C.
Na	$\mu g/m^3$	2.0 ± 0.2	0.30 ± 02
Al	$\mu g/m^3$	12 ± 0.9	1.35 ± 0.11
S	$\mu g/m^3$	5.2 ± 0.7	3.2 ± 0.4
K	$\mu g/m^3$	6.9 ± 1.8	0.40 ± 0.02
Ca	$\mu g/m^3$	15 ± 1.5	0.86 ± 0.04
Sc	ng/m^3	3.4 ± 0.34	0.33 ± 0.03
Ti	$\mu g/m^3$	1.1 ± 0.09	0.11 ± 0.01
V	ng/m^3	20 ± 7	25 ± 2
Cr	ng/m^3	70 ± 8	14 ± 2
Mn	ng/m^3	270 ± 25	26 ± 3
Fe	$\mu g/m^3$	6.7 ± 0.6	1.0 ± 0.06
Co	ng/m^3	7.3 ± 1.0	0.83 ± 0.08
Ni	ng/m^3	29 ± 4	17 ± 2
Cu	ng/m^3	48 ± 19	17 ± 2
Zn	ng/m^3	490 ± 70	85 ± 6
As	ng/m^3	42 ± 7	3.25 ± 0.2
Se	ng/m^3	14 ± 2	2.5 ± 0.2
Br	ng/m^3	38 ± 6	136 ± 9
Sb	ng/m^3	10 ± 2	2.1 ± 0.2
Ba	ng/m^3	170 ± 14	19 ± 2
La	ng/m^3	17 ± 2	1.5 ± 0.1
Sm	ng/m^3	2.0 ± 0.3	0.20 ± 0.02
W	ng/m^3	3.4 ± 0.7	0.24 ± 0.02
Pb	ng/m^3	250 ± 50	440 ± 20

[a]Beijing data from this work. Washington, D.C. data Ref. 7. Uncertainties are standard deviations of the mean values.

BEST COPY AVAILABLE

sulfate during transit. Possibly Beijing does not have such large SO_2 sources to the west.

Despite the high loading of the Beijing atmosphere, some concentrations are comparable to or less than those in Washington. Vanadium and Ni in Washington arise from oil combustion in power plants, whereas China has few oil-fired plants Lead and Br in Washington arise from combustion of leaded gasoline, whereas Beijing has few, if any vehicles that run on leaded gasoline.

6. Size Distribution of Resuspended Particles Bearing Various Elements

Much of the suspended particulate matter in the atmosphere is wind-entrained soil. Because of the importance of this component, we need to know its composition rather well to interpret airborne particle compositions. C. M. Thompson designed and built a chamber for the resuspension of dried, sieved, soil samples and collection of separate size fractions of the particles. Soils from several areas were resuspended, and the various size groups analyzed by INAA at the NBS reactor. The soils under investigation were collected from MLO, two places in China and in Laurel, MD. Results were reported in Dr. Thompson's Ph.D. thesis.

7. Shanandoah Valley Samples

A major environmental problem of our time is acid deposition. To control acid deposition in an optimal way, we must identify sources of acid precursors, find out how they are transported and deposited and how they are chemically converted to acids. In work supported by EPA, we are trying to identify elements borne by atmospheric particles that can serve as characteristic signatures of certain types of sources or areas of the country. S. Tuncel and I. Olmez subjected samples collected by EPA to analysis by INAA. Shaw and Paur collected samples for 15 months at rural sites in Kentucky, Indiana and Ohio[8] and Stevens et al. for three weeks in the Shenandoah Valley.[9] They collected particles in two size fractions, greater and less than 2.5-μm diam and analyzed them by x-ray fluorescence (XRF). The XRF method is rapid, highly automated technique for analyzing large numbers of samples, but it mainly observes major elements. INAA is more expensive and time-consuming than XRF, but yields data for many trace elements that are potentially useful tracers e.g. Se, As, Sb, In. The combined XRF and INAA results yield data for about 40 elements. We have analyzed fine particles, as they provide much more information about sources than large particles, which are dominated by local soil. Back-trajectories for air masses sampled during each period were calculated by J. Parrington using a model and meterological data from NOAA to identify areas over which the air was transported in order to see if the compositions of particles from different areas have characteristic signatures.

The Shenandoah work is complete and was recently published.[10] A major result of the

BEST COPY AVAILABLE

work was the observation of a regional sulfate component which carries with it small amounts of Se, Mn, V, Zn, As, Sb, In and Pb. The amounts of Se and Mn are great enough that, even in the midst of eastern cities such as Boston and Washington, appreciable amounts of the airborne concentrations of these elements come into the area with regional sulfate. The Se borne by regional sulfate undoubtedly originates from major sources of SO_2 gas, especially coal-fired power plants. At present we do not know if most of the other elements also arise from coal-fired plants.

Over 200 samples from the Ohio River Valley Study have been analyzed by INAA. We are now interpreting the data in an attempt to answer some of the questions noted above, including those raised by the much smaller data set from Shenandoah.

8. Philadelphia Samples

During the summer of 1982, EPA sponsored detailed studies of the sources of atmospheric particles in the atmosphere of Philadephia. Particles were collected at three ambient sampling sites in that area for one month using dichotomous samplers, which collect particles with diam above and below 2.5 μm separately. EPA personnel analyzed all of the samples by XRF and sent the fine fractions here for their analysis of INAA. I. Olmez and A. Sheffield analyzed these samples and have submitted the results to EPA. We are not reporting the results here, as EPA may use the combined data sets in a "blind", round-robin test of receptor models used for various research groups. Samples were also collected by John Cooper et al. of NEA, Inc[11] from seven important sources of particles in the Philadelphia area: a coal-fired power plant, two oil-fired plants, a refinery, an incinerator, and Al plant, and an Sb roaster. They were subjected to XRF at NEA, Inc. and then sent here for INAA. Three sets of fine and coarse samples from each source were analyzed by Olmez and Sheffield, and the results are being prepared for joint publication by NEA, EPA and our group.

9. Deep Creek Lake Samples

During the summer of 1983, EPA, DOE and EPRI and their contractors collected ambient samples at a site near Deep Creek Lake, MD and in stacks and plumes of several coal-fired plants upwind of the site. These samples have been subjected to XRF in other laboratories and are being analyzed by INAA by our group.

BEST COPY AVAILABLE

1. I. Olmez and G. E. Gordon, Rare Earths: Atmospheric Signatures for Oil-Fired Power Plants and Refineries, Science (in press, 1985).
2. W. H. Zoller, J. R. Parrington and J. M. Phelan Kotra, Iridium Enrichment in Airborne Particles from Kilauea Volcano, Science 222, 1118 (1983).
3. L. W. Alvarez, W. Alvarez, F. Asaro and H. V. Michel, Science 208, 1095 (1980).
4. I. Olmez, D. L. Finnegan and W. H. Zoller, Iridium Emissions from Kilauea Volcano, submitted to J. Geophys. Res.
5. W. C. Cunningham and W. H. Zoller, J. Aerosol Sci. 12, 367 (1981).
6. G. Tuncel, Trace Elements at the South Pole Atmosphere: Temporal Variations and Sources, Ph.D. thesis,, Dept. of Chemistry, Univ. of Maryland, College Park, MD, 1985.
7. G. S. Kowalczyk, G. E. Gordon and S. W. Rheingrover, Environ. Sci. Technol. 16, 79 (1982).
8. R. C. Shaw, Jr. and R. J. Paur, Atmos. Environ. 17, 2031 (1983).
9. R. K. Stevens, T. G. Dzubay, C. W. Lewis and R. W. Shaw, Jr., Atmos. Environ. 18, 261 (1984).
10. S. G. Tuncel, I. Olmez, J. R. Parrington, G. E. Gordon and R. K. Stevens, Environ. Sci. Technol. 19, 529 (1985).
11. J. E. Howes, J. A. Cooper and J. E. Houck, Sampling and Analysis to Determine Source Signatures in the Philadelphia Area, Report to EPA, 1985.

BEST COPY AVAILABLE

NON-RRD PROGRAMS

CHARACTERIZATION OF THE NBSR AT 20MW

D. A. Becker
(Center for Analytical Chemistry)

and

T. Williamson
(University of Virginia)

and

N. Bickford

Recently, the National Bureau of Standards nuclear reactor (NBSR) was upgraded to 20MW (thermal). With the higher neutron flux densities and modification of one of the pneumatic tube irradiation facilities, an extensive recharacterization extended the previous work on the NBSR[1], and several new techniques were developed which simplified data accumulation and resulted in better information about these facilities.

Described below are techniques used to measure the following parameters: thermal neutron flux density; flux density variations within an irradiation volume; relative fast neutron flux densities; temperatures generated by different sample matrices in various irradiation facilities; and pressures generated in sealed containers by radiolytic decomposition. Also included are some of the results obtained for the NBSR, and for two University reactors used by NBS personnel during the NBSR shutdown period.

1. Neutron Flux Density Measurements

For this work, neutron flux density measurements were made using the thin foil technique, in which the measurement is made with minimum disturbance of the surrounding neutron environment. The foils used were 0.95 cm (3/8 inch) diameter iron foils, with a thickness of 0.0028 cm (0.0011 inch). One to six foils were used per measurement, depending on the flux density expected. Each foil weighs approximately 17 mg. Thermal neutron data was obtained using the nuclear reaction

$$^{58}\text{Fe (n, gamma) } ^{59}\text{Fe}$$

with the 1.292 Mev gamma-ray of iron-59 used for calculations. Using the same foil, the fast neutron flux density can be measured with the nuclear reaction

BEST COPY AVAILABLE

^{54}Fe (n, p) ^{54}Mn

and the 0.835 Mev peak of manganese-54. Since the halflives of both isotopes are relatively long, the foils can be counted at almost any time up to about six months after irradiation. In some cases, fast neutrons were measured with nickel foils using the more sensitive Ni-58 (n, p) Co-58 nuclear reaction.

The technique used for the flux density measurements was as follows: foils were placed in the appropriate position(s) in the irradiation container, held tightly in position with polyethylene foam packing material; the container was irradiated in the appropriate facility; the foil(s) were then removed and counted on a calibrated semiconductor detector and pulse height analysis system. If the detector is calibrated for absolute counting efficiency using a standard radioactive source, and the appropriate corrections made, the absolute neutron flux density can be calculated. This had been done for the original characterization. However, current data has been calculated based on the NBSR RT-4 flux density at 10 MW being equal to 1.30×10^{13} $n/cm^{-2}s^{-1}$. This value was that obtained originally using copper foils[1], and was later verified by others using a variety of measurement materials[2,3].

Selected NBSR irradiation facilities currently available and the thermal neutron flux density of each are found in table 1. Also included in the table are values obtained for the University of Maryland and the University of Virginia nuclear reactors. Table 2 contains data on the relative thermal-to-fast neutron flux densities for these reactors.

The relative numbers of fast neutrons shown in table 2 are based on the NBSR RT-4 facility being equal to 1.00, with all others compared to that value. All of these foils were counted on the same detector using the identical geometry. It should be noted that for the accurate comparison between foils counted by different people, intercalibrated detectors or absolutely calibrated detectors must be used.

Additional flux density measurements were made in RT-5 with iron and nickel foils to determine the thermal and fast flux densities, respectively. The RT-5 pneumatic tube terminal is in the vicinity of the graphite thermal column, and the flux density in this facility is affected by the position of a boral curtain. The thermal flux density with the curtain open is shown in table 1. With the curtain down, the flux densities were measured with an eight day exposure. The values obtained from this are 8×10^{7} $n.cm^{-2}s^{-1}$ for the thermal neutron fluence rate and 2×10^{5} $n.cm^{-2}s^{-1}$ for the fast neutron fluence rate. The fast neutron value was

BEST COPY AVAILABLE

Table 1. Thermal Neutron Data.

Reactor	Facility	Maximum Flux Density[a]	Location[b]
NBSR	Pneumatic tube RT-1	7.7	Proximal end
NBSR	Pneumatic tube RT-3	10.3	Proximal end
NBSR	Pneumatic tube RT-4	2.7	Proximal end
NBSR	Pneumatic tube RT-5	0.032	Bottom
NBSR	Vertical tube G-2	18.0	Core gap
U. of Md.	Pneumatic tube	0.29	Top end
U. of Va.	Pneumatic tube	0.99	Top end
U. of Va.	Hydraulic tube	0.97	Top end
U. of Va.	"Hot" tube[c]	0.17	Bottom end

[a] $\times 10^{13}$ $n.cm^{-2}s^{-1}$

[b] Location of maximum flux density inside the irradiation container; for horizontal tubes, proximal end is that end nearest the reactor core center.

[c] Boral shielded facility.

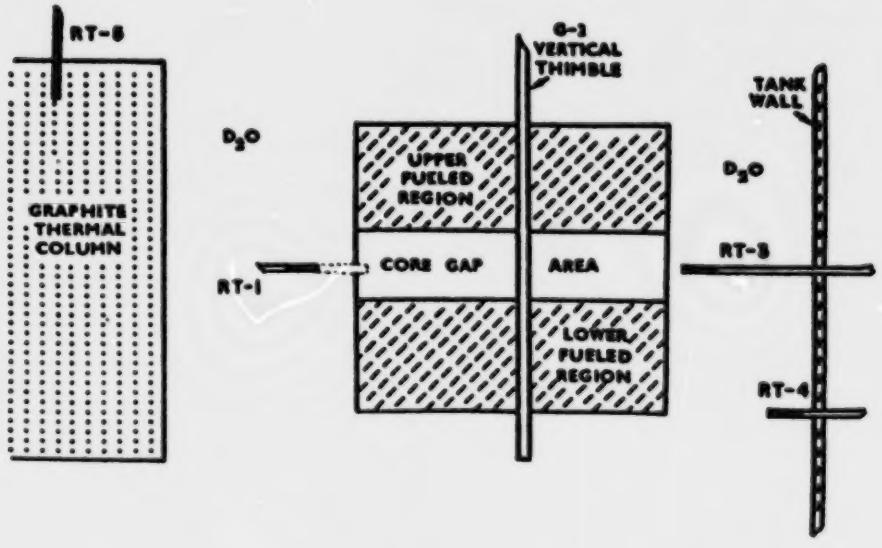

Figure 1. NBSR irradiation facilities at 20 MW.

BEST COPY AVAILABLE

Table 2. Fast Neutron Data

Facility	Reactor Power	Relative Thermal/ Fast Ratio[a] Bottom/ Proximal	Distal	Relative No. of Fast Neutrons[b]
NBSR RT-1	10 MW	49.1, 48.4	84.3	122
	20 MW[c]	242, 269		27.2
NBSR RT-2	10 MW	8.1, 8.0	7.5	593
	20 MW	--- REMOVED ---		---
NBSR RT-3	10 MW	103, 101	155, 158	49.3
	20 MW	96		100
NBSR RT-4	10 MW	1203, 1200	1860	1.00
	20 MW	1257		1.86
NBSR RT-5	10 MW	1.5×10^6		
NBSR G-2	20 MW	64.5[d]		259
U. of Md.				
- P. Tube	200 kW	5.2		51
U. of Va.				
- P. Tube	2 MW	14.3		64
- Hyd. Tube	2 MW	16.7		54
- "Hot" Tube[e]	2 MW	0.55		284

[a] For the various irradiation facilities identified in column 1; relative values are for Fe-59 activity/ Mn-54 activity taken from a single count. (Note: Bottom refers to vertical irradiation facilities; proximal and distal refer to horizontal irradiation facilities, the proximal end being that end nearest the reactor core center.)

[b] Based on RT-4 = 1.00

[c] RT-1 incore terminal moved during power upgrade.

[d] At core gap centerline.

[e] Boral shielded facility.

BEST COPY AVAILABLE

calculated from the measured Co-58 activity using a fission spectrum averaged cross section (0.107 b). Since the boral curtain should have little effect on the fast neutrons, this fast neutron flux density value should also be valid for the curtain open case.

The RT-5 measurements described above were made with the thermal column cavity empty. When a large cadmium absorber (700 g) was placed in the cavity and iron foils irradiated, the cadmium absorber caused an 18 percent reduction in the thermal flux density in the RT-5 irradiation container.

2. Neutron Flux Density Variations

Variations in flux density as a function of irradiation volumes can be a very significant source of error in neutron activation analysis. Many reactors with vertical irradiation facilities have side-to-side differences which are difficult to compensate for or eliminate. The primary irradiation facilities in the NBSR have horizontal in-core terminals, which minimizes side-to-side variations but introduces a horizontal dropoff factor (figure 1). Fortunately, the horizontal factor can be easily corrected, by careful sample/standard positioning, by an appropriate correction factor, or by reversing the irradiation container at a predetermined time during the irradiation period.

The NBSR horizontal and circumferential flux density variations were thoroughly evaluated for the original reactor power lever[4], and would not be expected to change significantly for the higher power lever (except for RT-1, which had the in-core terminal modified) (figure 1). These original measurements were confirmed at 20 MW[5]. In RT-1, which was relocated prior to 20MW operation, the horizontal thermal flux density dropoff was found to be still linear, with a maximum value of 28 percent over the irradiation container (rabbit) length. The fast neutron dropoff as determined by Ni-58 activation was 52 percent. The circumferential flux variation of less than $\pm$ 1 percent for RT-3 was also confirmed, with a maximum side-to-side variation of 1.7 percent over the 2.5 cm inside diameter (figure 2).

3. Temperature Measurements

Many reactor irradiation facilities have limitations for time and sample quantities, due in part to the sample temperatures generated during irradiation. In particular, the irradiation of heavy elements such as lead, and of strong neutron absorbers such as cadmium and boron nitride cause concern on the part of reactor operators. For the NBSR, the temperatures developed in various sample matrices were

BEST COPY AVAILABLE

measured using commercially available irreversible temperature indicating labels. A portion of these labels turns black when a specific temperature is reached or exceeded. These labels have been found to be very useful for evaluating the gamma and/or neutron heating of various materials when irradiated in a nuclear reactor. By use of a series of these labels on a sample, or a single label containing multiple temperature indicators, the maximum temperature "seen" by a sample can be readily determined.

Initial tests were made with small quantities of materials irradiated for short times, gradually working up to maximum values. Measurements were made on some "typical" materials and some "worst case" materials. These included high purity fused silica, lead, iron, nickel, cadmium, boron nitride, quartz ampoules filled with various materials, and polyethylene. Maximum temperatures allowed in pneumatic tube facilities usually were 125 degrees C(257 degrees F) due to use of linear polyethylene rabbits and polyethylene packing and containment materials. It was found that the indicated temperatures were very reproducible, and not affected by several hours irradiation to a neutron fluence of 1×10^{18} $n.cm^{-2}$.

Typical results using these labels revealed that: the NBSR RT-1 facility (7.7×10^{13}) could irradiate 12.9 grams of solid fused silica with no temperature problem, while in RT-3 (10.3×10^{13}) 5.6 grams of silica became too hot in five minutes; the RT-3 tube could be used with 25 grams of boron nitride for only 6 seconds; and the RT-4 tube (2.7×10^{13}) could irradiate 4.9 grams of lead to equilibrium and keep below 125 degrees C.

In addition to the temperature measurements described above, a second set of temperature measurements were made in the pneumatic tube facilities RT-1, RT-3 and RT-4 at 20 MW by inserting samples of graphite, polyethylene and lead into the reactor and measuring the sample temperatures with a thermocouple immediately upon removal. Each temperature sensing sample was machined to a right circular cylinder 10 mm in diameter and 20 mm long. A 3 mm hole was drilled along the cylindrical axis to the center so that a thermocouple probe could be inserted. Each cylinder was held in place in the polyethylene rabbit with polyethylene foam packing. A rabbit containing a temperature sensing cylinder was irradiated, immediately opened, a thermocouple inserted and the temperature noted. Typically, temperature readings were made within 30 seconds of removal from the reactor core, and the observed temperature would rise to a maximum value before decreasing to room temperature. The maximum temperature was recorded. In cases where the temperature exceeded about 80 degrees C, the maximum temperature would be reached very quickly and the temperature

BEST COPY AVAILABLE

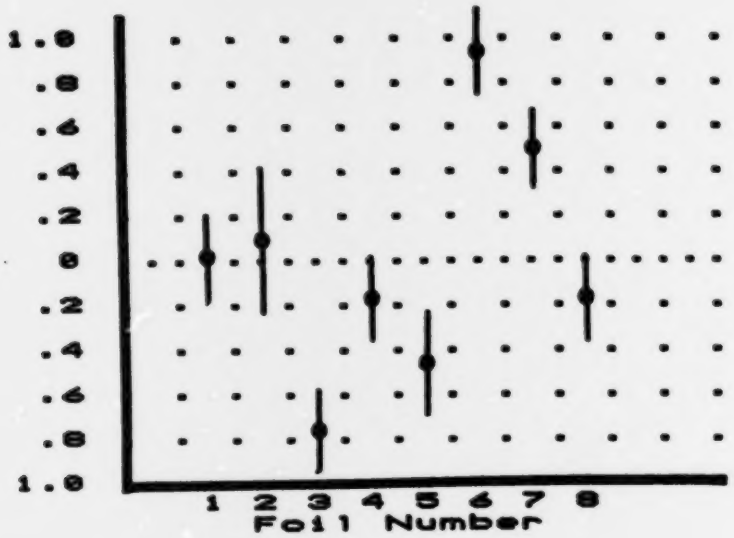

Figure 2. Circumferential neutron flux density distribution in NBS RT-3 (Note: error bars represent counting statistics).

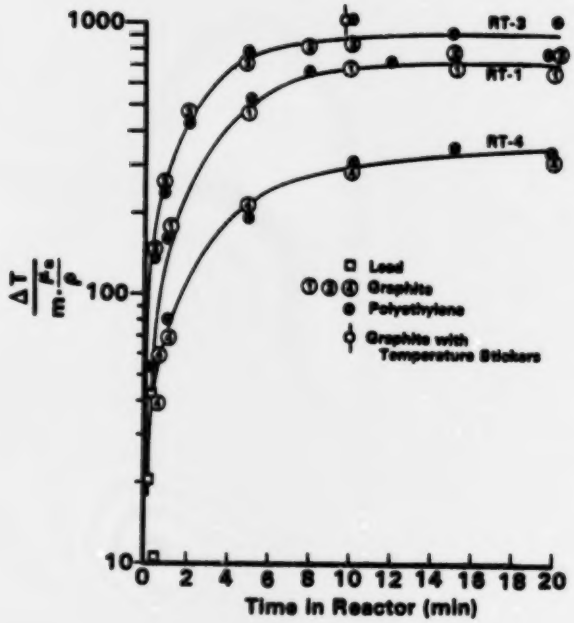

Figure 3. Temperature factors versus irradiation time.

BEST COPY AVAILABLE

would then decrease rapidly. This indicates that, at these higher temperatures, the rate of heat loss upon removal from the core is too rapid to be able to obtain an accurate maximum temperature by this technique. To evaluate the true maximum temperature for one of these samples, temperature indicating stickers as described at the beginning of this section were fastened to the graphite thermocouple sample, and irradiated for 10 minutes in RT-3. The sensors indicated a maximum temperature between 95 and 110 degrees C. The thermocouple reading for this sample was 90 degrees C, which indicates that for this sample the true maximum temperature was somewhere between 5 and 20 percent higher than the measured thermocouple maximum.

The data obtained from the thermocouple measurements was also used to examine relationships between the heating rates of the different materials. If the dominant heating mechanism during reactor irradiation is gamma heating, then the heat transfer rate should be proportional to the mass energy absorption coefficient and to the sample mass. The heat transfer rate is also proportional to the temperature differential. The data plotted in figure 3 are the temperature differential (measured sample temperature minus room ambient temperature) divided by the sample mass (g) and the gamma-ray mass energy absorption coefficient versus reactor irradiation time. The energy absorption coefficient at 600 kev, the nominal energy of fission gamma-rays, was used.

The data in figure 3 appear to agree quite well for different sample materials for an individual pneumatic tube irradiation facility. It must be cautioned, however, that these points represent measurements made only on right circular cylinders packed firmly in polyethylene foam. Other geometrical forms with different surface to volume ratios and other types of packing may substantially alter the heat transfer characteristics.

The data in figure 3 also indicate that sample temperature equilibrium is reached after approximately 10 minutes in the reactor. This agrees well with the data obtained using the temperature labels, which showed equilibrium reached between 10 and 20 minutes irradiaton in the pneumatic tubes for all samples measured to date.

4. Pressure Measurements

In the original characterization effort, pressure buildup in sealed samples due to radiolytic decomposition was determined qualitatively using a pressure inflating device[1]. Some later measurements were made with a manometer, estimating the increased pressures and then trying to calculate back to the pressure inside the ampoule.

BEST COPY AVAILABLE

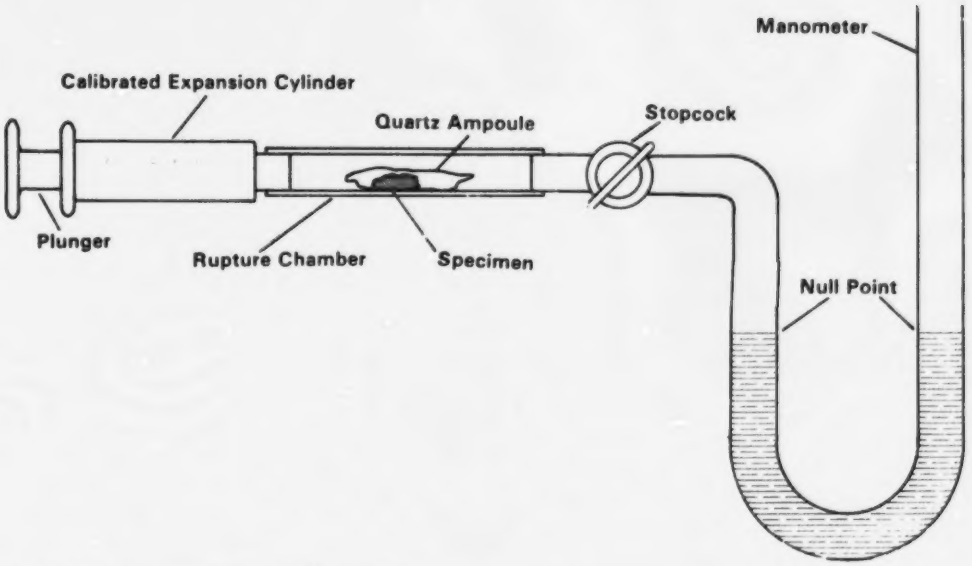

Figure 4. Pressure measurement system.

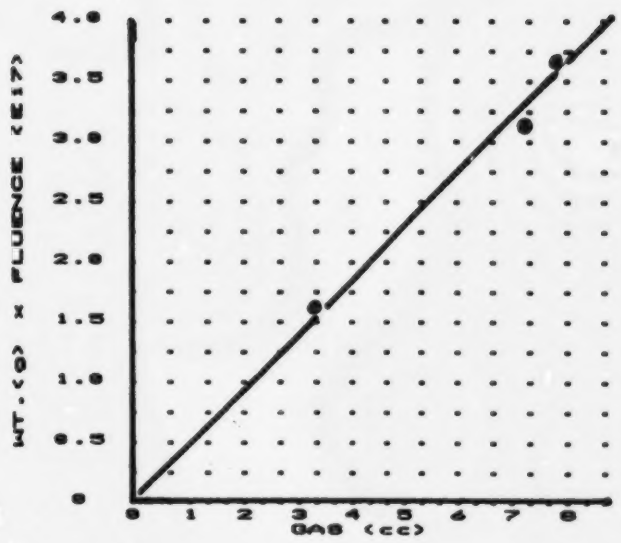

Figure 5. Plot of gaseous products versus sample weight times neutron fluence, for SRM Tomato Leaves in NBSR RT-3.

BEST COPY AVAILABLE

For this recharacterization work, a new system was developed which permits the accurate determination of pressures developed inside sealed quartz and polyethylene containers. This system is described in greater detail elsewhere[5], but will be discussed briefly here. This device utilizes a calibrated expansion cylinder in conjunction with a manometer (figure 4). The cylinder is used to bring the system pressure (after rupture of the irradiated container) back to pre-rupture system pressure ($\pm$ 1 atmosphere). Thus, the gas produced by irradiation (i.e., excess pressure) can be read directly from the increased volume of the calibrated cylinder. This occurs because the pressure of the system before and after the measurement is the same, 1 atmosphere, and the "dead" volume of the system is the same, and cancels out of the calculation. The result is that the equation for calculating pressure in the quartz ampoule (or sealed polyethylene container) is considerably simplified, and requires only the volume of the irradiated ampoule, corrected for the true sample volume, and the increased system volume after expansion back to one atmosphere pressure (as read off of the expansion cylinder).

Some results of this test can be seen in figure 5. Three samples of SRM 1573, Tomato Leaves, were irradiated for various times in the NBSR RT-3 pneumatic tube facility. It is apparent that for this facility the amount of gas produced is directly proportional to the sample weight times the neutron fluence. Additional data indicates that gas production from other irradiation facilities does not fit this same straight line, but apparently depends on the specific characteristics of each irradition facility.

5. Conclusion

Techniques have been developed to characterize the NBSR irradiation facilities for parameters important to neutron activation analysis and other purposes, and to understanding optimum safe irradiation conditions for these reactor facilities. It is hoped that the techniques reported here will be found useful in the characterization of other irradiation facilities and nuclear reactors as well.

---

1. Becker, D. A. and LaFleur, P. D., J. Radioanalytical Chem. 19, 149 (1974).

2. Fleming, R. F., Private Communication.

3. McElroy, W. N., Kellogg, L. S., and Matsumoto, W Y., NBS Technical Note 714, p. 58, U.S. Dept. of Commerce (1972).

BEST COPY AVAILABLE

4. Becker, D. A., in NBS Reactor: Summary of Activities, NBS Technical Note 758, U.S. Dept. of Commerce, Washington, DC (1973).

5. Becker, D. A., J. Radioanalytical and Nuclear Chemistry, (in press).

SUMMARY OF REACTOR RELATED ACTIVITIES CARRIED OUT BY THE NEUTRON FIELD STANDARDS GROUP

D. Gilliam, J. Grundl, G. P. Lamaze and E. McGarry
(Center for Radiation Research)

The Neutron Field Standards Group of the Center for Radiation Research (CRR) is engaged in the development and application of standard and reference neutron fields as permanent facilities for neutron detector calibrations, neutron dosimetry standardization, and reaction rate cross-section measurements. These activities are closely associated with similar international efforts. A component of the CRR makes use of the NBS Research Reactor thermal column and tangential beam tubes where facilities, designed and built by the Neutron Field Standards Group, are in operation. Included with this report is a revision of the Facilities' summary table: "Characteristics of NBS Neutron Sources and Fields For Detector Calibrations and Reaction Cross Section Measurements".

The following paragraphs report on recent activity progress.

1. Distribution of Neutron Fluence Standards

The cavity fission source was in operation before the long shutdown for the production of neutron fluence standards for reactor pressure vessel dosimetry and related programs. Eight species of fluence standards have been produced to date for materials neutron dosimetry applications: In(n,n'), Ni-58 (n,p), Fe-54(n,p), Ti(n,p), Rh(n,n'), Al(n,α), U-238(n,f). Fission neutron fluences certified for these standards are, in the range 0.7 to 60 x 10^{14} neutrons/cm^2.

Arrangements are in progress with CBNM, Geel, to convert NBS SRM-U0002, highly depleted uranium, to a pressed encapsulated pellet to be used as a U-238 fluence standard. This detector when used in conjunction with a natural uranium sample makes a so-called "paired uranium detector" (PUD). The use of PUD's allows the separation of the responses of U-235 and U-238 in power reactor environments.

Neutron fluence standards have also been provided to benchmark the neutron fields of the experimental rooms at the Armed Forces Radiobiological Research Institute (AFRRI). The reactions employed were Np(n,f), U-238(n,f), In-115(n,n'), Fe-54(n,p), Ni-58(n,p), Mg-24(n,α), Al-127(n,α), and Fe-56(n,p). Additionally, members of the neutron fields standards group made measurements at AFRRI with NBS fission chambers which have been calibrated at the NBS reactor.

BEST COPY AVAILABLE

2. Improvements in Fluence Measurements in the NBS Cavity Fission Source

International intercalibration of standard neutron fields is important for establishing absolute accuracies of neutron fluences and reaction rates. A fluence transfer via the Pu(n,f) reaction was made from Cf-252 to the SCK/CEN, MOL, Belgium cavity fission source [$U\text{-}235_{MOL}$] and then to the NBS cavity fission source. The diameter of the MOL cavity (in the BR1 Reactor, Mol, Belgium) is larger (1m) than that of the NBS cavity, resulting in a smaller correction for reflected neutrons. It also has a large cylindrical U-235 fission source which allows an active fission chamber to be placed at the center of the field. The following describes the salient features of the NBS cavity fission source and the fluence transfer procedure which resulted in an overall reduction in the uncertainties of fluence measurements at NBS.

The U.S. standard U-235 fission neutron spectrum at the National Bureau of Standards in Gaithersburg, Maryland, operates in the center of a 30-cm diameter spherical cavity located in the graphite thermal column of the NBS Research Reactor. The facility is frequently called the Cavity Fission Source (CFS). The upper view in figure 1 shows, in detail, the CFS assembly[1] containing neutron sensors and the lower view shows its location within the thermal column cavity. Two disks of U-235 metal (16mm dia x 0.13 mm thick) are placed above and below a cylindrical cadmium pill box 0.076cm thick, which encloses approximately six passive neutron sensors (nominally 1.27cm diameter x 0.025cm thick). The neutron sensors to be irradiated are held in the center of the assembly by light-weight aluminum pieces.

Fission fluence rates of ~2 x 10^{10} $n/cm^2 \cdot s$ are obtained between the U-235 source disks at a separation distance of one centimeter. Applications include detector calibrations for reactor dosimetry and fission cross section measurements.

The absolute source strength, and therefore the fluence rate, of the CFS is dependent upon reactor power level. Consequently, a fluence monitor that is independenty calibrated is required for each irradiation. Both the 70.8-day Ni-58(n,p)Co-58 reaction and the 4.5-hr In-115(n,n')In-115m reaction together with a fission-chamber or a power level monitor have been used. The CFS fluence is tied through these monitors back to known Cf-252 fission neutron fields.

In the fluence transfer technique, a neutron sensor response is measured first in a standard neutron field and then in the field to be calibrated. For example, transfer from a Cf-252 standard neutron field to the NBS U-235 CFS has been accomplished by the In-115(n,n')In-115m reaction. Foils of known purity are irradiated to a certified fluence in the californium field. The indium foils are then analyzed with a radioactivity detector having a reproducible geometry. The

BEST COPY AVAILABLE

factor Φ_{Cf}/R_{Cf} ($n \cdot cm^{-2}$ per $counts \cdot s^{-1} \cdot gm^{-1}$) is thereby established for the neutron sensor. Here R_{Cf} could refer to any reproducible response such as counting rate, reaction rate, or fission rate in the field of interest.

The same indium neutron sensor, or a different indium sensor with a known mass, is then exposed to a certified fluence in the U-235 field and the desired fluence, Φ_{235} is given by:

$$\Phi_{235_U} = \frac{\Phi_{Cf}}{R_{Cf}} \cdot R_{235_U} \cdot \frac{\bar{\sigma}_{Cf}(In)}{\bar{\sigma}_{235_U}(In)} \qquad (1)$$

The spectrum-averaged, cross-section-ratio term on the extreme right of Eq.(1) is more accurately known than the cross sections themselves because errors in the scalar magnitudes are eliminated by the division. For the In-115(n,n')In-115m reaction, the cross section ratio has been calculated to be 1.048 ± 1.6%, using ENDF/B-V differential cross section data and the NBS evaluations of the Cf-252 and U-235 fission spectra. However, different analytical forms of the U-235 spectrum give calculated ratios which are as small as 1.015. The experimental value for the ratio is 1.031 ± 2.1%.[3] to circumvent this uncertainty in the fluence transfer process, the Pu-239(n,f) reaction has replaced In(n,n') for fluence transfer based upon new experiments performed at a U-235 cavity fission source in Mol, Belgium.[3] For Pu-239, the spectrum-averaged cross section ratio is 1.003 ± 0.2%, with only a 0.3% uncertainty resulting from different descriptions of this spectra.

3. Fluence Transfer Through the Belgian U-235 Fission Spectrum

Figure 2 shows the U-235 cavity fission source assembly at the SCK/CEN Laboratory, Mol, Belgium.[4] This assembly incorporated a 100-cm dia. cavity as opposed to the 30-cm dia. cavity for the NBS U-235 field. The significance of the large cavity is that there are substantially fewer low-energy (wall returned) neutrons in the Belgian field. Also, the larger source permits exposure of high quality, light-weight Pu-239 deposits in an NBS fission chamber. This chamber cannot be used in the smaller volume NBS Cavity Fission Source.

Figure 3 depicts the present and former (indium-"only") fluence transfer procedures from the NBS Cf-252 fission spectrum. With the exception of differences in the scattering corrections in the Belgian and NBS U-235 fields, their energy spectra are identical. Therefore, details of the cross section of the reaction chosen as the transfer instrument do not matter (see Eq.3 at bottom of figure 3). Scattering differences in the two fields require a net adjustment of almost 4%; however, this correction has been calculated to ± 1.4%.

BEST COPY AVAILABLE

NBS CAVITY FISSION SOURCE

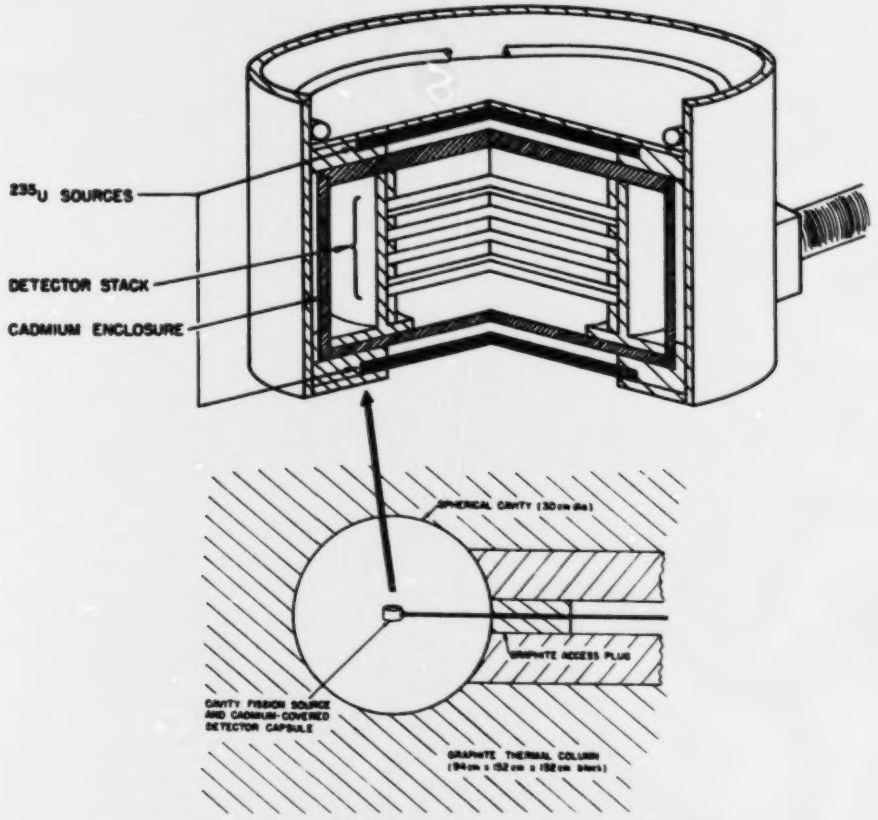

Figure 1. The NBS Cavity Fission Source

Belgian (SCK/CEN) ^{235}U Fission Spectrum Field in BR1 Reactor Thermal Column

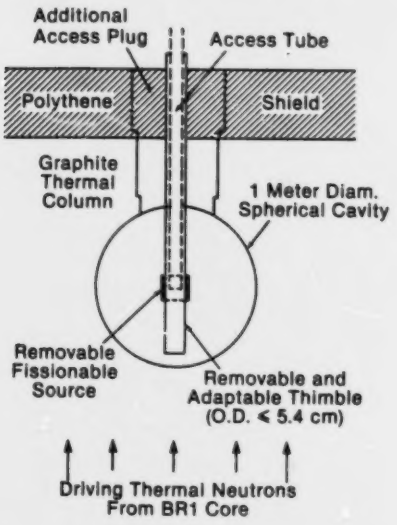

Figure 2.

BEST COPY AVAILABLE

Table 1.

Summary Of Uncertainties In Fluence Transfer Measurements

- For Transfer From NBS ^{252}Cf Field to Belgian ^{235}U Field

Source of Uncertainty	Contribution (%)
Source Strength of ^{252}Cf	0.9
^{252}Cf-Source to ^{239}Pu-Deposit Distance	0.6
Statistics of Fission Counting	0.1
Precision of 2π Fission Counting Corrections	0.4
^{239}Pu Cross-Section Ratio in ^{252}Cf Field and ^{235}U Field	0.1
Scattering Corrections for ^{239}Pu in ^{252}Cf Field	0.7
Wall Return Corrections in Belgian ^{235}U Field	0.6
Scattering Corrections for ^{239}Pu in Belgian ^{235}U Field	0.1
Total Uncertainty in Fluence Transfer = (Contributions Taken in Quadrature)	1.5%

Table 2.

Summary Of Uncertainties In Fluence Transfer Measurements

- For Transfer From Belgian to NBS ^{235}U Field

Source of Uncertainty	Contribution (%)	
	For ^{115}In (n, n')	For ^{58}Ni (n, p)
Statistics of Gamma Counting	0.2	0.4
Scattering + Wall Return in Belgian ^{235}U Field	1.1	1.7
Scattering + Wall Return in NBS ^{235}U Field	0.8	0.8
Fluence-Rate Gradient in NBS ^{235}U Field	0.4	0.4
Total Uncertainty in Fluence Transfer = (Contributions Taken in Quadrature)	2.1%	2.5%

BEST COPY AVAILABLE

Present and Former Procedures for Calibration Of The Neutron Fleunce Rate In The NBS ^{235}U Cavity Fission Source

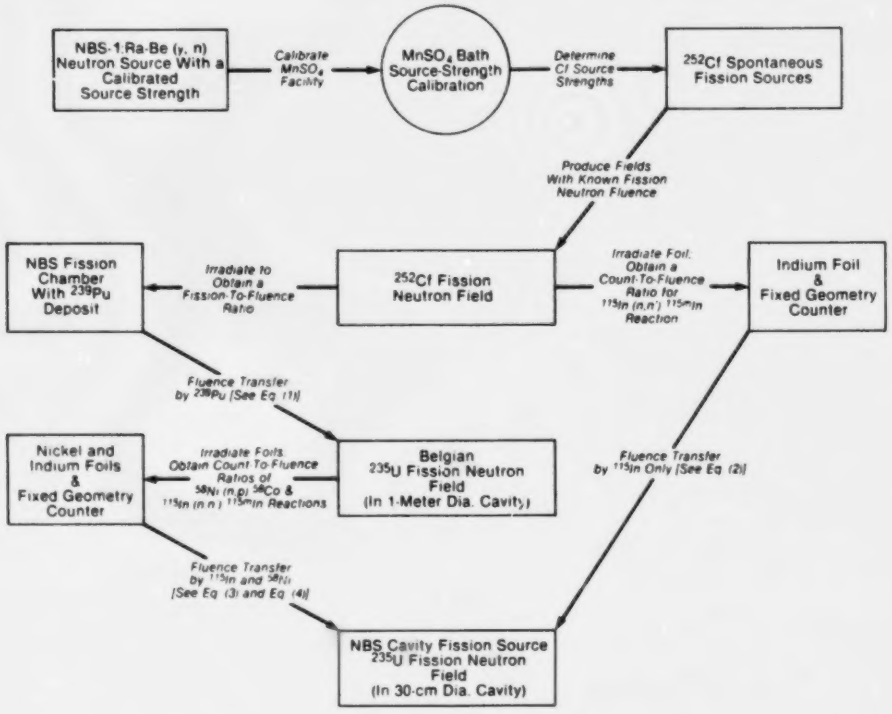
NBS-1 Ra-Be (γ, n) Neutron Source With a Calibrated Source Strength
Calibrate MnSO4 Facility
MnSO4 Bath Source-Strength Calibration
Determine Cf Source Strengths
252Cf Spontaneous Fission Sources
Produce Fields With Known Fission Neutron Fluence
NBS Fission Chamber With 239Pu Deposit
Irradiate to Obtain a Fission-To-Fluence Ratio
252Cf Fission Neutron Field
Irradiate Foil. Obtain a Count-To-Fluence Ratio for 115In (n,n') 115mIn Reaction
Indium Foil & Fixed Geometry Counter
Fluence Transfer by 239Pu [See Eq. (1)]
Nickel and Indium Foils & Fixed Geometry Counter
Irradiate Foils. Obtain Count-To-Fluence Ratios of 58Ni (n,p) 58Co & 115In (n,n') 115mIn Reactions
Belgian 235U Fission Neutron Field (In 1-Meter Dia. Cavity)
Fluence Transfer by 115In Only [See Eq. (2)]
Fluence Transfer by 115In and 58Ni [See Eq. (3) and Eq. (4)]
NBS Cavity Fission Source 235U Fission Neutron Field (In 30-cm Dia. Cavity)

$$\phi^{SCK/CEN}_{U\text{-}235} = \left[\frac{\phi_{cf}}{F^{Pu\text{-}239}_{cf}}\right] \bullet F^{Pu\text{-}239}_{U\text{-}235} \bullet \left[\frac{\bar{\sigma}^{Pu\text{-}239}_{cf}}{\bar{\sigma}^{Pu\text{-}239}_{U\text{-}235}}\right] \quad (1)$$

$$\text{Old}\,\phi^{NBS}_{U\text{-}235} = \left[\frac{\phi_{cf}}{R^{In\text{-}115}_{cf}}\right] \bullet R^{In\text{-}115}_{U\text{-}235} \bullet \left[\frac{\bar{\sigma}^{In\text{-}115}_{cf}}{\bar{\sigma}^{In\text{-}115}_{U\text{-}235}}\right] \quad (2)$$

$$\text{New}\,\phi^{NBS}_{U\text{-}235} = \left[\frac{\phi^{SCK/CEN}_{U\text{-}235}}{R^{Ni\text{-}58}_{U\text{-}235\,(SCK)}}\right] \bullet R^{Ni\text{-}58}_{U\text{-}235\,(NBS)} \quad (3)$$

$$\text{New}\,\phi^{NBS}_{U\text{-}235} = \left[\frac{\phi^{SCK/CEN}_{U\text{-}235}}{R^{In\text{-}115}_{U\text{-}235\,(SCK)}}\right] \bullet R^{In\text{-}115}_{U\text{-}235\,(NBS)} \quad (4)$$

Figure 3.

BEST COPY AVAILABLE

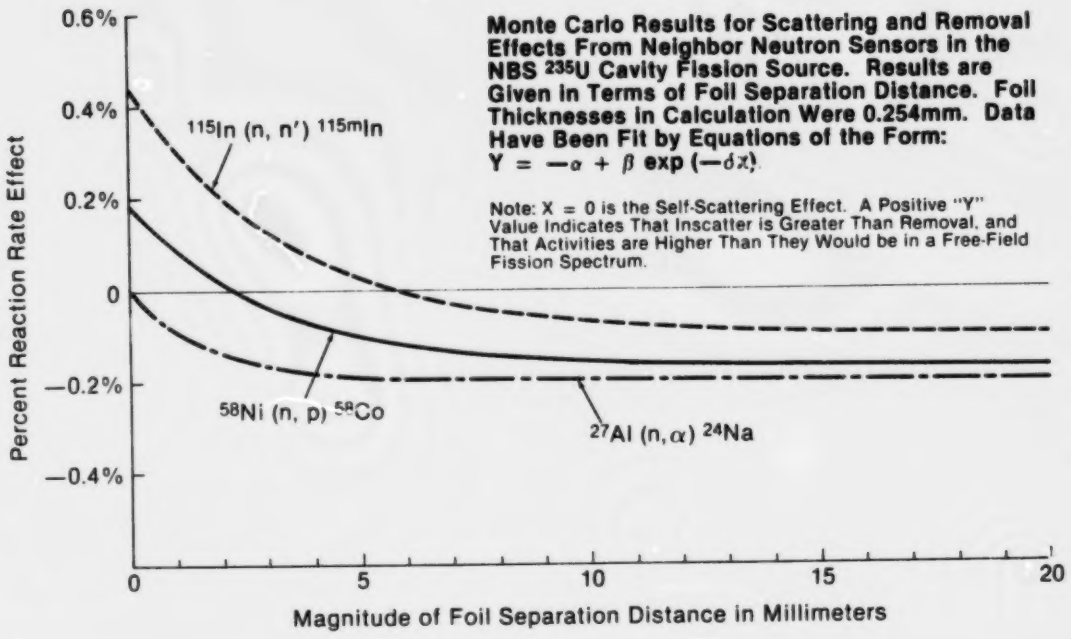

Monte Carlo Results for Scattering and Removal Effects From Neighbor Neutron Sensors in the NBS ^{235}U Cavity Fission Source. Results are Given in Terms of Foil Separation Distance. Foil Thicknesses in Calculation Were 0.254mm. Data Have Been Fit by Equations of the Form: $Y = -\alpha + \beta \exp(-\delta x)$.

Note: X = 0 is the Self-Scattering Effect. A Positive "Y" Value Indicates That Inscatter is Greater Than Removal, and That Activities are Higher Than They Would be in a Free-Field Fission Spectrum.

Figure 4.

Tables 1 and 2 summarize the transfer process. The total uncertainties for In(n,n') and for Ni-58(n,p) are the uncertainties of Table 1 and 2 taken in quadrature. Respectively, these are 2.0% and 2.3%.

4. Neutron Scattering and Removal Effects

Corrections must be made for effects of neutron scattering and removal because of the variety of materials in close proximity to each neutron sensor undergoing irradiation in a cavity fission source. For example, there are cadmium, aluminum in support structures, uranium in the fission disks, and various elements in other dosimeters. The corrections are a complex function of the cross sections (or thresholds) of the dosimetry reactions as well as the position of a particular sensor relative to all other materials. The present corrections for the NBS CFS are based upon rather extensive Monte Carlo calculations of indium, nickel and aluminum dosimeters in a detailed model of the cavity fission source. The results are summarized in figure 4.

BEST COPY AVAILABLE

1. Compendium of Benchmark and Test Region Neutron Fields for Pressure Vessel Irradiation Surveillance; Standard Neutron Spectra. NRC NUREG/CR-0551, Progress Report--July-Sept. 1978 (Dec. 1978).

2. "Neutron Fluence and Cross Section Measurements for Fast Neutron Dosimetry," G. P. Lamaze, D. M. Gilliam, E. D. McGarry, NBS, Gaithersburg, Maryland; A. Fabry, SCK/CEN Laboratory, Mol, Belgium; Proc. of Int'l. Conf. Nucl. Meth. and Environ. and Energy Res., San Juan, PR (April 1984) Conf-840408

3. "Cross Section Measurements in the U-235 Fission Spectrum Neutron Field," D. M. Gilliam, J. A. Grundl, G. P. Lamaze, C. M. Eisenhauer, NBS, Gaithersburg, Maryland; A. Fabry, SCK/CEN Laboratory, Mol, Belgium. Proc. Fifth ASTM/EURATOM Symposium on Reactor Dosimetry, Geesthacht, W. Germany (Sept. 1984). To be published.

4. "The Mol Cavity Fission Spectrum Standard Neutron Field and Its Applications," A. Fabry, G. Minsart, F. Cops, and S. DeLeeuw; Proc. Fourth ASTM/EURATOM Symposium on Reactor Dosimetry, Washington, DC (March 1982).

BEST COPY AVAILABLE

NEUTRON DRIVEN GAMMA RAY FIELD

G. Lamaze, E. Boswell, J. Grundl, D. Gilliam, D. Blackburn
(Center for Radiation Research)

and

T. Williamson
(University of Virginia, Charlottesville, VA)

A neutron driven gamma ray field, similar to one in operation at SCK/CEN Mol, Belgium, has been constructed to operate in the NBSR thermal column cavity. The system consists of an extruded cadmium cylinder one mm thick and 55 mm diameter. In the thermal column cavity, the cadmium is exposed to a thermal neutron fluence rate of 3 E 11 n/cm^{2}s. Since the cadmium is essentially black to thermal neutrons, a cadmium capture gamma ray fluence rate of about 2 E 11 photons/cm^{2}s is produced at the center of the cylinder. This corresponds to a dose rate of close to a megarad/hr. The gamma ray field strength is determined by two methods: exposing gold foils on the cadmium surface, and by measuring the induced Cd-115 activity. These measurements provide an estimate of the neutron reaction rate in the cadmium from which a gamma ray source strength may be derived. The gamma ray dose or fluence on the axis of the cylinder is obtained from a simple geometry calculation.

As shown in figure 1, the cadmium cylinder can be enclosed in a 64 mm sheath of lithium -6 loaded glass to determine the background of gamma rays from the core and from neutron capture in the surrounding graphite. An iron cylinder, which fits around the lithium glass, has been made to provide an alternate source of iron capture gamma rays in known geometry.

First application of the neutron driven gamma ray field is a measurement of photofission rates in U-238, Th-232, and Np-237 and photon activation rates in indium. A typical traverse along the axis of the cadmium cylinder taken in the course of these measurements with a U-238 fission chamber is shown in figure 2. The photofission due to the background gamma fluence is presently estimated to 7% of that from the cadmium source and fission from fast neutron leakage from the reactor to be 2% of the cadmium photofission rate.

The thermal neutron fluence rate in the center of the cavity without the gamma ray source in place is 2.7 E 11 n/cm^{2}s as measured with thin gold foils. The gold cadmium ratio with the cadmium cylinder in place is 8000.

BEST COPY AVAILABLE

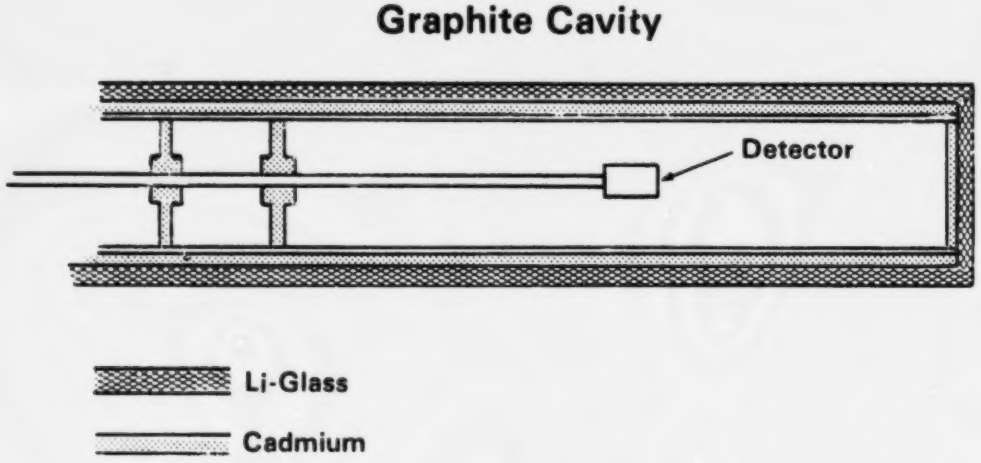

Figure 1. Assembly sketch of Neutron Driven Gamma-Ray Source (NDGS). The assembly as shown is placed in the NBSR thermal column cavity.

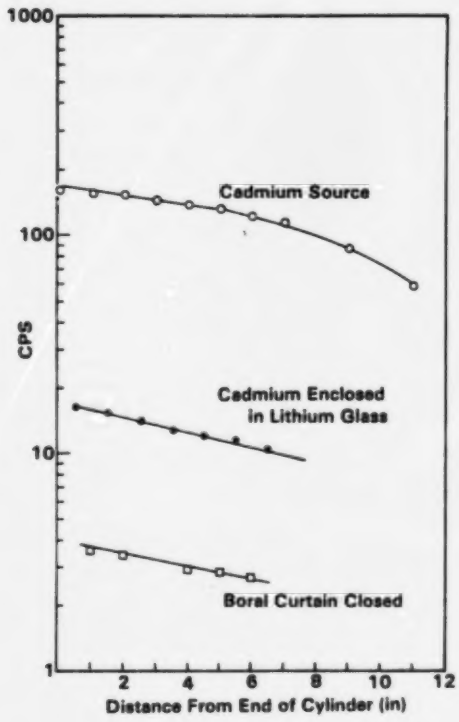

Figure 2. Fission rate transverses taken along the axis of the axis of the NDGS with a U-238 fission chamber.

BEST COPY AVAILABLE

NON-RRD PROGRAMS

EXPERIMENTAL MICRODOSIMETRY

Robert B. Schwartz
(Center for Radiation Research)

Introduction

In the previous progress report, we discussed preliminary measurements made at the 144 keV beam with our tissue-equivalent proportional counter ("TEPC"). These measurements have been repeated with lower noise electronics to allow us to extend the measurements to lower energy, and measurements were also made at the 24 and the 2 keV beams. Results are given in the form of y vs. y·D(y) plots. The 144 keV results are in good agreement with calculated spectra, and with other measurements. The 24 keV measurement is internally consistent, but we have no other results with which to compare it. The 2 keV results are interesting, but their interpretation is a bit uncertain and there are no other published measurements or calculations for comparison.

1. Data Analysis

Computer programs have been written in BASIC to take the pulse height analyzer data (counts per channel) and calculate lineal energy (y), the absorbed dose distribution (D(y)), and the product of y times D(y).

2. Experimental Notes

We have continued to use the Far West Technology LET-1/2 tissue equivalent proportional counter, with an equivalent diameter of one micron of tissue. The data at the filtered beams were taken on an (ancient!) Northern Scientific analyzer, sent to an HP 85 computer and stored on a tape cassette. The analysis programs (for computing the centroid position of the alpha particle calibration peak, and for extracting microdosimetric information from the pulse height data) were also run on the HP 85. The results were printed out on an HP 82905B printer. We do not as yet have any plotting programs for the HP, so the results were plotted by hand. This system is usable, if slightly inelegant.

In previous measurements of the Californium-252 microdosimetric spectrum, we noted that electronic noise was a limitation at lineal energies below about 1 keV/μm. To reduce the noise, the voltage on the counter was increased from 500 v. to 620 v. This increased the gas gain by about a factor of five. It would also have overloaded the amplifier, but we dropped the gain of the pre-amp (ORTEC 142 PC) by about a factor of five by adding a 1 pf feedback capacitor. We thus have approximately the

BEST COPY AVAILABLE

same size pulses going into the main amplifier as before, but we can now get down to about 0.15 keV/μm before noise becomes a problem.

3. Microdosimetric Spectra - General

In each neutron field the microdosimetric spectra were taken in three separate runs, with different amplifier gain settings, to cover the lineal energy range from 0.15 keV/μm to 160 keV/μm. The different point shapes in figs. 2, 4, and 6 indicate where data from the different runs were used for plotting. There was sufficient over-lap among the runs to assure that the different runs did, indeed, match up satisfactorily. At the highest amplifier gain setting at each beam (covering the range from 0.15 keV/μm), noise and background were explicitly subtracted. This gave corrections of from 4% to 10% at 0.2 keV/μm, decreasing with increasing lineal energy.

4. 144 keV Results

The fluence spectrum for the 144 keV beam is shown in figure 1. The data are taken from the proton recoil measurements of McGarry and Heimbach. Note that in this type of plot (known as a "lethargy" plot) equal areas under the curve correspond to equal fluences, in much the same way as equal areas under the $y \cdot D(y)$ vs. y curve correspond to equal doses The 144 keV beam fluence has a (barely visible) 1 1/2% impurity at 54 keV, but no high energy impurities. Since the fluence-to-kerma factor at 54 keV is about half of that at 144 keV, we do not expect to see any effect of the 54 keV neutrons The energy spread in the beam is about 25 keV FWHM, so there are a significant number of neutrons in the beam with energies up to about 160 keV.

The microdosimetric spectrum is shown in figure 2. This spectrum is in good agreement with Coyne's calculated spectrum, and also in good agreement with the measurements of Alberts et al. of PTB, presented at the Hamburg meeting. In particular, the small rise at about 0.2 keV/μm (presumably due to gamma events) was also seen by the PTB group.

5. 24 keV Results

The 24 keV beam is slightly more complicated than the 144 keV beam, with small contaminations at 74, 135, 280, and 360 keV neutron energies. (See figure 3.) From previous proton recoil proportional counter measurements, we know the relative fluence in each of these neutron groups, and, using fluence-to-kerma conversion

BEST COPY AVAILABLE

factors, we can calculate the relative dose from the high energy contaminants. This is shown in the following table:

ENERGY (keV)	% OF FLUENCE	KERMA FACTOR ($rad \cdot cm^2$)	REL. DOSE
24	97.0	2.35	2.275
74	0.23	5.13	.012
135	1.6	8.175	.131
280	1.0	12.1	.121
360	.16	13.8	.022
	3.0		.286

That is, the high energy contaminants amount to 3.1% of the 24 keV fluence, but (.286/2.275) x 100 = 13% of the 24 keV dose.

Figure 4 shows the microdosimetric spectrum of the 24 keV beam. The main peak at about 15 keV/μm is clearly due to the 24 keV neutrons, while the events extending above about 25 keV/μm must be due to the higher energy contaminants. From this spectrum we find that the area above 25 keV/μm is 15% of the area between 1 and 25 keV keV/μm, in good agreement with the above calculation. We are not aware of any published calculations or other measurements of this spectrum.

Comparing figure 3 with figure 4 shows how the use of the TEPC is a very sensitive way of seeing relatively small doses from high energy neutrons in the presence of much larger low energy doses.

6. 2 keV Results

The 2 keV fluence spectrum is shown in figure 5, and the microdosimetric spectrum in figure 6. (We had trouble getting reproducible data below ~ 0.4 keV/μm.) The results in this case are not so easy to interpret as those for the 24 keV beam.

The peak at ~ 0.9 keV/μm is, presumably, due to recoil protons from the 2 keV neutrons.

In the case of the 2 keV beam, as with the 24 keV beam, there are higher energy components, extending from 7 to 40 keV, and amounting to about 3% in fluence. From the previously measured intensities of these higher energy neutrons, we calculate

BEST COPY AVAILABLE

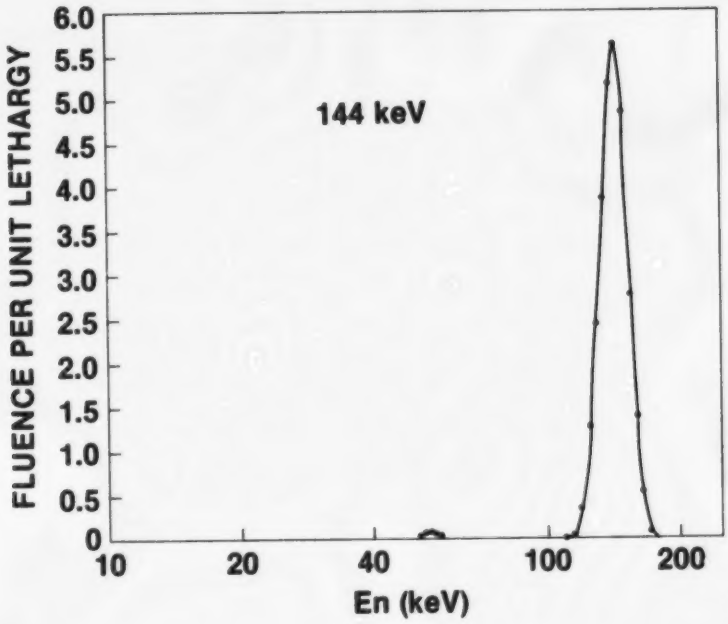

Figure 1. 144 keV Fluence spectrum

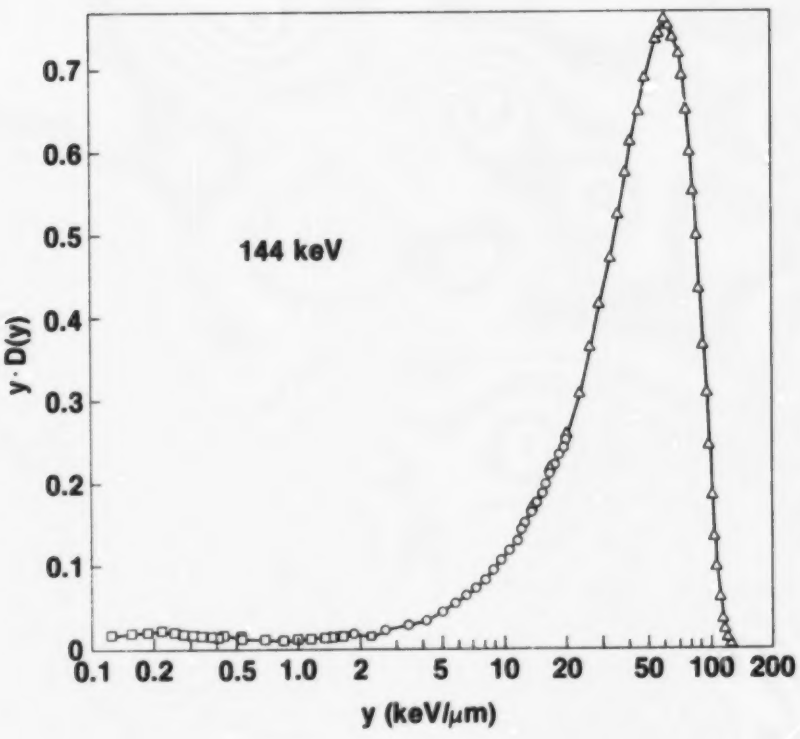

Figure 2. 144 keV Microdosimetric spectrum

BEST COPY AVAILABLE

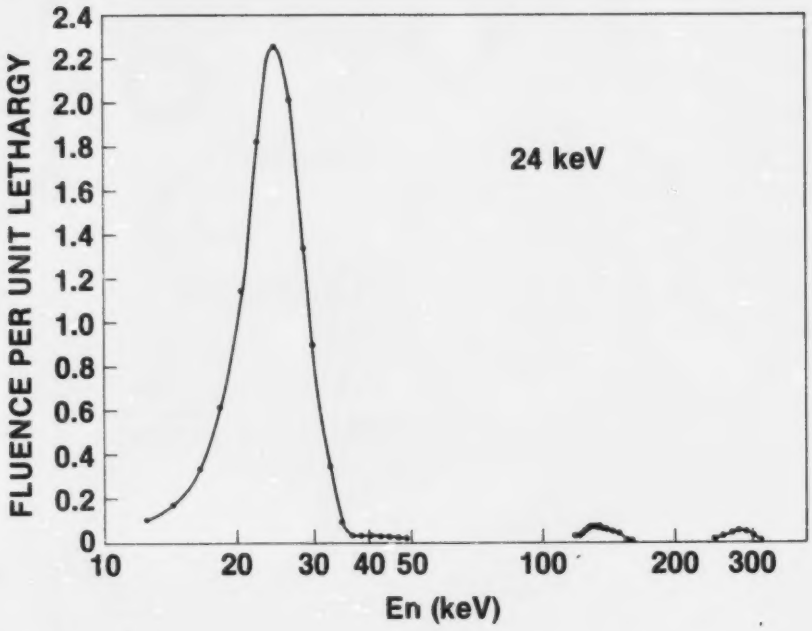

Figure 3. 24 keV Fluence spectrum

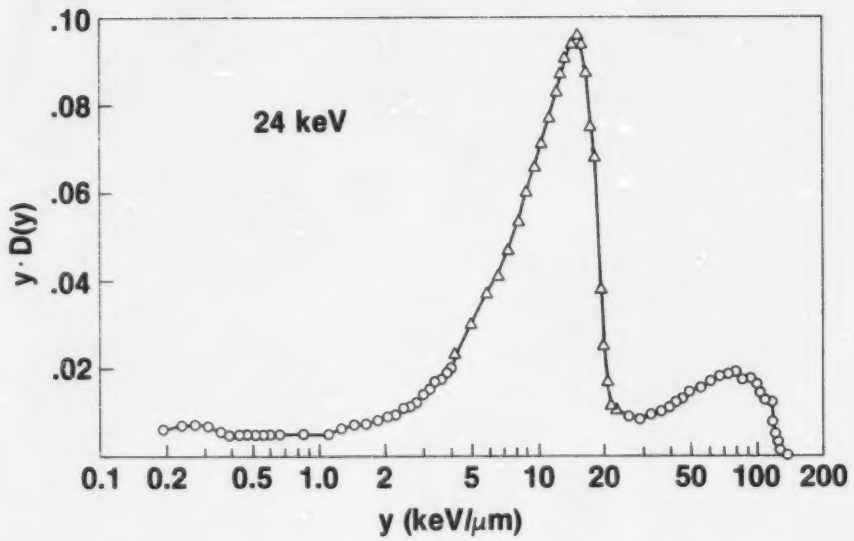

Figure 4. 24 keV Microdosimetric spectrum

BEST COPY AVAILABLE

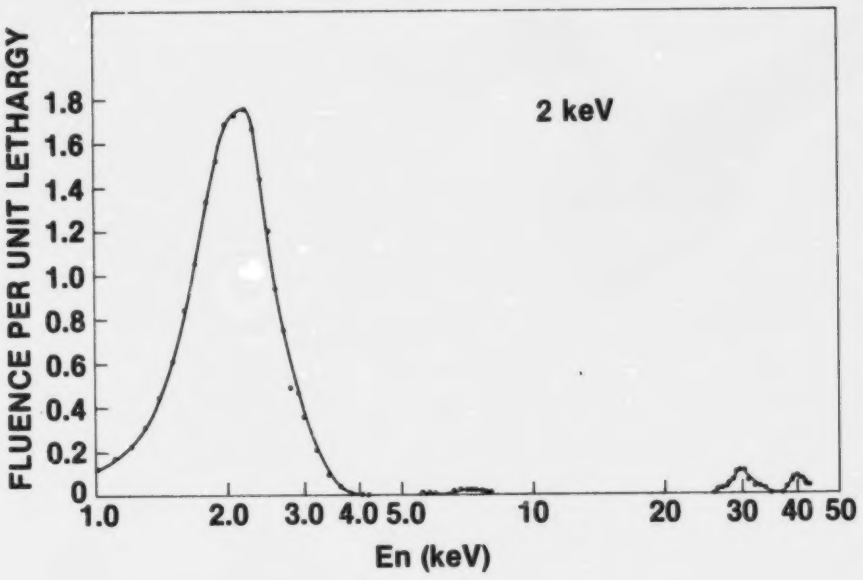

Figure 5. 2 keV Fluence spectrum

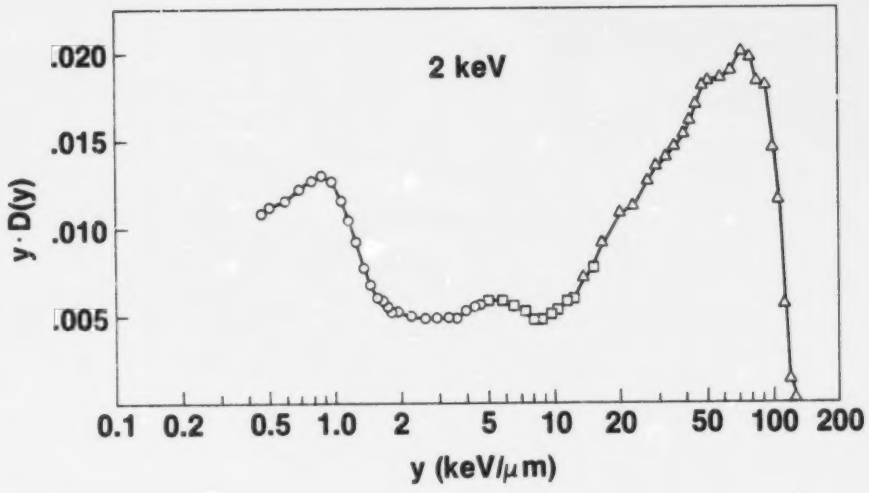

Figure 6. 2 keV Microdosimetric spectrum

BEST COPY AVAILABLE

that the dose from the high energy groups is about 30% of that from the 2 keV neutrons. These neutrons may be responsible for the small "bump" at about 6 keV/μm.

The only source that we can think of for the main peak at ~ 70 keV/μm are the 600 keV protons from the N(n,p) reaction. The kerma factor for the N(n,p) reaction at 2 keV is, however, only ~ 2% of that for the proton recoil reaction. We thus do not now have any quantitative explanation for the shape of this spectrum.

BEST COPY AVAILABLE

C. Reactor Operations and Services

REACTOR OPERATIONS AND SERVICES

On April 3, 1985, the NBS reactor achieved a major milestone, reaching a new high power level of 20 MW, double the power level of the past 16 years. The increased power will greatly enhance the capabilities of the reactor. The upgrade to 20 MW required extensive modifications that resulted in a shutdown of almost 8 months. The shutdown period was also used for planned major improvements and repairs.

1. Reactor Operations

As a consequence of the power upgrade, the reactor was operated on a curtailed schedule for most of the year except the last three months when it was operated on a regular round-the-clock schedule. A summary of the operating statistics for the period July 1, 1984 to June 30, 1985 is presented in the following table:

No. of days at 10 MW	33
No. of days at 10 - 20 MW	13
No of days at 20 MW	67
On-line time at 20 MW	75%
Average U-235 burnup	65%
No. of Irradiations	1500
Hours of Irradiations	1500
Hours per Irradiation	1.0

2. Irradiation Services

Extensive irradiation services were provided to many users from within and outside NBS. Even though the reactor was operated for less than 4 months, more than 1200 irradiations were performed which is 80% of that for the entire previous year.

3. Engineering Services

In addition to normal engineering and design services provided to reactor operations, experimenters and users, the engineering staff was involved in a comprehensive program of reactor modernization.

A shim arm test assembly is nearing completion which will be used for testing shim arm mechanisms and will be available for spare parts for the reactor shim arm mechanisms.

The regulating rod has been modified and the absorber section was fabricated for 20 MW operation. The addition of an electric braking technique has eliminated

BEST COPY AVAILABLE

slippage of the regulating rod. An additional motor was added to the regulating rod to provide additional torque and along with the dynamic brake, allows more flexible tolerances resulting in consistent up and down regulating rod travel times.

Twenty-three fuel element assemblies have been inspected and accepted from the DOE contractor by the NBSR engineering staff. An additional 52 fuel assemblies have been fabricated and are awaiting acceptance. There are 864 compacts made and ready for rolling into fuel plates.

For 20 MW operation many changes and improvements were made in the system. The check valves in the process room were removed to elements maintenance in a high radiation area and increase reliability of the system. The check valves at the pump discharges were removed and the diaphragm valves made to perform the check valve function. All of the pump impellers were changed from 12 3/8 to 13 inch diameter and along with new 125 HP motors have increased flow output. A fourth pump and motor was added to the system.

Two new primary system ion exchange columns were installed along with additional piping since the two old existing columns were left in position so that radioactive decay could reduce the activitiy before removal.

The thermal shield supply and return lines were replaced and are visible unlike the old lines which leaked inside the biological shielding. The new lines have reduced the thermal shield leakage considerably.

A new pneumatic tube for RT-1 was installed along with P_2O lines to provide cooling and neutron moderator to the samples in the tube top.

The heat exchanger HE-1A was cleaned and unless it was pressurized it was discovered that 15 tubes of the 1170 U-tubes had leaks or suspected of having leaks. The tubes were plugged and the heat exchanger returned to service. The second heat exchanger HE-1B was also fixed into the system.

The instrumentation-electronics group of the Reactor Engineering Section continued on with the modernization of the reactor instrumentation in the control room.

In preparation for the increase of reactor power from ten to twenty megawatts operation, additional instruments were installed in the process system along with modernizing of the transmitters, meters and recorders. With human engineering in mind an effort was made to relocate the primary cooling process instruments into flow, temperature and level zones, thus enabling improved recognition time of the process variables.

BEST COPY AVAILABLE

Meters monitoring the secondary cooling variables were condensed and also zoned into an area one-third of their original console space.

Two wide scale radiation monitoring chart recorders were replaced with one programmable chart recorder. An example of convenience using the new recorder switches; a radiation channel can be immediately monitored during a calibration check.

Four delta pressure transmitters with associated flow elements, lines and wiring were installed for monitoring the main heat exchangers HE1A and B, (2) primary outlet and (2) secondary inlet flows. Each transmitting signals to the control room console on recorders and meters respectively.

Four other process flow transmitters were replaced with new transmitters, the two reactor outlets, outer and inner plenum flows. They were also relocated in a lower radiation area of the process room to reduce radiation exposure to personnel while performing required technical specifications testing.

The primary inlet temperature controlling recorder and integrally associated controller were replaced by new separate recorder and programmable controller with the capability of manual operation with the controller removed from the console.

A cabinet for housing 14 new RFI protected temperature transmitters with 9 temperature transmitters activated. Two are new channels: the heat exchanger HE1B primary outlet and the secondary outlet temperature.

Four 4-way (energize to open) solenoid valves and four differential pressure switches were installed on the main pump discharge valves for automatic valve control in the process room. The valves may be remotely operated automatically or manually via 3-way switches from the control room. An annunciator monitors the air reserve tank for low pressure.

The final wiring is completed for the fourth main primary flow pump magnetic starter, lock out, interlocks and remote control switch.

The reactor building tritium monitor is being replaced in stages. The preamplifier via special shielded cable to the electrometer in the control room is being checked out. A second tritium electrometer system to control room is planned.

BEST COPY AVAILABLE

D. Service Programs

THE FOOD AND DRUG ADMINISTRATION'S NEUTRON ACTIVATION FACILITY

W. C. Cunningham and W. B. Stroube, Jr.
(U.S. Food and Drug Administration, Washington, DC)

The Food and Drug Administration (FDA) maintains a neutron activation analysis (NAA) facility in the reactor building of the National Bureau of Standards (NBS). The NAA program at FDA includes analytical support for regulatory activities and special projects as well as applications research. Neutron activation analysis complements the other analytical techniques used at FDA and serves as a reference technique for quality assurance practices.

During the past year hundreds of gamma-ray spectra from previous work on FDA Adult Total Diet Studies food composites[1] were re-examined to obtain additional analytical information and generate a detection limit table. Detection limits were listed for twelve main food groups and for the elements generally determined in foods. The tables can be used to provide a guideline of instrumental NAA (INAA) capabilities for food analyses and will enable FDA analytical scientists to accurately predict whether INAA would be applicable to specific projects.

The detection limit listing is of practical use for two reasons. First, these detection limits are not theoretical but are generated from experimental data. Interferences are accounted for realistically since the limits arise from actual food matrix spectra. Second, the values are based on a sizable data base. The spectra used have been generated during analyses of an entire year's collection of FDA Adult Total Diet Studies samples.

A need for improved capabilities for As, Cr, Mo, Sb and Se resulted in the application of radiochemical neutron activation analysis (RNAA) to the determination of these elements in foods. Work on this project continued this year with hydrated manganese dioxide (HMD) inorganic chromatographic resin. The trace elements are effectively removed from the interfering elements, mainly Br, K, Na and P, which are present in food matricies. A post-irradiation digestion is used in this procedure along with a chromatographic separation. Accuracy and precision were verified by analyzing SRM's; several foods were also analyzed. This RNAA procedure increases FDA's analytical capabilities for these trace elements in foods and provides a reference technique for other procedures.

---

1. Cunningham, W. C. and Stroube, W. B., Jr., The Science of the Total Environment, (submitted for publication).

BEST COPY AVAILABLE

PREPARATION OF F-18 LABELED RADIOTRACERS USING NBS REACTOR-PRODUCED F-18

W. C. Eckelman, M. Channing, and J. Bennett
(National Institutes of Health, Clinical Center, Bethesda, MD)

F-18 is produced by irradiating 0.4g enriched $^{6}Li_2CO_3$ for 2 hours at 1.1 x 10^{14} n/cm^2/sec. The quartz ampule is then returned to NIH for processing in a semiautomatic processing facility. The quartz ampule is cracked and Li_2CO_3 is mixed with cation exchange resin in water. The aqueous solution is transferred to a round bottom flask containing base and carrier fluoride. The water is evaporated and acetonitile is added. The acetonitile is evaporated and the process is repeated twice again. The substrate is then added to the fluoride. To date, two substrates have been used: (1) methyl 4,6-O-benzylidene 2,3-cyclic sulfate-B-D-Manno-pyranoside--a precursor to 2-fluoro-2-deoxy glucose, and (2) the 6-triflate derivative of naltrexone. Both are produced in 60% radiochemical yield.

---

1. C. B. Pert, J. A. Danks, M. A. Channing, W. C. Eckelmann, S. M. Larson, J. M. Bennett, T. R. Burke, Jr. and K. C. Rice, "3-[^{18}F] Acetylcyclofoxy: A Useful Probe for the Visualization of Opiate Receptors in Living Animals," FEBS 2001. 177, 2 (1984)

2. M. A. Channing, W. C. Eckelmann, J. M. Bennett, T. R. Burke, Jr. and K. C. Rice, "Radiosynthesis of [^{18}F] 3-Acetylcyclofoxy: A High Affinity Opiate Antagonist," Int. J. Appl. Radiat. Isot. (to be published)

PRODUCTION OF F-18 ON LOW FLUX REACTORS

M. S. Neuder, M. C. Channing, S. M. Larson
(National Institutes of Health, Clinical Center, Bethesda, MD)

and

R. F. Fleming
(Center for Analytical Chemistry)

The production of F-18 in oxygen-containing lithium compounds, such as Li_2CO_3, enriched to 95.56% in Li-6, occurs by the neutron irradiation of Li-6 in the reaction $^{6}Li(n,\alpha)^{3}H; ^{16}O(^{3}H,n)^{18}$. When irradiating at fluxes of about 10^{14} n/cm^2/sec, obtaining the maximum yield of F-18 per gram of lithium is important, and can be accomplished by insuring a high degree of surface area-to-volume ratio. From a theoretical standpoint, this would minimize self-shielding and flux depression contributions to overall sample yields. These contributions can, in fact, be

BEST COPY AVAILABLE

separately analyzed by performing the following experiment. Quartz tubes varying in diameter from 1 to 4 mm id, and containing lithium carbonate are irradiated individually in an evacuated spherical cavity. The cavity, about 12 inches in diameter and contained in graphite, has the advantage that a fairly uniform flux distribution will exist in the region of an absorber whose dimensions are small in comparison with the mean free path in the surrounding medium. Additionally, the flux depression which would normally be present at the surface of a tube irradiated in a given medium, would be considered negligible in the cavity. Rather, a depression is created in the vicinity of the cavity, i.e. the graphite. In effect, then, only a self-shielding contribution to the overall F-18 yields will be measured. The flux depression contribution to F-18 yields can subsequently be determined by irradiating in the graphite region surrounding the cavity. In this case, sample self-shielding and flux depression at the tube surface will exist. The difference in the empirically-derived self-shielding measurements, obtained at each location, is then a direct measure of the flux depression existing at the sample surface. Irradiations conducted in other areas of the reactor facility will permit the degree to which the flux depression contributes to overall F-18 experimental yields to be assessed. Additionally, reactivity comparisons can be made among othe suitable lithium compounds once these self-shielding and flux depressin contributins are accounted for in F-18 yields.

---

1. R. F. Fleming. Int. J. Appl. Radiat. Isot. 33, 1263, (1982).

2. K. M. Case, F. DeHoffmann, and G. Placzek. Introduction to Theory of Neutron Diffusion, Vol. 1 (LANL, Los Alamos, 1953).

3. M. S Neuder, W. C. Eckelman, M. C. Channing, and S. M. Larson, "The Production of F-18 on Low Flux Reactors," Poster Exhibit, The Society of Nuclear Medicine, 32nd Annual Meeting, 1985.

BEST COPY AVAILABLE

REACTOR RADIATION DIVISION

460

R. S. Carter, Chief
T. M. Raby, Deputy Chief
*E. C. Maxwell, Admin. Officer
T. L. Lindstrom, Secretary
*S. E. Tassey, Clerk-Steno

Division Staff
R. Casella
B. Mozer
F. Shorten

Cold Neutron Project
J. M. Rowe (1/2)
P. Kopetka
R. Williams

Reactor Operations
T. M. Raby, Chief
J. F. Torrence, Deputy Chief
C. Harrison, Secretary

Engineering Services
J. H. Nicklas, Chief
C. Harrison, Secretary

Neutron Condensed Materials Sci.
J. J. Rush, Chief
Mary Clark, Secretary
+L. K. Clutter, Clerk-Steno

BEST COPY AVAILABLE

Reactor Operations

R. Beasley
M. Bell
N. Bickford
J. Browning
A. Chapman
J. Clark
H. Dilks
L. Lindstrom
M. McDonald
W. Muellar
T. Myers
J. Ring
R. Stiber
A. Toth
D. Wilkison

Mechanical Design

E. Guglielmo
J. Sturrock

Electronics

R. Conway
R. Hayes
L. Shuman

Crystallography

#C. Choi
J. LaRock (1/2)
E. Prince
W. Rymes (1/2)
A. Santoro
#V. Himes
A. Mighell
J. Stalick
+D. Stakes

Metal Hydrides and Molecular Materials

D. Fravel (1/2)
#H. Prask
J. Rowe (1/4)
W. Rymes (1/2)
#S. Trevino

Magnetic and Amorphous Materials

#H. Alperin
#J. Gotaas
#J. Lynn
J. Rhyne
#M. Spano

Biological Materials

#H. Savage
A. Wlodawer

Advanced Neutron Methods

N. Berk
D. Fravel
C. Glinka
J. LaRock (1/2)
J. Rowe (1/4)

Neutron Radiography

M. Ganoczy
#T. Cheng

*Part-time
+WAE, Coop, Stay-in-school
#Guest Worker, research assoc.

PERSONNEL ROSTER

NON-RRD NBS STAFF LOCATED AT REACTOR

Division 354

D. Brown
C. Campbell
P. Cassidy
I. Jensen
F. Moore
J. Shubiak
J. Wang

Division 532

E. Boswell
C. Eisenhauer
D. Gilliam
J. A. Grundl
G. Lamaze
E. McGarry
I. Schroder
R. Schwartz

Division 551

D. Becker
S. Carpenter
G. Downing
R. Fleming
J. Langland
R. Lindstrom
G. Lutz
J. Maki
B. Norman
S. Stone
R. Zeisler

GUEST WORKERS AND COLLABORATORS

Division 400

J. Cahn

Division 401

J. Slabaugh

Division 420

F. Brickman
J. Blendell
B. Burton
B. Coblenz
T. Coyle
S. Frieman
K. Frase
E. Fuller
K. Hardman-Rhyne
G. Olson
C. Robbins
R. Roth
B. Steiner

Division 430

R. Fields

Division 440

B. Bauer
T. Davis
C. Han
C. Chiang
R. Waterstrat
W. Wu

Division 450

F. Biancanello
J. Early
R. Reno
R. Shaefer
R. Shull

Division 520

G. Greene
E. Kessler

Division 522

R. Dove

Division 532

A. Wasson

BEST COPY AVAILABLE

PERSONNEL ROSTER

Division 533

R. Placious

Division 541

R. Cavanagh
R. Kelly
T. Madey

Division 543

A. Wlodawer
I. Weber

Division 544

D. Tsai

Division 552

S. Wise
L. Sander

Division 553

H. Rook

Division 725

J. Ehrstein

Aberdeen Proving Ground

C. Heimback

Armed Forces Institute of Pathology

D. Nagarajan

Army Armament Research and Development Command

C. Choi
H. Prask
S. Trevino

Federal Bureau of Investigation

R. Asbery
R. Bilko
J. Haverkost
J. Kilty
P. Kostella
M. Moscop
C. Peters
J. Riley
P. Tangren
P. Thompson

Food and Drug Administration

W. Cunningham
W. Stroube, Jr.
J. Tanner

National Gallery of Art

B. Miller
C. Parkhurst

National Institutes of Health

J. Bennett
M. Channing
D. Davies
B. Dunn
W. Eckelman
R. Frank
A. Katki
C. Lowe
A. Maxwell
M. Neuder
R. Nossal
H. Savage

Naval Research Laboratory

D. Edelstein
A. Ehrlich
K. Grabowski
A. Iman
N. Koon
L. Pecora
L. Richards

Naval Surface Weapons Center

J. Cullen
M. Spano

BEST COPY AVAILABLE

PERSONNEL ROSTER

Smithsonian Institution

R. Bishop
M. Blackman
T. Chase
Y. Cheng
J. Mishara
E. Myers
J. Olin
R. Wright
L. Zacherman

Argonne National Laboratory

S. Susman

Battelle Laboratories

L. Brackenbush
F. Brauer
G. Endres
R. Holiman
W. Nicholson
R. Sanders

Chalmers Institute of Technology

L. Sjolin

C.N.R.S. Grenoble, France

C. Chaillout
D. Gignoux
M. Marezio
J. Soubeyroux
G. Zaccai

Institut Laue-Langevin
Grenoble, France

J. Bouillot
A. Magerl
P. Mangin
R. Pynn

Institute of Nuclear Sciences

R. Drascovic

KFA Jülich, Germany

R. Hempleman
D. Richter
M. Stueppler

Los Alamos National Laboratory

R. Robinson

Max-Planck Institute

R. Huber
J. Walter
E. Lukacevic

Sandia National Laboratory

J. Schirber
J. Harris

Nuclear Energy Center,
Mol, Belgium

A. Fabry

Oak Ridge National Laboratory

F. Kam

Alfred University

S. Kim
R. Snyder

Cambridge University (U.K)

J. Horton
G. Squire

Georgetown University

H. Mallek

Iowa State University

R. Shelton

Kyoto University (Japan)

H. Hasegawa
T. Hashimoto
Q. Trancong

Michigan State University

E. Case
Y. Fan
S. Solin

BEST COPY AVAILABLE

PERSONNEL ROSTER

M.I.T.

B. Averbach
R. Coble
S. Chen
J. Didiskein
M. Green
B. Wuensch

Northwestern University

H. Calderon
S. Kim
J. Weertman

Oregon State Graduate School

P. Davis

Purdue University

J. Furdyna
T. Giebultowicz
A. Overhanser

Rutgers University

M. Greenblatt

San Jose State University

A. Ling

State University of New York

H. Herman
R. Shanker

Tel Aviv University (Israel)

A. Voronel

University of Alabama

J. Segrest

University of Antwerp (Belgium)

K. Michel

University of California (San Diego)

J. Arnold
K. Nishiizumi

University of California (Santa Barbara)

J. Fint
C. Levi
P. Lombrozo
G. Odette

University of Illinois

S. Hardcastle
D. Heumann
M. Salamon
S. Sinha

University of Maryland

D. Anderson
I. Anderson
A. Bates
S. Faller
A. Fiesel
G. Gordon
F. Guenther
M. Han
D. Herman
J. Hoff
M. Kitto
S. Krueger
Q. Li
J. Lynn
C. LeCompte
L. McCarthy
I. Olmez
J. Ondov
J. Robertson
A. Sheffield
P. Sheridan
C. Thompson
G. Tuncel
S. Tuncel
W. Waters
W. Zoller

BEST COPY AVAILABLE

PERSONNEL ROSTER

University of Massachusetts

R. Stein
M. Shibayama
V. Soni
H. Yang

University of Michigan

D. Vincent

University of Milan (Italy)

M. Zocchi

University of Minnesota

V. Garry
T. Lodge

University of Missouri

W. Ching
W. James
T. Little
S. Werner

University of Munster

F. Kemper

University of Notre Dame

R. Ricker

University of Pennsylvania

J. Calem
T. Lutz

Carnegie-Mellon University

E. Boltich
M. Chisholm
W. Wallace

University of Rhode Island

D. Andrauskas
S. Hasanain
S. Pickart

University of Southern California

E. Amis

University of Vermont

T. Flanagan

University of Virginia

T. Williamson

University of Washington

K. Mottet

University of Wisconsin

S. Cooper
D. Huber
M. Landry
J. Miller
H. Spehard
H. Yu

Aerospace Corporation

R. Bowman
J. Knudsen

Baker Chemical Company

R. Ganapathy

Amoco

J. Laduk
C. Marshall

Alcoa Technical Center

C. Jensen
R. Rioja

Allied Corporation

G. Fish
A. Maeland

Atmoic Energy of Canada, LTD

W. Lennard

BEST COPY AVAILABLE

PERSONNEL ROSTER

Bell Laboratories

F. Bates
R. Cava
H. Chen
J. Mitchell
D. Murphy
J. Remeika
J. Riley

Bell-Northern Research Ltd.

F. Shepherd
W. Vandevorst

Directed Technologies, Inc.

N. Chesser

Dow Chemical Company

C. Crowder

Eastmand Kodak

T. Houssain

E. I. DuPont de Nemours Co.

J. Imbelzzno
G. Stucky

Exxon

D. Lohse
J. Gethner
R. Busch

General Electric Co.

C. Austin
R. Bonnan
R. Darlia
L. Provo

W. R. Grace

M. Wax
R. Wormsbecker

Genex Corporation

R. Salemme

GTE Laboratories

D. Oblas
G. Hamill

IBM (San Jose)

G. Hadziioannou

IBM (Yorktown Heights)

M. Schaefer
R. Gambino

Intel Corporation

N. Cox
S. Singhal

3M Research Laboratory

A. Siedle

Motorola, Inc.

S. Wilson

Rockwell International

M. Brown
B. Titmann

Southerwest Research Institute

R. Page

Union Carbide Corporation

P. Leung

Westinghouse-Hanford Corp.

W. McElroy
J. Rawlins

BEST COPY AVAILABLE

F. Publications

COLLABORATIVE PROGRAMS

AMMON, H. L., ZHANG D. CHOI, C. S., SANDUS, O., MARCHAND, A. P., and SURI, S. C., "6,6,8-Trinitropentacyclo[5.3.0.$0^{2,5}$.$0^{3,9}$.$0^{4,8}$]decane, $C_{10}H_9O_6$", Acta Cryst. C41, 404-406 (1985).

BEECH, F., CATLOW, C. R. A., SANTOR, A., and STEELE, B. C. H., "Structural and Electrical Studies of the Defect Pysochlore Materials $Pb_{15}M_2O_{5.5}$ (M=Ta, Nb)", Solid State Ionics (in press).

BEECK, F., CATLOW, C. R. A., SANTORO, A., and STEELS, B. C. H., "Neutron Diffraction and A/C Conductivity Study, Solid State Ionics (in press).

BENHAM, M. J., ROSS, D. K., LARTIGUYE, C., PERCHERON-GUEGAN, A., and ANDERSON, I. S., "Neutron Inelastic Scattering Study of the Effects of Hydrogen Absorption Cycling of $LANI_5/H$", Belfast Conf. On `Hydrogen in Metals' 1985 (in press).

BERK, N. F., MAGERL A., RUSH, J. J., ROWE, J. M., and PROVO, J. L., "Anomalous Vibrations of Hydrogen Isotopes in β-Phase Vanadium Hydride: A Novel, Double-Well Potential", (Submitted to Phys. Rev. Lett.).

BERK, N. F. ans HARDMAN-RHYNE, K. A., "Characterization of Alumina Powder Using Small Angle Scattering, I: Theory", J. Appl. Cryst. 18 (in press).

BERK, N. F. and HANDMAN-RHYNE, K. A. "The Phase Shift and Multiple Scattering in Small Angle Neutron Scattering: Application to Beam Broadening From Ceramics", Physica B (in press).

BERK, N. F. and HARDMAN-RHYNE, K. A., "The Phase Shift and Multiple Scattering in Small Angle Neutron Scattering: Application to Beam Broadening from Cermics", Proceedings of the 1985 Santa Fe Internation Conference on Neutron Scattering, Physica B (to be published).

BOUILLOT, J, ROWE, J. M., RUSH, J. J. and LUTY, F., "Crystal Structure of Mixed Alkali Halide-Alkali Cyanide Mixed Crystals", Bull. Am. Phys. Soc. 30, 456 (1985).

BOUILLOT, J., COQUET, E., PANNETIER, J., and CRETTEZ, J. M. "Neutron Powder Diffraction Studies of $LiIO_3$ and ($HIO_3 \cdot 2LiIO_3$)", Intern. Conf. Neutron Scatt. Santa Fe, Physica B. (in press).

CASELLA, R. C. "Nonlinearity in Weak Magnetic Fields Induced by Neutron-Antineutron Oscillations in Neutron Interferometry and Spin Resonance", Phys. Rev Lett. 53, 1033 (1984).

CAVA, R. J., and SANTORO, A., "Tarascon. The Crystal Structures of the Chevrel Phases $Li_{3.3}Mo_6S_8$ and $Li_{3.2}Mo_6Se_8$", J. of Solid State Chem. 54, 193, 203 (1984).

CAVA, R. J., and SANTORO, A., "The Structure of the Lithium Inserted Metal Odide $Li_{0.5}TiO_2$ (Anatase) $LiTi_2O_4$ (Spinel) and $Li_2Ti_2O_4$", J. Sol. State Chem. (in press).

BEST COPY AVAILABLE

PUBLICATIONS

CAVAGNAT, D., MAGERL, A., VETTIER, C., ANDERSON, I. S., and TREVINO, S. F., "Anomalous Pressure Dependence of the Torsional Levels in Solid Nitromethane, Phys. Rev. Lett. 54, 193 (1985).

CHOI, C. S., and PRASK, H. J., "Neutron Powder Diffraction Studies of Two Uranium-0.75wt% Titanium Alloys", J. Appl. Cryst. 18, 141-144 (1985).

CHOI, C. S., and PRASK, H. J. "Texture of Extruded Uranium Alloy by Neutron Diffraction", J. Appl. Cryst. (in press).

DIDISHEIM, J. J., PRINCE, E., and WUENSCH. B. J., "Neutron Rietveld Analysis of Structural Changes in Nasicon Solid Solutions $Na_{1+x}Zr_2Si_xP_{3-x}O_{12}$", Solid State Ionics (in press).

EICK, H. A., and PRINCE, E. "A Neutron Diffraction and Electron Microscopy Examination of 2BaBr2"BaC12", Acta Cryst., Section C (in press).

ERWIN, R. W., LYNN J. W., RHYNE, J. J. and CHEN, H. S., "Spin Stiffness Anomaly in the Reentrant Spin-Glass $(Fe_{0.25}Ni_{0.75})_{0.75}P_{0.16}B_{0.06}Al_{0.03}$", J. Appl. Phys. 57, 3473 (1985).

FERNANDEX-BACA, J. A., LYNN, J. W., RHYNE, J. J. and FISH, G. E., "Spin Dynamics of the Amorphous Invar alloy $Fe_{0.86}B_{0.14}$", J. Appl. Phys. 57, 3545 (1985).

ERWIN, R. W., LYNN, J. W., and MAGERL, A. "The Reentrant Spin-Glass Order Parameter in $(Fe_{0.3}Ni_{0.7})_{75}P_{16}B_6Al_3$", J. Magnetism and Magnetic Matls. (in press).

FERNANDEZ-BACA, J. A., RHYNE, J. J., and FISH, G. E. "Neutron Scattering Study of the Spin Dynmics of Amorphous $Fe_7Ni_2Zr_1$", J. Magnetism and Magnetic Matls. (in press).

FERNANDEZ-BACA, J. A., LYNN, J. W., RHYNE, J. J., and FISH, G. E., "Spin Dynamics of Amorphous $Fe_{0.86}B_{0.14}$", Physica (in press).

FISHER, R. X., BAUR, W. H., SHANNON, R. D. STALEY, R. H., VIGA, A. J., ABRAMS, L., and PRINCE, E., "Neutron Powder Diffraction Study and Physical Characterization of Zeolite D-Rho", J. of Phys. Chem. (in press).

GIEBULTOWICZ, T. M., and FURDYNA, J. K., "Monte Carlo Simulation of Fcc Heisenberg Antiferromagnet with Nearest and Next-Nearest-Neighbor Interactions", J. Appl. Phys. 57, 3312 (1985).

GIEBULTOWICZ, T. M., RHYNE, J. J., CHING, W. Y., and HUBER, D. L. "Low-Temperature Spin Correlations and Spin Dynamics in Diluted Magnetic Semiconductors", J. Appl. Phys. 57 3415 (1986).

GIEBULTOWICZ. T. M. "Monte Carlo Simulation of Dilute MMagnetic Semiconductors for High Concentrations of the Magnetic Component", J. Magnetism and Magnetic Matls. (in press).

GIEBULTOWICZ, T. M., RHYNE, J. J., CHING, W. Y., HUBER, D. L. and GALAZKA, R. R., "Static and Dynamic Spin Correlations and Exchange Interactions in $Cd_{1-x}Mn_xTe$", J. Magnetism and Magnetic Matls. (in press).

GIGNOUX, D. and RHYNE, J. J., "Spin Excitations in $TbNi_5$ by Inelastic Neutron Scattering", J. Magnetism and Magnetic Matls. (in press).

BEST COPY AVAILABLE

PUBLICATIONS

GILARDI, G. R., FLIPPEN-ANDERSON, J. L., CHOI, C. S., MARCHAND, A. P., and REDDY, D. S., "Structure of 6,6,10,10-Tetranitropentacyclo[5.3.0.$0^{2,5}$.$0^{3,9}$.$0^{4,8}$] decane, $C_{10}H_8O_8$", Acta Cryst. C41, 788-791 (1985).

GLINKA, C. J., SANDER, L. C., WISE, S. A. HUNNICUTT, M. L., and LOCHMULLER, C. H., "Determination of Pore Accessibility in Silica Microparticles by Small Angle Neutron Scattering", Anal. Chem. 57, 2079-2084 (1985).

GOTAAS, J. A., RHYNE, J. J., and WERNER, S. A. "Spin Density Waves in Cu-Mn", J. Appl. Phys. 57, 3404-3406 (1985).

GOTAAS, J. A., RHYNE, J. J., WENGER, S. A., and MYDOSH, J. A., "Long-RanGe Incommensurate Spin State in Dilute YGd Alloys", J. Magnetism and Magnetic Matls. (in press).

GOTAAS, J. A. and LYNN, J. W., "Magnetic Field Dependence of the Small Angle Neutron Scattering in $HoMo_6Se_8$", J. Manetism and Magnetic Matls. (in press).

HAN, C. C., OHADA, M., MUROGA, Y., BAUER, B. V., and TRAN-CONG, E., "Phase Decomposition Phenomena of Polystyrene/Polyvinyl Methylether", SPE ANTEC '85 Conf. Proc. 43, 306 (1985).

HARDMAN-RHYNE, K. A., FRASE, K. G.., and BERK, N. F., "Applications of Multiple Small Angle Scattering to Studies of Ceramic Processing", Proc. of the 1985 Santa Fe Internation Conf. on Neutron Scattering, Physica B (to be published).

HARDMAN-RHYNE, K. A. and BERK, N. F., "Characterization of Alumina Powder Using Small Angle Scattering, I: Experiment", J. Appl. Cyrst., 18 (in press).

HARDMAN-RHYNE, K. A. and BERK, N. F., "Characterization of Alumina Powder Using Small Angle Neutron Scattering, II: Experiment", J. Appl. Cryst. 18 (in press).

HARDMAN-RHYNE, K. A., FRASE, K. G. and BERK, N. F. "Applications of Multiple Small Angle Scattering to Studies of Ceramic Processing", Physica B (in press).

HEMPLEMANN, R., RICHTER, D., ECKOLD, G, RUSH, J. J. ROWE, J. M. and MONTOYA, M., "Localized Hydrogen Modes in $LaNi_5H_x$", J. Less Common Metals 104, 1-12 (1984).

HASEGAWA, H.M, HASHIMOTO, T., KAWAI, H., LODGE, T. P., AMIS, E. M., GLINKA, C. J., and HAN, C. C., "SANS and SAXS Studies on Molecular Conformation of a Block Polymer in Microdomain Space", Macromolecules 18, 67 (198).

HIMES, V. L., MIGHELL, A. D., and STALICK, J. K., NBS Crystal Data Distribution Package (Version of June 1985). Product of the NBS Crystal Data Center consisting of the NBS Crystal Data Identification Field and Software (=NBS*LATTICE). Distributed by the JCPDS--International Centre for Diffraction Data, 1601 Park Lane Road, Swarthmore, PA 19081.

HIMES, V. L., and MIGHELL, A. D. "NBS*LATTICE - A Program to Analyze Lattice Relationship", NBS Tech. Note 1214, U. S. Dept. of Comm./NBS (in press).

HODEAU, J. L, MAREZIO, M., SANTORO, A., and ROTH, R. S., "Neutron Diffraction Structure Determinnation of the High Temperature Form of Lithium Tritantalate, H-$LiTa_3O_8$", J. Solid State Chem. 51, 275-292 (1984).

COPY AVAILABLE

PUBLICATIONS

KELLEY, R. D., CAVANAGH, R. R., RUSH, J. J., and MADEY, T. E. "Neutron Spectroscopy Studies of the Adsorption and Decomposition of C_2H_2 and C_2H_4 on Raney Nickel", Surf. Sci. 155, 480 (1985).

LEUNG, P. S., GODDARD, E. D., HAN, C. C., and GLINKA, C. J., "A Study of Polycation-Anionic Surfactant Systems" Colloids and Surfaces 13, 47-62 (1985).

LUKACEVIC, E., RUSH, J. J., and SANTORO, A., "Neutron Powder Diffraction and Inelastic Scattering Study of the Structures of Zr_2Pd, $Zr_2PdD_{1.70}$ and $Zr_2PdD_{1.96}$", Acta Crys. (in press).

LUKACEVIC, E., SANTORO, A., and ROTH, R. S., "Neutron Powder Diffraction Study of the Structure of the Molybdate of Composition $Li_20.9:La_20_3:32MoO_3$", Solid State Ionics (in press).

LYNN, J. W., GOTAAS, J. A., SHELTON, R. N. HORNG, H. E., and GLINKA, C. J. "Magnetic and Superconducting Properties of Holmium-Rich $(Er_{1-x}Ho_x)Rh_4B_4$", Phys. Rev. B 31, 5756-5767 (1985).

LYNN, J. W. "Helium Condensation Observed in Small Angle Neutron Scattering", Physica (in press).

MAGERL, A., RUSH, J. J., and ROWE, J. M. "Local Modes in Dilute Metal Hydrogen Alloys", Phys. Rev B (in press).

MATSUSHITA, Y., HODA, I., NAGASAWAM, M., LODGE, T. P., AMIS, E. J., and HAN, C. C., "Expansion Factor of a Part of a Polymer Chain in a Good Solvent Measured by Small Angle Neutron Scattering", Macromoleculs 17, 1785 (1984).

MCDONALD, G. W., UDOVIC, T. J. DUMESIC, J. A., and LANGER, S. H. "Equilibria Associated with Cupric Chloride Leaching of Chalcopyrite Concentrate", Hydrometall. 13, 125 (1984).

MCKERGOW, M. W., GILBERD, P. W., PICTON, P. J., ROSS, D. K. BLASCHKO, O., ANDERSON, I. S., and HAGEN, M., "Interatomic Potentials and Lattice Distortions in $PdD_{0.8}$" Belfast Conf. on `Hydrogen in Metals' 1985 (in press).

MICHEL, K. H. and ROWE, J. M. "KCN, a Model System of Tanslation-Rotation Coupling in Orientationally Disordered Crystals", J. Chem. Phys. 82, 199 (1985).

MICHEL, K. H. and ROWE, J. M. "Local Properties in Orientationally Disordered Crystals with Translation-Rotation Coupling", Phys. Rev. B (in press).

MICHEL, K. H. and ROWE, J. M. "Molecular Symmetry and Translation-Rotation Coupling in Orientatonally Disordered Crystals", Phys. Rev. B (in press).

MICHELL, A. D. and HIMES, V. L. "Compound Identification and Characterization Using Lattice-Formula Matching Techniques", Acta Cryst. A (in press).

NOSSAL, R., GLINKA, C. J., and CHEN S. H. "SANS Studies of Concentrated Protein Solutions I.", Bovine, Serum Albumin (in press).

PICKART, S. J., HASANAIN, S., ANDRAUSKAS, D., ALPERIN, H. A., SPANO, M., and RHYNE, J. J., "Magnetic Field Dependence of the Small Angle Scattering in Amorphous DyCu". J. Appl. Phys. 57, 3430 (1985).

BEST COPY AVAILABLE

PUBLICATIONS

PRINCE, E., TAKAGI, S., MATHEW, M. and BROWN, W. E., "The Structure of Dicalicum Potassium Heptahydrogen Tetrakis Phosphate", Acta. Cryst. C 40 1499-1502 (1984).

PRINCE, E., and NICHOLSON, W., "The Influence of Individual Reflections on the Precision of Parameter Estimates in Least Squares Refinement. Structure and Statistics inn Crystallography", Ed. A. J. C. Wilson (in press).

PRINCE, E., "Precision and Accuracy in Struture Refinement by the Rietveld Method. Structure and Statistics in Crystallograhy", Ed. A. J. C. Wilson (in press).

RHYNE, J. J., "Critica and `Subcritical' Magnetic States of Amorphous Rare Earth Spin Glasses", Physica 130B, 253 (1985).

RHYNE, J. J. and FISH, G. E., "Small Angle Neutron Scattering Evidence for the Absence of Long-Range Magnetic Order in Amorphous $Fe_{91}Ar_9$", J. Appl. Phys. 57, 3407 (1985).

RHYNE, J. J., "Magnetic Properties of Amorphous Metals", J. of Non-Crystalline Solids (in press).

RHYNE, J. J., "Effects of Random Field Interactions in Amorphous Rare Earth Alloys", IEEE Trans. Mag. (in press).

RHYNE, J. J., COOPER, B. R., HUBER, D. A., KOON, N. C., and O'HANDLEY, R. C. eds. "Proc. of the Intern. Conf. on Magnetism ICM-85", J. of Magnetism and Magnetic Materials (in press).

RHYNE, J. J. "Quenching of Long-Range Magnetic Order by Random Interactions in Amorphous Alloys", Physica (in press).

ROWE, J. M., BOUILLOT, J., RUSH, J. J., and LUTY, F., "Structural Phase Diagram of Mixed $(KCN)_x(KA)_{1-x}$ Crystal", Physica B (in press).

RUSH, J. J., ROWE, J. M., and RICHTER, D., "Dynamics of Dilute H in β-Phase Palladium Deuteride: A Novel Mass Defect", Phys. Rev. B 31, 6102 (1985).

RUSH, J. J. and ROWE, J. M. "Chemical Physics with Emphasis on Low Energy Ecitations", Physica B (in press).

RUSH, J. J., CAVANAGH, R. R., KELLEY, R. D., and ROWE, J. M., "Interaction of Vibrating H atoms on the Surface of Platinum Particles by Isotope Dilution Neutron Spectroscopy", J. Chem. Phys. 1985 (in press).

SPANO, M. L. and RHYNE, J. J. "Suppression of Long-Range Order by Random Fields in Tb_xFe_{1-x} Alloys", J. Appl. Phys. 57, 3303 (1985).

SPANO, M. L., ALPERIN, H. A., RHYNE, J. J., PICKART, S. J., HASANAIN, S., and ANDRAUSKAS, D. "Applied Field Response of the Spin Glass State in Amorphous $NdFe_2$", J. Appl. Phys. 57, 3432 (1985).

SPANO. M. L., and RHYNE, J. J., "Effects of Appied Fields on the Magnetic Order of Amorphous Tb_xFe_{1-x}", J. Magnetism and Magentic Matls. (in press).

STEIN, R. S. and HAN, C. C. "Neutron Scattering from Polymers", Physics Today 38 (1985).

BEST COPY AVAILABLE

PUBLICATIONS

SHIBAYAMA, M., YANG, H., STEIN, R. S., and HAN, C. C. "Study of Miscibility and Critical Phenomena of Deuterated Polystyrene and Hydrogenated Poly (Vingy methyl ether) by Small Angle Neutron Scattering", Macromolecules (in press).

SHULL, R. D. SINGHAL, S. P., MOZER, B., and MAELAND, A., "Small Angle Neutron Scattering of Metallic Glass", Proc. of the 5th Intern. Conf. on Rapidly Quenched Metals (in press).

STOECKLI, A., FURRER, A., SCHOENENBERGER, C. H., MEIER, B. H., ERNST, R. R., and ANDERSON, I. S., "Dynamics of Hydrogen Bonds in Carboxylic Acids", Physica B (in press).

TSAI, D. H. and TREVINO, S. F. "Simulation of the Initiation of Detonation in an Energetic Molecular Crystal", J. Chem. Phys. 81, 248 (1984).

UDOVIC, T. J., KELLEY, R. D., and MADEY, T. E., "The Methanation Activity of W(110)", Surf. Sci. 150, L71 (1985).

WAX, M. J., CAVANAGH, R. R., RUSH, J. J., STUKY, G. D., ABRAMS, L., and CORBIN, D. R., "A Neutron Scattering Study of Zerolite Rho", J. Am. Chem. Soc. (in press).

WERNER, S. A., RHYNE, J. J., and GOTAAS, J. A., "Temperature Dependence of the Spin Density Wave Magnetism in Copper-manganese", Solid State Commun. (in press).

INDEPENDENT PROGRAMS

BECKER, D. A., "Quality Assurance Techniques for Activation Analysis", Proc. 5th Intern. Conf. on Nuclear Methods in Environmental and Energy Res., U.S. DOE Publ. CONF-840408, U.S. Dept. of Energy, Washington, DC (1984).

BECKER, D. A., "The Role of Reactor Characterization in NBS Quality Assurance", J. Radioanalytical and Nucl. Chem. (in press).

BLACKMAN, M. J. "Provenience Studies of Middle Eastern Obsidian from Sites in Highland Iran", Archaeological Chemistry III, Joseph Lambert, ed., Am. Chem. Soc., Washington, D.C. (1984).

BLACKMAN, M. J., "Chemical Characteizations of Sealing Clays from Fourth Millenium B. C. Sites in Iran", The Transations of the Am. Nucl. Soc. 49, 168-169 (1985).

BLACKMAN, M. J., "The Provenience of Obsidian Artifacts from Late Chalcolithic Levels at Aphrodisias, Turkey", Prehistoric Aphrodisias, M. Joukowsky, ed., Archaeologia Transatlantica, IV Louvain-la-Neuve, Institut Superieur D'rchelogie et Histoire de L'Art Brown Univ. (1985).

BURGER, G. and SCHWARTZ, R. B., "Guidelines for the Establishment and Operation of a Secondary Standard Dosimetry Laboratory for Neutrons", IAEA Tech. Rept. Series (to be publ.)

DOWNING, R. G., FLEMING, R. F., MAKI, J. T., SIMONS, D. S., and STALLARD, B. R., "Near-Surface and Interfacial Profiling by Neutron Depth Profiling (NDP) and Secondary Mass Spectrometry (SIMS)", Proc. of Materials Res. Soc., Thin Films and Interfaces II Vol. 25, J. E. Baglin, D. R. Campbell, and W. K. Chu, eds., North Holland, 655-666 (1984).

BEST COPY AVAILABLE

PUBLICATIONS

DOWNING, R. G. MAKI, J. T., and FLEMING, R. F., "Application of Neutron Depth Profiling to Microelectronic Materials Processing", Special Proc. Industrial Chem. Div. Session for the 187th National Meeting, Am. Chem. Soc., L. A. Casper, ed. (in press).

EISENHAUE, C. M., HUNT, J. M., and SCHWARTZ, R. B., "Calibration Techniques for Neutrron Personal Dosimetry", 10, No. 1-4, 43-47 (1985).

Gilliam, D. M., Grundl, J. A., Lamaze, G., Eisenhauer, C. M., and Fabry, A., "Cross Section Measurements in the U235 Fission Spectrum Neutron Field", Proc. of the 5th ASTM-EURATOM Symposium on Reactor Dosimetry, Geesthacht, West Germany (Oct. 1985.

GREENBERG, R. R., "Radiochemical Procedures Used for Improved Low-Level Determinations of Critical Elements in Biological Materials, Use and Development of Low and Medium Flux Research Reactors", Supplement to Atomkernenergie-Kerntechnik 44, 659 (1964).

GREENBERG, R. R. and CARPENTER, B. S., "High Accuracy/High Precision Determination of U-235 in Nondestructive Assay Standards by Gamma-Ray Spectrometry", Proc. Fifth Intl. Conf. on Nuclear Methods in Environmental and Energy Research, 644 (1984).

GREENBERG,, R. R., "Multielement Analysis of NBS Coals by Instrumental Neutron Activation Analysis, in Methods and Procedures Used at the National Bureau of Standards to certify Sulfur in Coal SRM's for Sulfur Content, Calorific Value, Ash Content", T. E. Gills ed., NBS Publ. 260-94, 32 (1984).

GREENBERG, R. R., FLEMING, R. F. and ZEISLER, R., "High Sensitivity Neutron Activation Analysis of Biologicl/Environmental Standard Reference Materials", Environ. Intern., 10, 129-136 (1984).

GRUNDL, J. A., "Examination of $^{10}B(n,He)$ and $^{6}Li(n,He)$ Cross Section Measurements in Reactor Physics Benchmarks", Proc. Intern. Conf. on Nuclear Data for Basic and Applied Science, 1985.

JORNET, A., BLACKMAN, M. J., and OLIN, J. S., XIIIth to XVIIIth Century Ceramics from the Paterna-Manises Area (Spain), in Ceramics and Civilization, D. Kingery, ed., Amcerican Ceramic Society (1985).

KINGSTON, H. M. and GREENBERG, R. R., "An Elemental Ratioing Technique for Assessing Concentration Data from a Complex Water System", Environ. Intern. 10, 153 (1984).

LINDSTROM, R. M. and ANDERSON, D. L., "Analytical Neutron-Capture Gamma-Ray Apectroscopy: Statues and Prospects, in Capture Gam,ma-Ray Spectroscopy and Related Topics-1984", S. Raman, ed., (AIP Conf. Proc. No. 125), Am. Inst. Phys., New York, 810-819 (1985).

LINDSTROM, R. L., "Activation Analysis of Semiconductor Materials, in ACS Books" (in press).

LUNTZ, G. J., ROOK, H. L. and LINDSTROM, R. M., "Determination for I-129 at Natural Levels by Thermal Neutron Activation Analysis", Journal of Trace and Microprobe Techniques 2 (1), 33-51 (1984).

BEST COPY AVAILABLE

PUBLICATIONS

McGARRY, E. D., GILLIAM, D. M., LAMAZE, G., EISENHAUER, C. M., and FABRY, A., "The U.S. U235 Fission Spectrum Standard Neutron Field Revisited", Proc. Fifth ASTM-EURATOM Sym. on Reactor Dosimetry,, Geesthact, West Germany (Oct. 1984).

MICHEL, R., IYENGAR, G. V., and ZEISLER, R., "Current Aspects of Multielement Analysis in the Life Sciences", Proc. Sym. Instrumental Multielement Analysis, Julich, FRG, April 2-5 (1984).

MICHAEL, R., IYENGAR, G. V. and ZEISLER, R., "Current Aspects of Multielement Analysis in the Life Sciences", Proc. Symp. Instrumental Multielement Analysis, Julich, FRG, April 2-5, 1985 (in press).

MYERS, J. E. and BLACKMAN, M. J., "Conical Plates from Medieval Qsar es-Seghir, Proc. of the Third Intern. Congress on Medieval Ceramics (1985).

OLIVER, B. M., FARRAR IV, H., GILLIAM, D. M., and LIPPINCOTT, E. P., "Spectrum-Integrated Helium Generation Cross Section for ^{6}Li and ^{10}B in the Immediate-Energy Standard Neutron Field", Proc. 5th ASTM-EURATOM Sym. on Reactor Dosimetry, Geesthacht, Germany (Sept. 1984).

PETILLI, M., and GILLIAM, D. M., "Evaluation of Uncertainties of ^{235}U Fission Spectrum", Proc. 5th ASTM-EURATOM Sym. on Reactor Dosimetry, Geesthacht, Germany (Sept. 1984).

RILEY Jr., J. E., MITCHELL, J. W., DOWNING, R. G., FLEMING, R. F., LINDSTROM, R. M., and VINCENT, D. H., "Materials Analysis Using Thermal Neutron Reactions: Applications, Materials Science Forum 2, 123-132 (1984).

SCHRODER, I. G., LINPEI, Li, GILLIAM, D. M., McGARRY, E. D. and EISENHAUER, C. E., "Measurement of Absolute Fission Cross Sections for ^{252}Cf Spontaneous Fission Neutrons, ANS Trans. (1985).

STONE, S. F. and ZEISLER, R., "Evaluation of Biological Samples for Specimen Banking and Biomonitoring By Nuclear Methods", Proc. 5th Conf. on Nuclear Methods in Environment and Energy Technology, J. R. Vogt, ed. NTIS U.S. Dept. of Commerce, Springfield, VA, CONF-840408 (1984).

STROUBE, W. B. and LUTZ, G. J., "Epithermal Neutron Activation Analysis of Powdered Infant Formula for Iodine", Trans. Amer. Nucl. Soc. 49, 164-165 (1985).

STROUBE, W. B. and LUTZ, G. J., "Determination of Iodine in Liquid Infant Formula by Epithermal Neutron Activation Analysis" (in press).

VANDERVOST, W., SHEPHERD, F. R., and DOWNING, R. G., "High Resolution SIMS and Neutron Depth Profiling of B through Oxide-Silicon Interfaces, J. Am. Vacuum Soc., Sci. Technol., A3 (3), 1318-1321 (1985).

WILSON, S. R., PAULSON, W. M., GREGORY, R. B., KRAUSE,, R. J., GRESSETT, J. D., McDANIEL, F. D., and DOWNING, R. G., "Properties of Ion Implanted Polysilicon Layers Subjected to Rapid Thermal Annealing", J. Electrochemical Soc.; Solid State Sci. and Tech. 132 (4) 922-929 (1984).

WISE, S. A. and ZEISLER, R., "The Pilot Environmental Specimen Bank Program", Environ. Sci. Technol., 18 302A-307A (1984).

BEST COPY AVAILABLE

NBS-114A (REV. 2-8C)

U.S. DEPT. OF COMM. **BIBLIOGRAPHIC DATA SHEET** (See instructions)	1. PUBLICATION OR REPORT NO. NBS/TN-1217	2. Performing Organ. Report No.	3. Publication Date December 1985

4. TITLE AND SUBTITLE

NBS Reactor: Summary of Activities July 1984 Through June 1985

5. AUTHOR(S)

Frederick J. Shorten, Editor

6. PERFORMING ORGANIZATION (If joint or other than NBS, see instructions)

NATIONAL BUREAU OF STANDARDS
DEPARTMENT OF COMMERCE
GAITHERSBURG, MD 20899

7. Contract/Grant No.

8. Type of Report & Period Covered

7/84 - 6/85

9. SPONSORING ORGANIZATION NAME AND COMPLETE ADDRESS (Street, City, State, ZIP)

Same as # 6.

10. SUPPLEMENTARY NOTES

☐ Document describes a computer program; SF-185, FIPS Software Summary, is attached.

11. ABSTRACT (A 200-word or less factual summary of most significant information. If document includes a significant bibliography or literature survey, mention it here)

This report summarizes all those programs which depend on the NBS reactor. It covers the period from July 1984 through June 1985. The programs range from the use of neutron beams to study the structure and dynamics of materials through nuclear physics and neutron standards to sample irradiations for activation analysis, isotope production, radiation effects studies, neutron radiography, and nondestructive evaluation.

12. KEY WORDS (Six to twelve entries; alphabetical order; capitalize only proper names; and separate key words by semicolons)

Activation analysis; crystal structure; diffraction; isotopes; molecular dynamics; neutron; neutron radiography; nondestructive evaluation; nuclear reactor; radiation.

13. AVAILABILITY

☒ Unlimited

☐ For Official Distribution. Do Not Release to NTIS

☐ Order From Superintendent of Documents, U.S. Government Printing Office, Washington, D.C. 20402.

☒ Order From National Technical Information Service (NTIS), Springfield, VA. 22161

14. NO. OF PRINTED PAGES

175

15. Price

BEST COPY AVAILABLE

☆U.S. GOVERNMENT PRINTING OFFICE: 1985 491 070 20311

NBS Technical Publications

Periodical

Journal of Research—The Journal of Research of the National Bureau of Standards reports NBS research and development in those disciplines of the physical and engineering sciences in which the Bureau is active. These include physics, chemistry, engineering, mathematics, and computer sciences. Papers cover a broad range of subjects, with major emphasis on measurement methodology and the basic technology underlying standardization. Also included from time to time are survey articles on topics closely related to the Bureau's technical and scientific programs. Issued six times a year.

Nonperiodicals

Monographs—Major contributions to the technical literature on various subjects related to the Bureau's scientific and technical activities.

Handbooks—Recommended codes of engineering and industrial practice (including safety codes) developed in cooperation with interested industries, professional organizations, and regulatory bodies.

Special Publications—Include proceedings of conferences sponsored by NBS, NBS annual reports, and other special publications appropriate to this grouping such as wall charts, pocket cards, and bibliographies.

Applied Mathematics Series—Mathematical tables, manuals, and studies of special interest to physicists, engineers, chemists, biologists, mathematicians, computer programmers, and others engaged in scientific and technical work.

National Standard Reference Data Series—Provides quantitative data on the physical and chemical properties of materials, compiled from the world's literature and critically evaluated. Developed under a worldwide program coordinated by NBS under the authority of the National Standard Data Act (Public Law 90-396). NOTE: The Journal of Physical and Chemical Reference Data (JPCRD) is published quarterly for NBS by the American Chemical Society (ACS) and the American Institute of Physics (AIP). Subscriptions, reprints, and supplements are available from ACS, 1155 Sixteenth St., NW, Washington, DC 20056.

Building Science Series—Disseminates technical information developed at the Bureau on building materials, components, systems, and whole structures. The series presents research results, test methods, and performance criteria related to the structural and environmental functions and the durability and safety characteristics of building elements and systems.

Technical Notes—Studies or reports which are complete in themselves but restrictive in their treatment of a subject. Analogous to monographs but not so comprehensive in scope or definitive in treatment of the subject area. Often serve as a vehicle for final reports of work performed at NBS under the sponsorship of other government agencies.

Voluntary Product Standards—Developed under procedures published by the Department of Commerce in Part 10, Title 15, of the Code of Federal Regulations. The standards establish nationally recognized requirements for products, and provide all concerned interests with a basis for common understanding of the characteristics of the products. NBS administers this program as a supplement to the activities of the private sector standardizing organizations.

Consumer Information Series—Practical information, based on NBS research and experience, covering areas of interest to the consumer. Easily understandable language and illustrations provide useful background knowledge for shopping in today's technological marketplace.

Order the **above** *NBS publications from: Superintendent of Documents, Government Printing Office, Washington, DC 20402.*

Order the **following** *NBS publications—FIPS and NBSIR's—from the National Technical Information Service, Springfield, VA 22161.*

Federal Information Processing Standards Publications (FIPS PUB)—Publications in this series collectively constitute the Federal Information Processing Standards Register. The Register serves as the official source of information in the Federal Government regarding standards issued by NBS pursuant to the Federal Property and Administrative Services Act of 1949 as amended, Public Law 89-306 (79 Stat. 1127), and as implemented by Executive Order 11717 (38 FR 12315, dated May 11, 1973) and Part 6 of Title 15 CFR (Code of Federal Regulations).

NBS Interagency Reports (NBSIR)—A special series of interim or final reports on work performed by NBS for outside sponsors (both government and non-government). In general, initial distribution is handled by the sponsor; public distribution is by the National Technical Information Service, Springfield, VA 22161, in paper copy or microfiche form.

BEST COPY AVAILABLE